HOKKAIDO UNIVERSITY

Title	Study on Morphological and Electronic Structures of Semiconductor Electrodes in Electrolyte Solutions
Author(s)	Koinuma, Michio
Degree Grantor	北海道大学
Degree Name	博士(理学)
Dissertation Number	甲第3948号
Issue Date	1996-06-28
DOI	https://doi.org/10.11501/3113504
Doc URL	https://hdl.handle.net/2115/51351
Type	doctoral thesis
File Information	000000298695.pdf

Hokkaido University Collection of Scholarly and Academic Papers : HUSCAP

Study on Morphological and Electronic Structures of Semiconductor Electrodes in Electrolyte Solutions

(半導体／電解質溶液界面での構造および電子状態に関する研究)

Michio Koinuma

Physical Chemistry Laboratory
Division of Chemistry
Graduate School of Science
Hokkaido University

1996

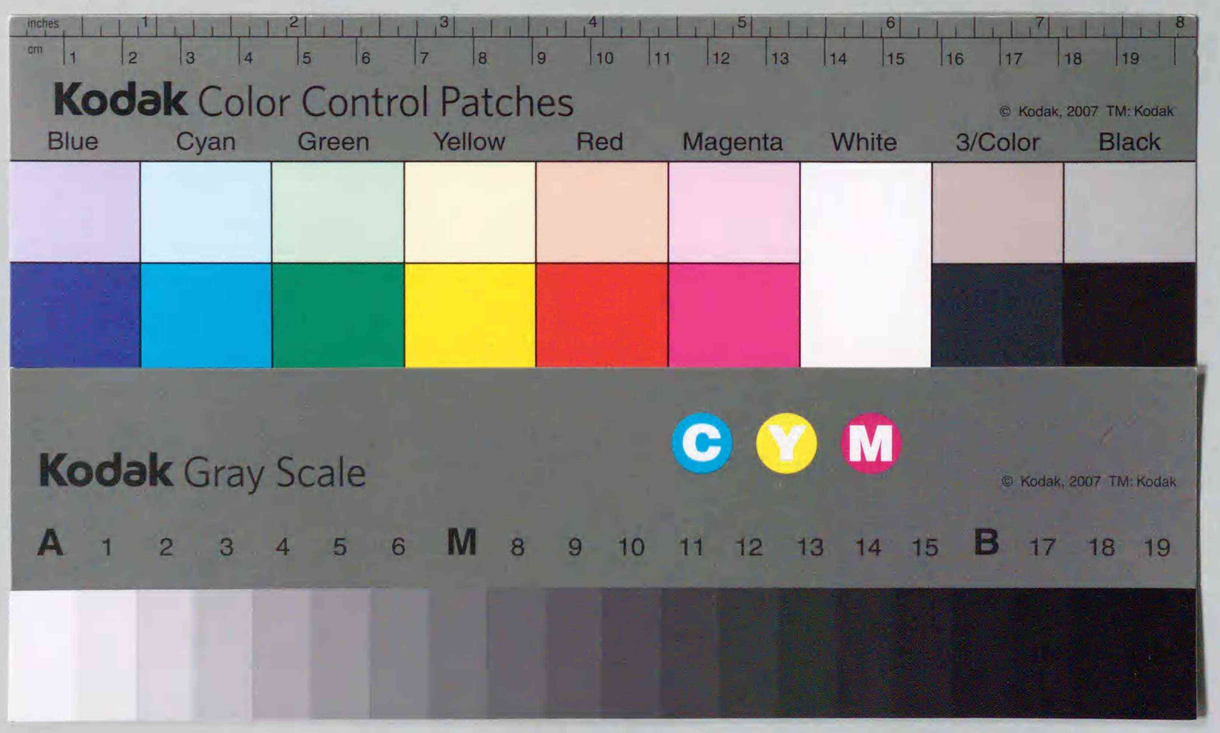

9

Study on Morphological and Electronic Structures of Semiconductor Electrodes in Electrolyte Solutions

（半導体／電解質溶液界面での構造および電子状態に関する研究）

Michio Koinuma

Physical Chemistry Laboratory
Division of Chemistry
Graduate School of Science
Hokkaido University

1996

CONTENTS

Aknowledgement

Chapter 1 Introduction 1
1.1 General Introduction 1
1.2 Electrochemistry in the Semiconductor Electrodes 3
1.3 Scanning Tunneling Microscopy (STM) 5
1.3.1 Principles of STM 5
1.3.2 Electrochemical STM (ECSTM) 7
1.4 Atomic Force Microscopy (AFM) 8
1.5 Surface X-ray Diffraction (SXRD) 11
1.5.1 Basic Principles of In-plane X-ray diffraction . 13
1.6 Outline of the Present Thesis 15

Chapter 2 Experimental 19
2.1 Chemicals 19
2.2 Semiconductor Electrodes 19
2.2.1 GaAs 19
2.2.2 CdS 20
2.2.3 InSe 20
2.3 TCV Measurement 21
2.4 AFM Measurement 23
2.5 SXRD Measurement 25

Chapter 3 Tip Current Voltammetry (TCV) Study of a Variety Surface Treatment at n-GaAs(100)/Electrolyte Interface 29
3.1 Introduction 29
3.2 Results and Discussion 30
3.2.1 "Etched" n-GaAs Electrode 30
3.2.2 "Ru-treated" and "S-treated" n-GaAs Electrodes: Effect of Surface States on TCV 33
3.2.3 CdS Electrode 34
3.4 Conclusion 35

Chapter 4 AFM Study of Surface Structure and Electrochemical Reaction of InSe Single Crystals..... 39
4.1 Introduction..... 39
4.2 Results and Discussion..... 40
4.2.1 Measurement in Air..... 40
4.2.2 Electrochemical AFM Observation..... 41
4.3 Conclusion..... 47

Chapter 5 AFM Study of Surface Structure and Electrochemical Reaction of GaAs(100) Single Crystals..... 51
5.1 Introduction..... 51
5.2 Results and Discussion..... 53
5.2.1 p-GaAs(100) in HCl Solution..... 53
5.2.2 p-GaAs(100) in H_2SO_4 Solution..... 57
5.2.3 p-GaAs(100) in Na_2S Solution..... 60
5.2.4 n-GaAs(100) in HCl Solution..... 63
5.2.5 Surface Modification..... 66
5.3 Conclusion..... 70

Chapter 6 Copper Electrochemical Deposition on GaAs(100) Surface - An ECAFM Study..... 75
6.1 Introduction..... 75
6.2 Results and Discussion..... 76
6.2.1 p-GaAs(100) in HCl-$CuCl_2$ Solution..... 76
6.2.2 p-GaAs(100) in H_2SO_4-$CuSO_4$ Solution..... 84
6.2.3 Selective Cu Deposition at μm Defects Created by AFM Tip Modified Surface..... 89
6.3 Conclusion..... 90

Chapter 7 In Situ Observation OF Anodic Dissolution Process of p-GaAs(001) in HCl Solution by SXRD..... 95
7.1 Introduction..... 95
7.2 Results and Discussion..... 96
7.3 Conclusion..... 98

Chapter 8 Gneral Conclusion..... 100

Acknowledgment

I wish to express my sincerest thanks to Prof. K. Uosaki for his invaluable comments, discussions and suggestions and his constant encouragement during the period of this research project.

Hearty thanks are due to Prof. Y. Nakamura, Prof. M. Ichikawa, Prof. N. Kitamura, and Prof. T. Inabe, who acted as examiner of the dissertation, for their helpful and useful suggestion. Grateful acknowledgment is made to Prof. K. Maruoka and Prof. M. Miyashita for their suggestions.

Thanks are also due to the staffs of the Physical Chemistry Laboratory, Prof. S. Nakabayashi, Dr. T. Kondo, and Dr. S. Ye for the many fruitful discussions. It is also great pleasure for me to thank to Dr. K. Murakoshi and Dr. Y. Sato for their generous collaborations and encouragement. I would like to acknowledge helpful with Mr. I. Yagi, Miss N. Sekine, Mr. H. Noguchi, Mr. K. Tamura, Mr. R. Yamada, and Mr. K. Konishi. I am also greatly indebted to all the students studied together with me at Physical Chemistry Laboratory. Thanks are due to also due to Mr. T. Kiya and Mr. N. Sakai for their technical supports in the experiments. I am grateful to Mrs. K. Masuyama, Miss K. Sasaki, and Mrs. K. Yata for their encouragements and assistance for completing the thesis.

I gratefully acknowledge Prof. T. Matsushita and Dr. K. Takeshita of Photon Factory, National Laboratory for High Energy Physics for his help in measuring SXRD and Dr. I. Saeki of Graduate School of Engineering, Hokkaido University for his help in measuring XPS. I am also grateful to Dr. Chevy of Université Pierre et Marie Curie-Paris VI and Mr. H. Fujita of Mitsubishi Chemical Corporation for providing with InSe and GaAs single crystals, respectively.

I am also thankful to Japan Society for the Promotion of Science for the support.

Finally, I sincerely thank my parents, grandparents, and brother for their constant encouragement, understanding and financial support.

Michio KOINUMA

Sapporo
April, 1996

CHAPTER 1

INTRODUCTION

CHAPTER 1
INTRODUCTION

1.1 General Introduction

The science of semiconductors makes a great contribution to the progress not only in the field of electronics but also in various fields of science. In particular, since electrochemistry is closely related to electronics, it is natural for the two fields to utilize mutual knowledge. Thus, many electrochemists have been studying semiconductors and making some contribution to the progress in the science of semiconductors. In 1955, Brattain and Garrett used a semiconductor as an electrode for the first time and investigated theoretically [1]. Since then the knowledge of tsemiconductor electrochemistry has grown steadily and many reviews and books on this subject have appeared [2-8]. The research activity in this field, however, has grown significantly in the last 20 years, following the suggestion by Fujishima and Honda that solar energy may be directly converted to a chemical energy, hydrogen, by using semiconductor/aqueous electrolyte solution/metal cells [9]. This process, photoelectrochemical energy conversion, attracted many research groups. Subsequently, Gerischer [10] proposed an alternative type of solar cell using the semiconductor electrodes in electrolyte solutions, which is called a regenerative cell or a wet solar cell. In this type of cell, a dissolved reducing agent is photoanodically oxidized at an *n*-type semiconductor, while the corresponding oxidizing agent is reduced again at a metal counter electrode in dark. In contrast to the Fujishima-Honda cell, here the electrodes were connected through a load, the purpose being to convert solar energy not to chemical energy but to electrical energy. The regenerative cells seemed attractive, since less strict conditions were imposed as far as the band-gap width and the band edge position are concerned. Thus, semiconductor photoanodes with a less wide band gap could be used and the active part of the solar spectrum hence extended toward the visible and infrared region in this system. The stability of illuminated *n*-type semiconductors with respect to photocorrosion brought the serious problem for the solar energy conversion using the semiconductor electrodes. In other words, the fact that not only the photoanodic oxidation of the reducing agent in the solution but also the anodic dissolution of the semiconductor itself contributes to the

current. The letter leads to the deterioration of the cell. To find a way to suppress the anodic dissolution of the semiconductor, one need to deepen the insight into the mechanisms of these reactions.

Anodic dissolution of the semiconductor has some positive aspect as well. For example, electronic industry utilizes the dissolution reactions in various ways. Etching of the semiconductors is indeed an essential process in microelectronics device technology [11,12]. Various kinds of the surface layers such as oxide and damage layer are removed by etching. Furthermore, the etching procedures are used to reveal different kinds of crystal defects.

Electrochemical deposition of metal onto the semiconductor is also an important process. Thin metal layers on the semiconductor surfaces are used to form Schottky barriers [13,14], to make ohmic contacts on the semiconducting materials [15], and to increase the catalytic effect of the surface for a specific reaction [16]. Some of the advantages of electrochemical treatments over conventional vacuum techniques are its ease of use and low cost. Hence much research has been carried out to improve and utilize the electrochemical plating process.

Thus, it is clear that the understanding and control of various electrochemical reactions are quite important. The mechanisms of the semiconductor electrode reactions in the electrolyte solution have been inferred by a variety of electrochemical and spectroscopic techniques. Most of the techniques employed traditionally such as cyclic voltammetry [17,18], impedance spectroscopy [19,20], and luminescence method [21,22] can only provide the information averaged for whole surface. It is well known that rate and selectivity of the electrochemical reactions are very sensitive to the nature of the surface such as the crystal orientation and density of the defects. To fully understand the reactions, It is essential to obtain the information of morphological and electronic structures of the electrodes with atomic resolution. Although the atomically resolved information is obtained with relative loose by ultra high vacuum (UHV) techniques such as transmission electron microscopy (TEM) and low energy electron diffraction (LEED), the UHV techniques can be applied to electrochemical system only for the *ex situ* examination. On the other hand, scanning probe microscopy (SPM) can monitor the information of electrode/electrolyte interface.

In the present study, *in situ* observation of the semiconductor surface structure and the electronic structure were carried out by using electrochemical atomic force microscopy (ECAFM) and tip current voltammerty (TCV). Moreover, electrochemical surface X-ray diffraction (SXRD) was used to monitor electrochemical dissolution process of *p*-GaAs(100) surface.

In the following sections, basics of semiconductor/electrode interface and principles of techniques employed in this study are briefly described.

1.2 Electrochemistry in the Semiconductor Electrodes

The semiconductor/electrolyte contact has been extensively investigated since the 1970s for solar cell and technological applications. Theoretical details are available in many text books and review articles [2-8,23,24]. The contact between a semiconductor and an electrolyte solution behaves more or less like a solid state Schottky diode, with the electrolyte playing the role of the metal layer.

In Fig. 1.1 (a) the semiconductor and the electrolyte solution are represented in terms of bands of energy vs. distance z from the interface after contact. At equilibrium, the Fermi levels have equalized and electronic exchanges occurred. This builds the distribution of charges shown in Fig. 1.1 (b). Q_{SC} is the space charge in the semiconductor and extends over several 10 nm, since the density of electronic charges available in the semiconductor is several orders of magnitude smaller than that in solution (typically 10^{17} charges•cm^{-3} in the semiconductor against 10^{20} charges•cm^{-3} in the solution), which corresponding to immobile ionized dopants because each transferred electronic charge leaves one ionized atom. Q_{SC} is positive in the case of an *n*-type electrode. Q_S is localized

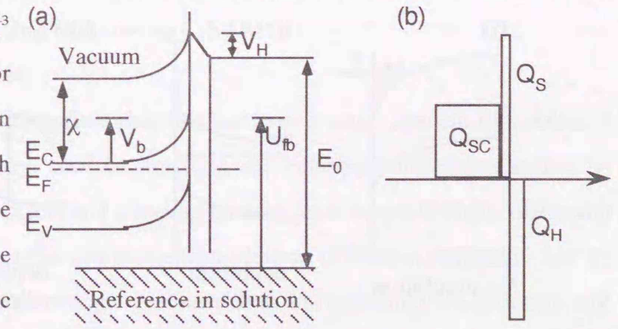

Fig. 1.1 Distribution of charge (a) and energy diagram (b) for the *n*-type semiconductor/electrolyte interface: U_{fb} is the flat band potential and V_b is the band bending. The energy difference E_0 depends on the reference electrode in solution. E_0 = -4.5 eV for the normal hydrogen electrode (NHE).

at the surface and arises from surface states or adsorbates for instance. Q_H is an ionic counter charge in the Helmholtz layer (thickness ~ 3 Å) which compensates $Q_{SC} + Q_S$. In Fig. 1.1 (a), the position of energy levels at the surface, with respect to the reference in solution, depends on several parameters, including electron affinity of the material, creation of surface states, ionic adsorption [3,4]. Inside the semiconductor the potential drop, also referred to as the band bending, V_b, is a potential barrier to majority carriers. The space charge width varies as $(V_b/N_D)^{1/2}$.

The energy diagram can be quoted against a reference in solution from the measure of U_{fb}, the flat band potential, which represents the potential that must be applied to the electrode to flatten bands. U_{fb} is determinated by different methods [25]. U_{fb} depends on the pH of the solution and shifts by -0.059 V/pH unit for many materials such as Si, GaAs, and semiconductor oxides. The generally accepted reason is specific

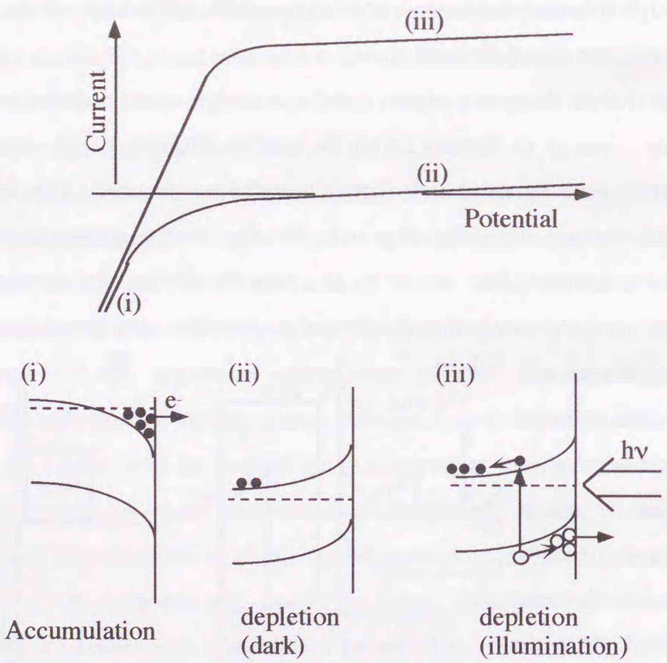

Fig. 1.2 Typical current-potential curves of an *n*-type semiconductor electrode in darkness and under illumination. The band diagrams illustrate the shift of the band edges with illumination (right) and at cathodic bias (left).

adsorption of OH^- or H^+ legends, especially on materials forming oxide or hydride layers. To simplify U_{fb} is however partially independent of the applied bias and the overvoltage drops inside the semiconductor. The density n_s of majority carriers at the surface is therefore monitored by the bias according to the Boltzmann relationship

$$n_s = N_D \exp(-eV_b/kT) \quad (1.1)$$

with

$$V_b = U_s - U_{fb} \quad (1.2)$$

because of the potential barrier at the surface.

The carrier transport properties of the interface are summarized in Fig. 1.2. Typical current-potential curve (Fig. 1.2 (a)) and corresponding energy diagram (Fig. 1.2 (b)) are shown for an *n*-type electrode. In darkness a rectifying behavior is observed at positive bias because the surface is depleted of electrons (diode-like behavior). At cathodic bias the band is bent upward and excess electrons roll down along the bottom of the conduction band towards near the surface. Thus, the enriched electrons flow from the semiconductor to the solution. Illumination of the surface with light of energy larger than the band gap generates electron-hole pairs. If the band bending is sufficiently large, the electron-hole pairs are separated by electric field in the space charge region, and the minority carriers reach the surface. The photocurrent is normally proportional to light intensity in such conditions because each photogenerated carrier is transferred to solution.

1.3 Scanning Tunneling Microscopy (STM)

1.3.1 Principles of STM

The understanding of surface structure has been a major concern of condensed matter physics and chemistry. Surface structures and conditions have been studied by electron microscopes (*e.g.* TEM and scanning electron microscope (SEM)), diffraction measurements (*e.g.* LEED, reflection high energy electron diffraction (RHEED), and X-ray diffraction (XRD)), and scattering experiments (*e.g.* ion scattering). Direct imaging of geometric and electronic surface structures with atomic resolution had been impossible until the invention of scanning tunneling microscopy (STM) by G. Binnig, H. Rohrer, and Ch. Gerber in 1981 [26,27]. The STM has attracted considerable attention because it is a method of measuring the surface of solid surface in three-dimensional real-space with

vertical resolution as high as 10 pm and horizontal resolution as high as ~0.2 nm. Since the observation of real-space image of Si(111)-(7x7) [28], the STM has been accepted as a powerful surface science tool and used in wide variety of fields, including surface science, solid state physics, electrochemistry, biology, organic and nano-machining. There already exist many review articles [29-32] devoted to STM.

If the distance of two conducting electrodes separated by some isolator which forms a barrier for the electrons is close enough, the overlap of the wave functions of the two electrodes causes electrons to travel through the barrier. This tunneling phenomenon has been known since the introduction of quantum mechanics in 1920's [33]. The tunneling electrons constitute a current that is a function of the distance between the electrons and the nature of the electronic states involved. One-dimensional planar tunneling has been often used as a simple model to describe three-dimensional vacuum tunneling [34]. For free electrons tunneling through the planar barrier at small voltages U « f, the current density, j, can be written as [35]

$$j = (2\pi e^2) \bullet (k_0 / 4\pi d) \bullet V \bullet \exp(-2k_0 d) \qquad (1.3)$$

where d is the effective tunneling distance (in Å), k_0 is the inverse decay length of the wave function density outside the surface, V is the applied voltage (in volts), and $(2\pi e^2 / h) = 2.44 \times 10\text{-}4\ \Omega^{-1}$. In this case of vacuum tunneling, k_0 is related to the effective barrier height ϕ [$\approx (\phi_1 + \phi_2) / 2$] by

$$k_0 = (2\pi / h) \bullet (2m\phi)^{1/2} \qquad (1.4)$$

where m is the electron mass.

For a typical barrier height of 4 eV, the tunneling current decreases roughly by an order of magnitude when the gap d is increased by 0.1 nm. Even if the tunneling current is only kept constant to with in 10 %, then the gap d remains constant to within 40 pm (*i.e.* Au atomic size of 1/75). One of the electrodes of the STM is formed into a sharp tip and acts as a probe which investigates the surface properties of opposite electrode. Because of the rapid decrease in tunneling current with the distance between the surface and tip, usually only a few of the outermost atoms on the tip contribute significantly to the tunneling current. Hence, the vertical resolution, d, using the local radius of curvature at tip end R is affected by the shape of the tip and is given by [36]

$$d = \{2(R + d) / k_0\}^{1/2} \qquad (1.5)$$

thus, the vertical resolution is around 0.2 nm, if tip end is consisted from a few atoms (R = 0.3 nm). The surface topography of the sample is measured by scanning the tip across the surface and sensing the height of the surface from the voltage applied to a piezo adjusting the lateral position of the tip.

1.3.2 Electrochemical STM (ECSTM)

If the tunnel junction of Fig. 1.3 (a) is simply immersed in an electrolyte, the polarization between the tip and the sample will promote an electrolysis. A bipotentiostat is necessary to ensure real tunneling between the sample and the tip. Such a device, classically used in electrochemistry, enables to split the tunnel junction into two solid/liquid interfaces, independently polarized against a reference of potential (Fig. 1.3 (b)). Using this configuration, also referred to as the four-electrode configuration and introduced very early by several groups, it is possible to avoid any electrochemical transfer between the sample and the tip [37-39]. The reference potential is an electrode whose potential is well defined and constant with respect to the vacuum level. The sample is based against the reference electrode monitor reactions at the surface, just as in a classical electrochemical cell. The tip potential is adjusted independently of that of the sample to nullify the faradic current at its extremity. The potentiostat regulates the potential of an auxiliary electrode, also called the counter electrode, so as to prevent any current flow in circuit of the reference electrode. The counter electrode therefore collects all the electrochemical current issued from the sample and tip collects only tunneling electrons when its potential is properly adjusted. Usually the tunnel bias

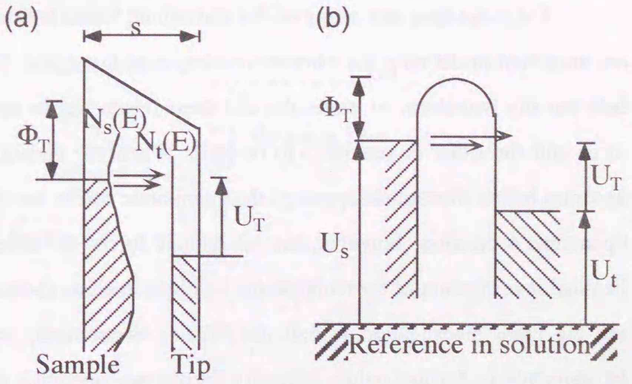

Fig. 1.3 Energy diagram of a tunneling junction. (a) In UHV: U_T is the tunnel bias. (b) In the electrolytic environment: U_s and U_t are ser independently against the reference potential in solution (four-electrode configuration); the tunnel voltage is $U_T = U_t - U_s$.

$U_T = U_s - U_t$ depends on the sample bias U_s, because the tip potential U_t is generally constant.

1.4 Atomic Force Microscopy (AFM)

The atomic force microscope (AFM) was developed as a new type microscope to remedy the severe limitation of the STM which can image only conducting materials by G. Binnig, C. F. Quate, and Ch. Gerber in 1986 [40]. The basic principles of the AFM are very related to other techniques such as stylus profilometry and the STM. The AFM can image the surface topography sensing the force applied between the sample and tip held in close proximity to each other. The AFM has a tip attached to a micro-cantilever which provides a restoring force to counter that obtained from the interaction between the sample and tip. Changes in the deflection of the cantilever are correspond to changes in the tip-sample force. The deflection of the cantilever is monitored as the tip is scanned. The deflection signal is used in a feedback loop similar to the way the tunneling current is used in an STM. The data can be acquired whether by measuring the cantilever signal or by adjusting the tip-sample separation using feedback to maintain a constant cantilever deflection. The latter measurement mode is said "constant force mode" and most AFM studies have been obtained in this mode. The AFM field, new by any measure and in substantial flux, has already been the subject of many reviews [41-44].

The magnitude and nature of the interatomic forces between sample surface and tip are important in defining the ultimate resolution of the AFM. The interatomic forces act between any two atoms or molecules and these forces can be two types; One is attractive force and the other is repulsive force [45]. When the distance of the sample and tip becomes below interatomic spacings the interatomic forces are always repulsive. At large tip-sample separation, however, the interatomic forces are either repulsive or attractive. Detailed investigation of the components involved in either forces is still discussed activity, but the main investigation is van der Waals, electrostatic, and magnetostatic forces. Experiments performed when attractive forces are operative are so-called "noncontact mode" while experiments under condition occurring with repulsive force, that is, when the tip is contact with the sample called "contact mode". Noncontact mode measurements operate with relatively large tip-sample separation and therefore are not capable of

achieving atomic resolution because of reduced interaction between the sample and tip. Thus, most AFM studies have been performed in contact mode.

There are some methods that detect the deflection of cantilever. Changes in this deflection must be on the order of atomic dimensions or less for high resolution imaging. The original AFM developed by G. Binnig utilized an STM apparatus to detect the

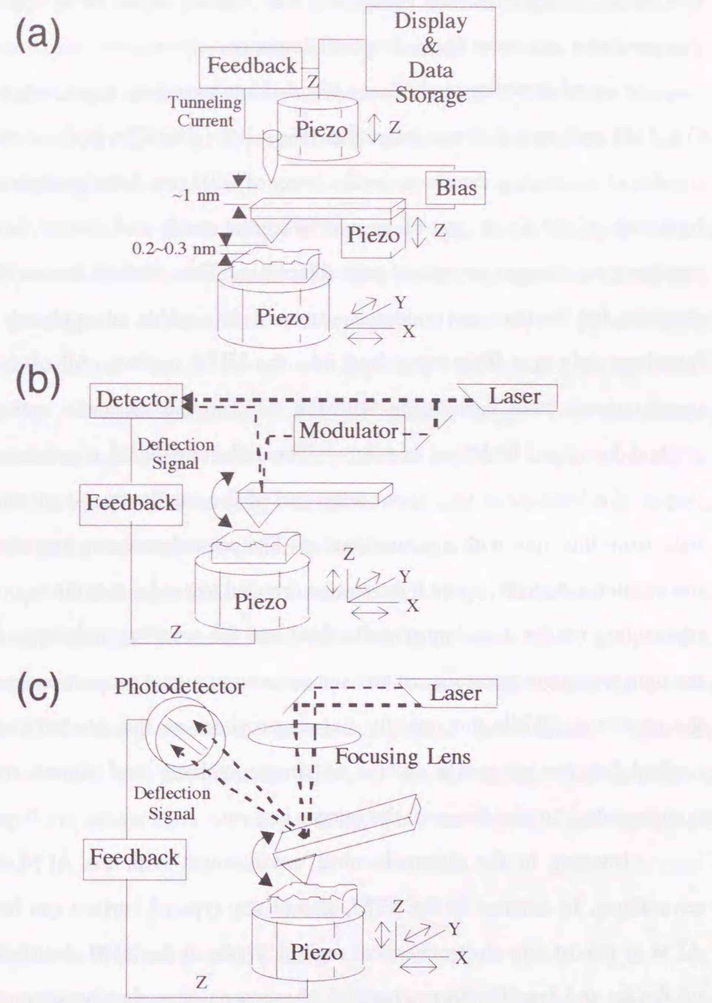

Fig. 1.4 Schematic diagrams of an atomic force microscope. (a) The original AFM developed by G. Binnig utilized an STM apparatus, (b) interferometry method, and (c) optical lever deflection.

movement of the cantilever. As shown in Fig. 1.4 (a), the cantilever which is conductivity on the back side of it is sandwiched between the sample and the STM tip [40]. The images are obtained to convert the morphology of the sample surface into that of conductive surface (changes in the deflection of the cantilever). However, high resolution image is difficult to obtain in this method because the force exerted by the STM tip exceed that being probed with the AFM. For this reason, most AFM apparatuses which is designed now use some form of optical detection.

Optical detection methods are divided into two basic types; interfermetry (Fig. 1.4 (b)) [46] and optical lever deflection (Fig. 1.4 (c)) [47]. Both of those methods are capable of measuring cantilever on the order of 0.01 nm. Interferometric method uses the back side of the tip as part of an interferometer cavity and detects the deflection of the cantilever as changes in optical path difference. This method has received considerable attention for vacuum environments, since it is capable of applying UHV system to introduce only one fiber optic lead into the UHV camber. All of the electrochemical measurements have been made with the AFM which uses the optical lever detection method developed by Meyer and Amer. The deflection signal is produced by focusing the output of a laser diode to a spot on the end of the cantilever and measuring the reflected light from this spot with a photodetector. The photodetector is two element devices. As the cantilever deflects, more light will be directed toward either the top or bottom detector (depending on the direction of deflection) and the resulting imbalance in the quantity of the light from two detectors can be used as an error signal proportional to the deflection of the cantilever. While theoretically not as sensitive as the interferometric method, this method has the advantage in that is simple, robust, and allows removal of optical components from the area near the sample and tip.

Imaging in the electrochemical environment with the AFM has a number of advantages. In contract to the STM, almost any type of surface can be imaged with the AFM in almost any electrochemical region. While in the STM electrochemical processes on the tip and specific electrochemical phenomena occurring between the sample and tip cause serious problems, in the AFM we can obtain stable image even when substantial faradaic currents are being passed at the sample surface. In contract to almost all other technique which have been adapted to investigate the solid-liquid interface, the AFM is

most suitable technique to observe the surface structure in electrolyte solutions. In air, such a large force as 10^{-7} N is required for imaging stable because of the presence of contamination layer, namely, water films on the sample and tip. Capillary forces from water adsorbed onto the tip can cause the tip to adhere into the surface when the tip comes to the surface, and meniscus forces act during the separation. As a result, since high repulsive forces act to the sample surface, softer materials such as organics and biologics adsorbed onto metal surface are substantially difficult to image in air. In water, adhesive forces between the sample and tip decrease to the order of 10^{-9} N because adsorptive forces from water are isotropically dispersed and, therefore, meniscus forces can be negligible.

One of the drawback to the technique is the lack of appropriate theory to describe the imaging mechanism. If the interaction is truly between a single atom in the tip and a single atom on the electrode surface, then with an imaging force of 10^{-9} N (a relatively low value) the pressure between the two would approach 10^{10} Pascal [48-50]. This is clearly not physics. One reason for this lack of specific insight into the imaging mechanism is the dearth of AFM information obtained in UHV where well-defined surface and tips are available. The imaging mechanism may also be modified as different force interact with the tip and sample in different environments.

Finally, the AFM image lacks the spectroscopic insight associated with STM images. STM images potentially contain not only topographic information, but also hold details of the density of states in the sample and tip. While accessing this data can be quite problematic for STM measurements in the electrochemical environment, substantial insight has been obtained in UHV. For the AFM, different materials (and atoms) will have different repulsive interactions with a given tip, but extracting this information will be quite different.

1.5 Surface X-ray Diffraction (SXRD)

The arrangement of atoms at solid/liquid interfaces is of fundamental importance, since the atomic structure strongly affects the chemical and physical properties of the interfaces. Despite this importance, our knowledge of atomic structure at electrochemical interfaces is rather poor due to the difficulty of *in situ* structure determination. In

particular, *in situ* study of "buried" interface such as the second and the third layer have not been much progressed, although STM and AFM can provide very useful information on the most top atoms of the interface structure. X-ray scattering is, however, useful for *in situ* studies of such "buried" interfaces and substantial progress has recently been made in determining the atomic structure at solid/electrolyte interface [51-56].

Hard X-rays are well suited for *in situ* measurements of the interface structure. X-rays have a large penetration depth in electrolyte solution, and X-rays interact weakly with matter, the intensity data can be interpreted kinematically, which greatly simplifies data analysis compared to electron diffraction. Furthermore, X-ray wavelengths are comparable to atomic distances. Thus, X-ray diffraction provides information on atomic scale, although it is necessary that the atomic order extends over a long range.

The drawback of the weak interaction between X-rays and matter is that the signals have low intensity. This is remarkably for surfaces and interfaces, since these contain only a small number of atoms. On the other hand, the weak interaction of X-ray with matter provides an additional advantage for measurements of structures that are the "buried" interfaces, since it results in a large penetration depth. Thus, X-ray can be to probe "buried" interfaces, unlike many other surface science techniques routinely used in vacuum. Indeed, X-ray diffraction has been successfully applied *in situ* studies of electrochemical systems.

However, X-ray diffraction has received considerably less attention in electrochemistry than both the *in situ* scanning probe techniques and ex situ techniques such as LEED following transfer into vacuum. Because of the low scattering cross section of atoms, and since both conventional X-ray tubes and rotating anode sources provide relatively low photon fluxes, probing the structure of surfaces and interfaces has required excessively long acquisition times. However, this problem can be overcome with the use of the intense radiation from synchrotron sources, which have opened a new avenue of research into structure measurements at surfaces and interfaces.

Synchrotron radiation greatly makes easily the execution of the surface X-ray scattering experiments and makes possible experiments that are impossible with conventional sources. For X-ray diffraction, the brightness, instead of the total photon flux, is the important characteristic quantity. Brightness is defined as the total number of

photons emitted per sec per unit solid angle per unit source area. High brightness is favorable when high spatial and angular resolutions needed, because high brightness corresponds to a large photon flux into a small spatial and angular region. Since a small grazing incidence angle is used for surface scattering experiments, the projected sample size is quite small, and the very high brightness of synchrotron radiation compared to conventional source is a great advantage. Another characteristic of synchrotron radiation that is important for X-ray scattering is its high collimation (~ 0.2 milliradian (mrad) = 0.012°). This contributes to the high brightness and permits a high flux for high resolution experiments. For experiments probing the solid/liquid interface, high energies are usually selected, since the absorption cross-section of water is smaller than at lower energies.

In the following sections, basic principles of in plane X ray diffraction are described.

1.5.1 Basic Principles of In-plane X-ray diffraction [57,58]

A crystal has long-range transitional order and is composed of a periodic array of identical structure unit. The periodic array is described in terms of a lattice, and each unit cell occupies a certain site on that lattice. All the atoms in the crystal fall on sets of parallel lattice planes, and in the Bragg approach, the crystal is imagined as consisting of sets of these planes, which are spaced a distance d apart. This construction is illustrated in Fig. 1.5. X-rays that are incident on the planes wire an angle θ have a small fraction (~ 10^{-4} - 10^{-2}) of

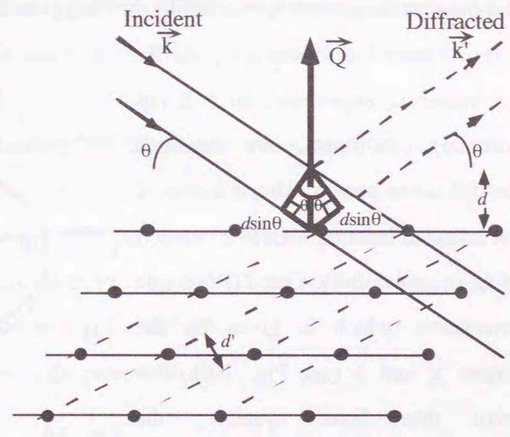

Fig. 1.5 Bragg refection from lattice planes with spacing d. The wave vector of the incident X-rays (shown by the solid line) is k and makes an angle θ with the lattice planes. The small portion of the incident beam that is specularly reflected is shown by the dashed lines and has wave vector k'. The scattering vector is $Q = (4\pi/\lambda)\sin\theta = 2\theta/d$. A set of planes with spacing d' is also shown.

their incident radiation spectrally reflected at the same angle. A peak in the intensity of the scattered radiation will occur when reflections from successive planes interfere constructively. Since the path length difference between planes is $2d\sin\theta$, the condition for constructive interference is

$$n\lambda = 2d\sin\theta \qquad (1.6)$$

when n is an integer and λ is the X-ray wavelength. This is the well-known Bragg's law.

When discussing X-ray diffraction, it is convenient to define the scattering vector

$$\mathbf{Q} = \mathbf{k'} - \mathbf{k} \qquad (1.7)$$

where k and k' are the incident and scattered wave vectors and are shown in Fig. 1.5. Since X-ray scattering is elastic, they have the same magnitude $k = k' = 2\pi/\lambda$, and thus, the magnitude of **Q** is

$$Q = (4\pi/\lambda)\sin\theta. \qquad (1.8)$$

Using Equation (1.6) one can see that an alternative formation of Bragg's law is $Q = 2\pi/d$. In addition, when the diffraction condition is satisfied, **Q** is perpendicular to the lattice planes, as shown in Fig. 1.5. An advantage of using **Q** rather than the Bragg angle θ_B is that the scattering vector Q that fulfills the Bragg condition is independent of λ, unlike θ_B.

Figure 1.6 shows a typical X-ray scattering experiment. In a X-ray scattering experiment, one measures the diffraction pattern. This is a map of the scattered intensity I(Q) as a function of Q, or equivalently, Q and the sample orientation, which is given by the angles χ and ϕ (see Fig. 1.6). For most thin layer systems, the kinematics approximation is valid, and

$$I(\mathbf{Q}) = I_e \left| \int \rho(\mathbf{r}) e^{i\mathbf{Q}\cdot\mathbf{r}} d^3\mathbf{r} \right|^2, \qquad (1.9)$$

where r(r) is the electron density of the material and Ie is the scattering intensity of a single electron. This simple Fourier-transform relation between intensity and electron density is a great advantage of X-ray scattering compound to the electron diffraction. A complicated dynamically treatment is need to calculate intensity. Note that since materials with low atomic number elements tend to have small electron densities, surface X-ray diffraction will be rather insensitive to these.

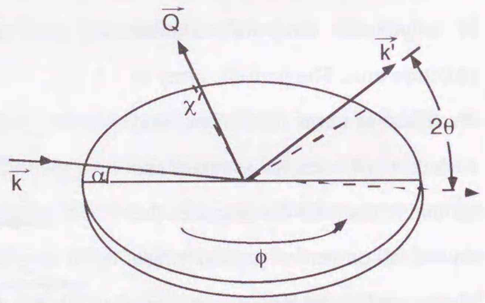

Fig. 1.6 Schematic representation of a X-ray scattering experiment. The incident and diffracted wave vectors are k and k', respectively, and the scattering vector is Q = k' - k. The sample orientation is given by the azimuthal angle ϕ and the polar angle χ.

1.6 Outline of the Present Thesis

The outline of the present thesis is as follows.

Chapter 2 describes the experimental details of pre-treatment of substrates and apparatus and procedure for measurements.

In **Chapter 3**, tip current voltammetry (TCV) is used to investigate the effect of various surface treatment of *n*-GaAs(100) on surface state density and the electron transfer characteristics between the treated substrates and the STM tip.

Chapter 4 treats InSe single crystal surface structure in air and in electrolyte solution with atomic resolution by using AFM.

In **Chapter 5**, Electrochemical AFM is used to observe the surface structure in atomic resolution and to monitor the electrochemical dissolution and tip induced surface modification of GaAs(100).

In **Chapter 6**, Cu electrochemical deposition on GaAs(100) surface is investigated by electrochemical AFM.

In **Chapter 7**, an attempt is made to observe electrochemical reaction on semiconductor surface in electrolyte solution by using SXRD. An SXRD study is carried out to monitor anodic dissolution process of *p*-GaAs(100).

Finally, **Chapter 8** summarizes the present results.

References

1) W.H. Brattain and G.G.B. Garett, *Bell. Sys. Tech. J.*, **34**, 129 (1955).
2) M. Green, in *Modern Aspects of Electrochemistry*, No. 2, Ed. by J.O'M. Bockris, Butterworths, London, pp. 343-407 (1959).
3) H. Gerisher, in *Advances in Electrochemistry and Electrochemical Engineering*, Vol.1, Ed., by P. Delahay, Interscience, New York, pp139-232 (1961).
4) P. J. Holmes, Ed., *The electrochemistry of Semiconductors*, Academic, London, (1962).
5) V. A. Myamlin and Y. V. Pleskov, *Electrochemistry of Semiconductors*, Plenum Press, New York, (1967).
6) S. R. Morrison, *Electrochemistry at Semiconductor and Oxidized Metal Electrodes*, Plenum Press, New York, (1980).
7) Y. V. Pleskov and Y. Y. Gurevich, *Semicondutor Photoelectrochemistry*, Ed., by P.N. Bartlett, Consultans Bureau, New York, (1986).
8) K. Uosaki and H. Kita, in *Modern Aspects of Electrochemistry*, No. 18, Eds., by R.E. White, J.O'M. Bockris, and B.E. Conway, Butterworths, London, (1986).
9) A. Fujishima and K. Honda, *Nature*, **238**, 37 (1972).
10) H. Gerischer, *J. Electroanal. Chem.* **58**, 263 (1975).
11) M. Datta and L. T. Romankiw, *J. Electrochem. Soc.* **136**, 185C (1989).
12) H. Beneking, *J. Electrochem. Soc.* **136**, 2680 (1989).
13) R. Reineke and R. Memming, *Surf. Sci.* **192**, 66 (1987).
14) P. Allongue and E. Souteyrand, *J. Vac. Sci. Technol. B* **6**, 1644 (1987).
15) J. J. Kelly, J. M. G. Rikken, J. W. N. Jacobs, and A. Valster, *J. Vac. Sci. Technol. B* **6**, 48 (1988).
16) M. M. Kühne and J. Schefold, *Ber. Bunsenges. Phys. Chem.* **92**, 1430 (1988).
17) J. Li and L. M. Peter, *J. Electroanal. Chem.* **199**, 1 (1986).
18) H. H. Goossens, F. Van den Kerchove, and W. P. Gomes, *J. Electroanal. Chem.* **261**, 89 (1989).
19) H. Gerischer, *Ber. Bunsenges. Phys. Chem.* **69**, 578 (1965).
20) S. Lingier, W. P. Gomes, and F. Cardon, *Ber. Bunsenges. Phys. Chem.* **93**, 2 (1989).
21) G. C. Barker, Ber.Bunsenges. Phys. Chem. 75, 728 (1971).
22) Y. V. Pleskov, Z. A. Rotenberg, V. V. Eletsky, and V. I. Lakomov, Faraday. Diss. Chem. Soc. 56, 52 (1974).
23) H. Gerischer, *Electrochemical Acta* **35**, 1677 (1990).
24) P. Allonge, in *Advance in Electrochemical Science and Engineering*, Eds. by H. Gerischer and C. W. Tobias, Vol. 4. VCH, New York (1995).
25) J. N. Chazalviel, *Electrochim. Acta* **33**, 461 (1988).
25) G. Binnig, H. Rohrer, Ch. Gerber, and E. Weibel, *Appl. Phys. Lett.* **40**, 178 (1982).
26) G. Binnig, H. Rohrer, Ch. Gerber, and E. Weibel, *Phys. Rev. Lett.* **48**, 57 (1982).
27) G. Binnig, H. Rohrer, Ch. Gerber, and E. Weibel, *Phys. Rev. Lett.* **50**, 120 (1983).
28) S. Park and C. F. Quate, *Rev. Sci. Instrum.* **58**, 2010 (1987).
29) J. D. Todd and T. R. I. Cataldi, *Chemistry in Britain* **1991**, 525 (1991).
30) C. J. Chen, *Introduction to Scanning Tunneling Microscopy*, Oxford University Press, New York (1993).
31) A. J. Bard, H. D. Abruna, C. E.Chidsey, L. R. Faulkner, S. W. Feldgerg, K. Itaya, M. Majda, O. Melroy, R. W. Murray, M.D. Porter, M. D. Soriage and H. S. White, *J. Phys. Chem.* **97**, 7147 (1993).

32) A. A. Gewirth and V. Siegenthaler Eds., *Nanoscale Probes of the Solid/Liquid Interface*, Kluwer Academic, Dordrecht 1995.
33) R. H. Folwer and L. Nordhein, *Pro. Roy. Soc. Lond. A* **119**, 173 (1928).
34) J. Bardeen, *Phys. Rev. Lett.* **6**, 57 (1961).
35) J. Simmons, *J. Appl. Phys.* **34**, 1793 (1963).
36) J. Tersoff and D. R. Hamann, *Phys. Rev. B* **31**, 805 (1985).
37) J. Wiechers, T. Twomey, D. M. Kolb, and R. J. Behm, *J. Electroanal. Chem.* **248**, 451 (1988).
38) P. Lustenberger, H. Rohrer, R. Chistoph, and H. Siegenthaler, *J. Electroanal. Chem.*, **243**, 225 (1988).
39) K. Uosaki and H. Kita, *J. Electroanal. Chem.* **259**, 301 (1989).
40) G. Binnig, C. F. Quate, and Ch. Gerber, *Phys. Rev. Lett.* **12**, 930 (1986)
41) D. Ruger and P. K. Hansma, *Physics Today* **43**, 23 (1990).
42) D. Sarid, Scanning Force Microscopy, Oxford University, New York (1991).
43) D. Sarid and V. Elings, *J. Vac. Sci. Technol. B* **9**, 431 (1991).
44) S. R. Snyder and H. S. White, *Anal. Chem.* **64**, 116R (1992).
45) J. N. Israelachvili, *Intermolecular and Surface Force*, Academic Press, New York (1985).
46) Y. Martin, C. C. Williams, H. K. Wickramasinghe, *J. Appl. Phys.* **61**, 4723 (1987).
47) G. Mayer and N. M. Amer, *Appl. Phys. Lett.* **53**, 1045 (1988).
48) H.-J. Butt, C. B. Prater, and P. K. Hansma, *J. Vac. Sci. Tech. B* **9**, 1193 (1991).
49) A. L. Weisenhorn, P. Maivald, H.-J. Butt, P. K. Hansma, *Phys. Rev. B* **45**, 11226 (1992).
50) D. A. Grigg, P. E. Russell, and J. E. Griffith, *J. Vac. Sci. Technol. A* **10**, 680 (1992).
51) M. H. Samant, M. F. Toney, G. L. Borges, L. Blum, and O. R. Melroy, *J. Phys. Chem.* **92**, 220 (1988).
52) M. F. Toney, J. G. Gordon, L. Kau, G. L. Borges, O. R. Melroy, M. H. Samant, D. G. Wiesler, D. Yee, and L. B. Sorensen, *Phys. Rev. B* **42**, 5594 (1990).
53) B. M. Ocko, J. Wang, A. J. Davenport, and H. S. Isaacs, *Phys. Rev. Lett.* **65**, 1466 (1990).
54) J. Wang, B. M. Ocko, A. J. Davenport, and H. S. Isaacs, *Phys. Rev. B* **46**, 10321 (1992).
55) I. M. Tidswell, N. M. Markovic, C. A. Lucas, and P. N. Ross, *Phys. Rev. B* **47**, 16542 (1993).
56) B. M. Ocko, G. M. Watoson, and J. Wang, *J. Phys. Chem.* **98**, 897 (1994).
57) M. F. Toney and O. R. Melroy, in *Electrochemical Interfaces*, Ed. H. D. Abruna, Sec.3, VCH, New York (1991).
58) C. A. Melendres and A. Tadjeddine Eds., *Synchrotron Techniques in Interfacial Electrochemistry*, Kluwer Academic, Dordrecht (1992).

CHAPTER 2

EXPERIMENTAL

CHAPTER 2
EXPERIMENTAL

2.1 Chemicals

Reagent grade chemicals and water purified by Mill-Q purification system (Milli Pore coop.) were used for the preparation of electrolyte solutions and solutions for etching and surface treatment. Hydrochloric acid (HCl, 36 %), sulfuric acid (H_2SO_4, 97 %), perchloric acid ($HClO_4$, 70 %), nitric acid (HNO_3, 61 %), hydrogen peroxide (H_2O_2, 30 %), copper (II) sulfate, pentahydrate ($CuSO_4 \cdot 5H_2O > 99.5$ %), cupric chloride, dihydrate ($CuCl_2 \cdot 2H_2O > 99$ %), sodium sulfide ($Na_2S \cdot 5H_2O > 99.5$ %), acetone (CH_3COCH_3, 99.5 %), and ethanol (C_2H_5OH, 99.5 %) purchased from Wako Pure Chemicals were used without further purification. "Ammonium Sulfide Solution, Yellow ($(NH_4)_2S_x$ x = 1.2)" purchased from Kanto Chemical was used for "Sulfur treatment". Ruthenium solution ($RuCl_3 \cdot nH_2O$) was prepared with 1g of $RuCl_3 \cdot nH_2O$ (Aldrich) in 10 cm^3 water. For ohmic contact, indium (In, 99.98 %) and zinc (Zn, 99.97 %) purchased from Wako Pure Chemicals were used.

The electrolyte solutions were dearated by passing high purity nitrogen gas prior to each experiment for at least 20 min.

2.2 Semiconductor Electrodes

2.2.1 GaAs

The (100) face of *n*-GaAs doped with Si (0.8 x 10 cm^{-3}) (Laser Diode, Inc.) was used as the electrode for TCV measurement. An In metal was soldered on the back side of the sample for the ohmic contact. Three different surface treatments were employed. The "etched" *n*-GaAs electrode was prepared by etching the GaAs surface with HCl - HNO_3 (1:1) solution at room temperature [1] followed by thorough rinsing with Milli-Q water. The electrode was then etched with H_2SO_4 - H_2O_2 - H_2O (4:1:1) at 50℃ [2,3]. The electrode was finally rinsed with Milli-Q water. The "Ru-treated" electrode was obtained by dipping the etched electrode in $RuCl_3 \cdot nH_2O$ solution for 30 min followed by thorough rinsing with Milli-Q water [4]. The "S-treated" *n*-GaAs electrode was obtained by immersing the etched *n*-GaAs electrode in aqueous solution of $(NH_4)_2S$ with excess S

(Kanto Chemical) overnight followed by thorough rinsing with pure water [5,6].

Single crystalline Zn doped *p*-GaAs(100) (1.25 x 10^{19} cm^{-3} or 1.5 x 10^{19} cm^{-3}) and Si doped *n*-GaAs(100) (2.0 x 10^{17} cm^{-3}) wafers, which were donated by Mitsubishi Chemical Corp., were used as samples for AFM and SXRD study. Prior to experiments, samples were cleaned in hot acetone and ethanol for 30 sec. Figure 2.1 shows an AFM image of as-received GaAs(100) surface used in this study, showing a very flat surface over a wide region. In some cases, the samples were then etched in H_2SO_4 - H_2O_2 - H_2O (5:1:1) at 0 ℃ for 30 sec [2,3] and rinsed with Milli-Q water. In other cases, the samples were used without etching treatment. Ohmic contacts were made by using an In-Zn alloy for *p*-type and an In for *n*-type GaAs.

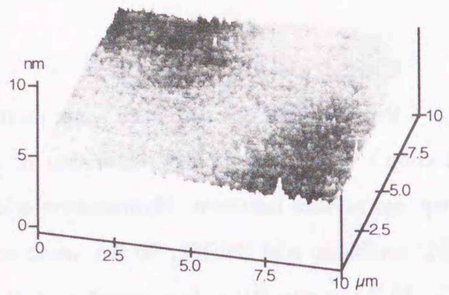

Fig. 2.1 An AFM image (10 μm x 10 μm) of an as-received *p*-GaAs(100) surface.

2.2.2 CdS

The (0001) *n*-type CdS (1.01 x 10^{17} cm^{-3}) purchased from Teikoku Tsushin Kogyo was used as a sample. The surface was etched with concentrated HCl solution for 60 sec [7] and then rinsed with Milli-Q water. The ohmic contact was obtained by soldering with an In.

2.2.3 InSe

The (0001) face of *p*-type (ca. 0.1 % Zn doping) and *n*-type (undope) InSe single crystals grown by Brigman-Stockbarger method from the $In_{1.12}Se_{0.88}$ liquid phase were donated by Dr. Chevy [8]. Before each experiment, a clean surface was obtained by removing some layers by using adhesive tape. Both *p*-type and *n*-type materials were examined in air but only the *p*-type material was used for electrochemical investigation. Ohmic contact was secured by an In - Zn alloy.

2.3 TCV Measurement

A block diagram of the TCV system is shown in Fig. 2.2 (a). A scanning tunneling microscope (STM) used in this study was a NanoScope I of Digital Instruments (CA, U.S.A.) which uses a tube scanner for movement of tunneling tip in the X, Y and Z directions. The tunneling tip is connected to ground through a 1 MΩ resistor and to a pre-amplifier which acts as a voltage amplifier [9]. Thus, the tunneling current was measured as the voltage drop across the 1 MΩ resistor. The output of the pre-amplifier is connected to a feed back circuit [10,11].

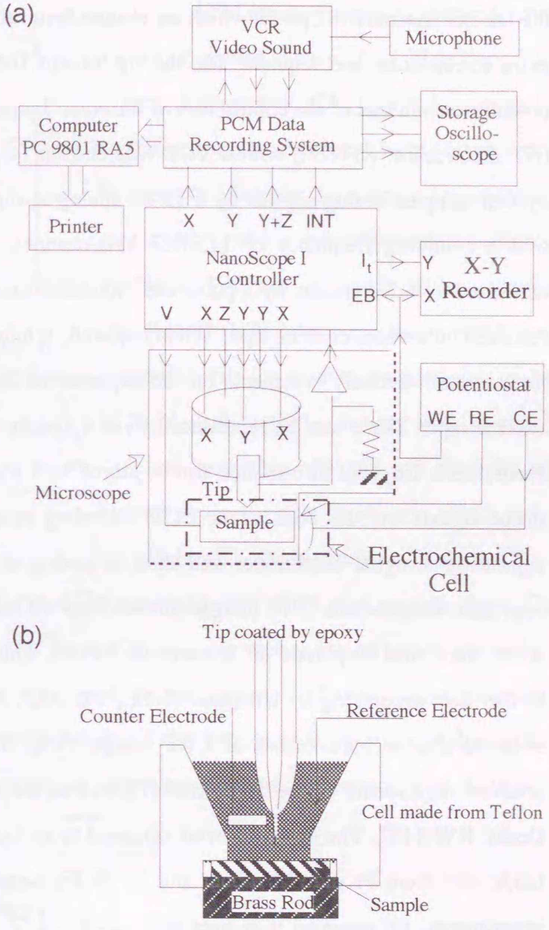

Fig. 2.2 (a) Block diagram of the TCV system. (b) Electrochemical STM cell.

To control the potential of the tip and the sample with respect to the reference electrode and carry out electrochemical reactions, a potentiostat was constructed. A schematic diagram of the potential control circuitry is shown in Fig. 2.3 [10]. It is essentially that of a well known four-electrode potentiostat (bipotentiostat) commonly used for rotating ring-disk electrode work [12] and is similar to that of Itaya and Tomita [13] and that of Siegenthaler [14]. The reference electrode (RE) and the counter electrode (CE) outputs of the potentiostat are connected directly to the reference electrode and the counter electrode of the cell, respectively. In the present work, an Ag/AgCl and a Pt wire were used as the reference

and counter electrode, respectively. The working electrode (WE) output is connected to the base of the microscope on which an electrochemical cell (Fig. 2.2 (b)) is placed. No extra connections are required for the tip except for connecting the ground of the potentiostat and that of the control unit of the NanoScope I. A PCM data recording system (NF Electronics, RP-880) with a VCR was chosen for continuous data recording. This system samples analog signals by a 12-bit analog-to-digital converter (max. 4 channels) with a sampling frequency of 115.085 kHz/channel. The sampled digital signals are converted to video signals by a pulse code modulation (PCM) and sent to the VCR to be recorded on a video cassette tape. When required, while recording video signals, one can record simultaneously comments on the experiments on the sound portion of the video cassette tape. These can be reproduced over a speaker of the system during playback. More than 1 Gbyte of information can be stored very economically. During playback, the stored signals are sent back to the PCM recording system and first converted to digital signals by a signal conditioner and then to analog signals by 12 bit digital-to-analog converter. Played-back STM images can be observed by using a storage oscilloscope and at the same time displayed on a computer screen. This system has a digital output for further data processing by computer (NEC, PC-9801 RA5). Thus, STM images can be obtained also as hard copies of CRT images from the computer. The semiconductor potential dependence of the tip current (TCV) was recorded on an X - Y recorder (Rika Denki, RW-11T). The tips used were obtained from Longreach Science Resources (ME, USA) and were Pt + Ir (80 % Pt and 20 % Ir) insulated with epoxy. In most of the experiments, tip potential was kept at 0.0 V *vs.* Ag/AgCl. The electrochemical cell was *ca.* 10 mm in diameter and *ca.* 5 mm high and made from Teflon. The working electrode was soldered to a brass rod which was in contact with the base plate of the STM microscope and this, turn, was in contact with the working electrode output from the potentiostat.

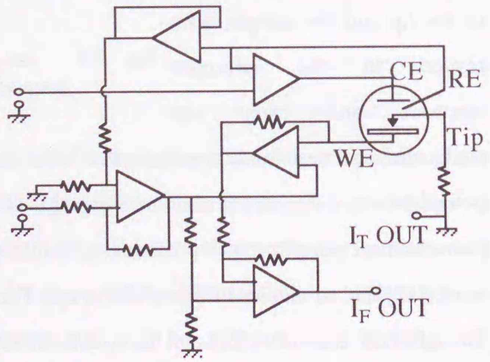

Fig. 2.3 Schematic illustration of the electronic circuit.

2.4 AFM Measurement

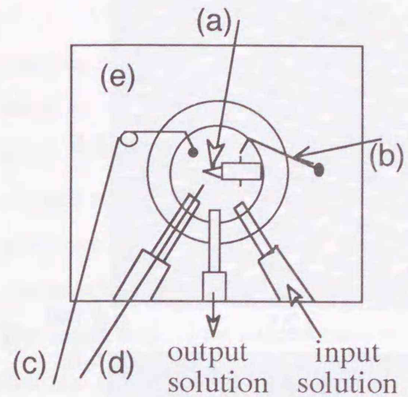

Fig. 2.4 Electrochemical AFM cell. (a) Cantilever, (b) Cantilever clip, (c) Counter electrode, (d) Reference electrode, (e) Cell made of glass

AFM measurements were carried out by using a NanoScope II or NanoScope E (Digital Instruments, CA, U.S.A.) in constant repulsive force mode. An A-head (scan size = 0.7 μm) or a D-head (scan size = 13 μm) was employed and microfabricated Si_3N_4 cantilever 100 μm in length with a spring constant of 0.58 N/m were used. AFM tips integrated with the cantilevers were also made of Si_3N_4 and were 4 μm long with nominal radii of less than 40 nm. A potentiostat system and a glass fluid cell (Fig. 2.4) supplied by Digital Instruments (volume : 0.2 ml) was used for the electrochemical AFM measurements. A Pt wire and an Ag/AgCl (3.3M KCl) electrode or an Ag wire were used as a counter and a reference electrode, respectively. When the Ag wire was used as the reference electrode, the electrode potential was corrected by comparing the shape and current peak position of the cyclic voltammograms of the same samples in the same solution measured with Ag/AgCl

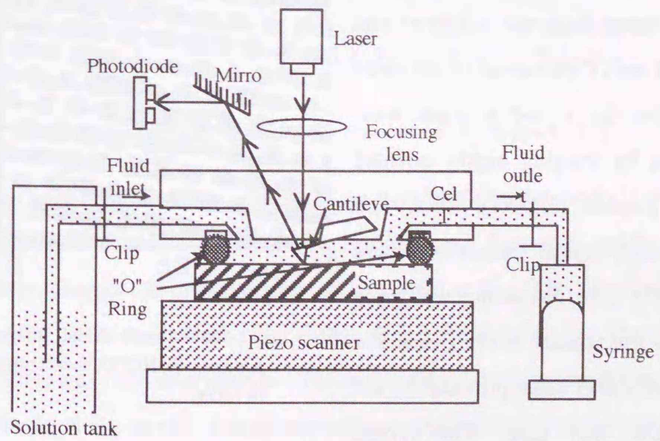

Fig. 2.5 Schematic illustration of electrochemical AFM.

electrode. The Ag wire reference electrode was used because in the case of Ag/AgCl electrode measurement did not last for long time as air bubbles were gotten into the cell and the solution within the AFM cell was not replaced. All the potentials in this thesis are given with respect to the Ag/AgCl electrode. The electrolyte solution was introduced into the electrochemical AFM cell from a solution tank through an input tube made from Teflon by pulling a syringe which was connected to an output tube of the cell as shown in Fig. 2.5. Both output and input tubes were closed by clip after the cell was filled with the solution. Thus, the electrolyte solution in the electrochemical AFM cell was never in contact with air. The exposed electrode area in contact with the solution was about 0.32 cm^2. Calibrations of the piezo scanners for the x and y plane were carried out by imaging highly oriented pyrolytic graphite (HOPG), mica, and Au(111) single crystal surface in air and in water (Fig. 2.6). No attempt was made to calibrate the scanner in the z direction and the calibration value provided by the manufacturer was used. The typical applied force during the measurements was ca. 10 nN in air and less than 1 nN in solution. For a surface modification, the typical applied force was about 10 nN.

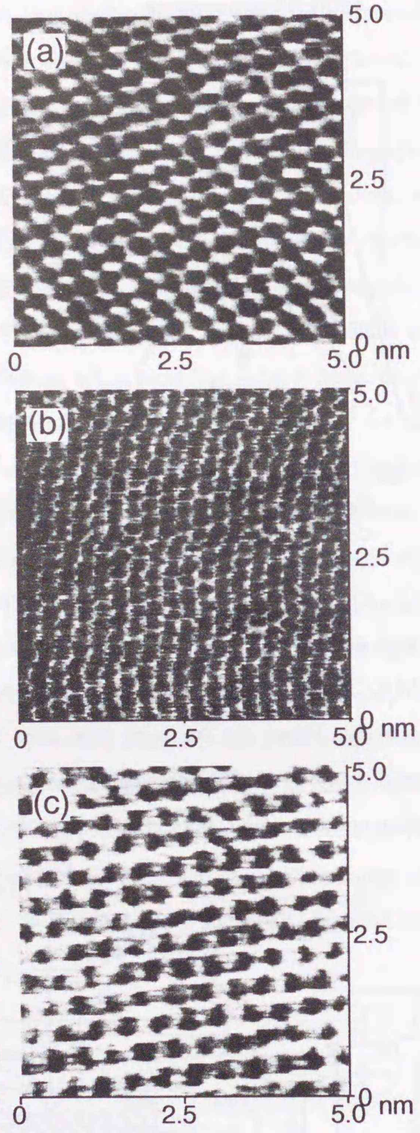

Fig. 2.6 Atomic scale AFM images of (a) Au(111), (b) HOPG, and (c) mica obtained in water.

2.5 SXRD Measurement

SXRD experiments were carried out on the 53-pole permanent magnet wiggler beamline 16A at the Photon Factory of National Laboratory for High Energy Physics shown in Fig. 2.7. The X-ray was focused with a toroidal focusing mirror. An Incident X-ray wavelength of 1.488 Å was selected by using a Si(111) double crystal monochromator. At a typical electron current in the storage ring of 250 mA, beam line provides a flux of approximately 5 x 10^{11} photons•sec^{-1}•cm^{-2}. The incident X-ray beam was collected by a mirror which consist of a quartz coated with a vapor deposited gold. The glazing angle of the incident beam was set at 0.40° (*i.e.*, 7 mrad), which is a little less than the critical angle for a total external reflection of X-rays at the GaAs(001) electrode/electrolyte solution interface. The incident X-ray beam intensity was monitored by an ionization chamber in order to normalize the intensity of the detected X-ray intensity. The diffracted intensity was detected by a one-dimensional gas position sensitive proportional counter (PSPC) in front of which a Soller collimator was placed.

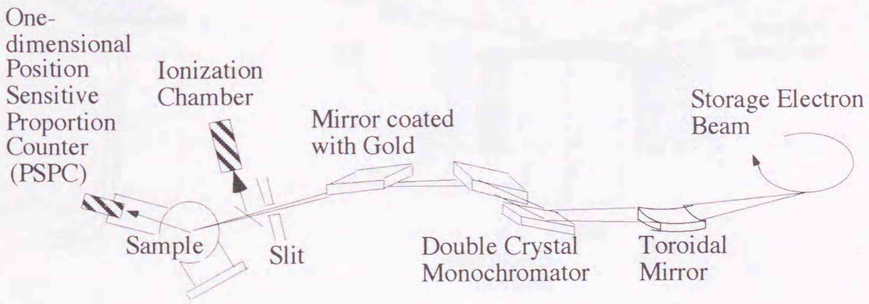

Fig. 2.7 Schematic representation of the beamline 16A at Photon Factory.

The GaAs(001) samples were fixed on the sample holder made from Teflon by using epoxy based adhesive (Ciba-Geigy, Araldite) and then was set to a specially designed electrochemical X-ray scattering cell as shown in Fig. 2.8. The electrochemical X-ray scattering cell is constructed from Teflon. A 7.5 μm thick Kapton film (Toray - Du Pont Co., 30H) was used as a window. The measurement was carried out in 0.1 M HCl solution. The applied potential was referenced to an Ag/AgCl electrode connected to the cell through a capillary tube and was controlled by a potentiostat (Toho Technical

Research, PS-07). The electrochemical X-ray scattering cell was mounted on the ϕ-axis of a two-circle diffractometer. Since it is necessary to adjust the sample orientation so that the diffractometer ϕ-axis is parallel to the normal of the sample surface in this system, the GaAs(100) sample alignment was first made ensured by checking that the positions of total reflection did not change as ϕ was rotated. When a radial scan was carried out to determinate the direction of atom rows, *i.e.*, ϕ = 0, the PSPC was set to 2θ = 10.9°(q = 1.596 $Å^{-1}$), corresponding to the position expected from bulk crystal structures. The structure of GaAs(001) has the cubic, zinc-blend unit cell (a = 5.654 Å) and the surface has square lattice [15]. The distance between the atom rows was obtained by a azimuthal scan by fixing ϕ = 0. The data were collected for the diffraction from the GaAs(001) single crystal when a high resolution transverse (θ – 2θ) scan along the direction ϕ = 0 was carried out.

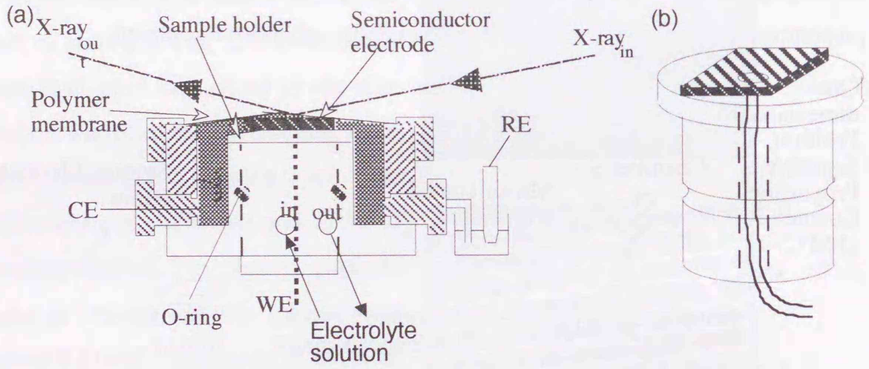

Fig. 2.8 (a) Electrochemical X-ray scattering cell. (b) Sample holder.

References

1) P. A. Kohl and A. J. Bard, *J. Am. Chem. Soc.*, **99**, 7531 (1977).
2) S. Iida and K. Ito, *J. Electrochem. Soc.*, **118**, 768 (1971).
3) D. W. Shaw, *J. Electrochem. Soc.*, **128**, 874 (1981).
4) K. Uosaki and H. Kita, *Chem. Lett.*, **1987**, 953.
5) J. F. Fan, H. Oigawa and Y. Nannichi, *Jpn. J. Appl. Phys.* **27**, L1331 (1988).
6) B. J. Skromme, C. J. Sandroff, E. Yablonoitch and T. Gmitter, *Appl. Phys. Lett.* **51**, 2022 (1987).
7) J. J. Kelly and R. Memming, *J. Electrochem. Soc.* **129**, 730 (1982).
8) A. Chevy, A. Kuhn, and M. S. Martin, *J. Cryst. Growth* **38**, 118 (1977).
9) NanoScope I Instruction Manual Version 1.1, Digital Instruments Inc., Goleta, CA, 1987.
10) K. Uosaki and H. Kita, *J. Electroanal. Chem.* **259**, 301 (1989).
11) K. Uosaki, M. Fukuda, and H. Kita, *Denki Kagaku* **57**, 1213 (1989).
12) A. J. Bard and L. R. Faulkner, Electrochemical Methods: Fundamental and Applications, Wiley, New York, 1980 Ch. 13.
13) K. Itaya and E. Tomita, *Surf. Sci.* **201**, L507 (1988).
14) P. Lustenberger, H. Rohrer, R. Chistoph, and H. Siegenthaler, J. Electroanal. Chem., 243, 225 (1988).
15) J.S. Blakemore, *J. Appl. Phys.* **53**, R123 (1982).

CHAPTER 3

TIP CURRENT VOLTAMMETRY (TCV) STUDY OF A VARIETY SURFACE TREATMENT AT *n*-GaAs(100)/ELECTROLYTE INTERFACE

CHAPTER 3

TIP CURRENT VOLTAMMETRY (TCV) STUDY OF A VARIETY SURFACE TREATMENT AT *n*-GaAs(100)/ELECTROLYTE INTERFACE

3.1 Introduction

Although the application of STM to metal electrodes has advanced quite significantly and several research groups have now resolved the surface structures of noble-metal electrodes [1,2], STM study of semiconductor electrodes is still limited. One of the reasons for this limitation is that semiconductor surfaces are covered with oxide in most cases [3] and there is almost no way of obtaining and maintaining a clean, defined surface in air or in solution. The other reason is that STM observation of semiconductor electrodes is not possible in certain potential regions owing to the existence of a space-charge layer which acts as an extra tunneling barrier [4]. Itaya and Tomita were the first to demonstrate the latter effect at the TiO_2/electrolyte interface, showing that tunneling is inhibited and the tip crashes onto the surface when the potential of TiO_2 becomes more positive than the flat-band potential [5]. Uosaki and co-workers have, however, found that in some cases STM measurement is inhibited only in certain potential regions and is possible if the potential is more positive and more negative than this middle region [6,7]. They have suggested that the doping density, energy gap and the existence of surface state may affect this potential region, and that the energetics of semiconductor/electrolyte interfaces may be probed by measuring the tip current as function of semiconductor potential. This method is called tip-current voltammetry (TCV).

The existence of surface state on a semiconductor surface is one of the most important issues in semiconductor electrochemistry [8]. In some cases, the surface states act as a recombination center for photoexited electron-hole pairs and, therefore, reduce the photoelectrochemical energy conversion efficiency. In other cases, however, the states act as an electron mediator between the semiconductor and the species in solution. It is suggested that the difference is caused by the energy of the surface states [9]. Therefore, it is very important to know the energy distribution of the surface states.

In this chapter, we investigated further the possibility of probing the energetics of the semiconductor/electrolyte interface. The effects of etching, Ruthenium treatment

and Sulfur treatment on the TCV behavior of the *n*-GaAs electrode are reported and the importance of the surface-state density on the tunneling property is demonstrated. TCV of the CdS electrode is also presented.

3.2 Results and discussion

3.2.1 "Etched" *n*-GaAs Electrode

Figure 3.1 shows the tip-current voltammetry of the "etched" *n*-GaAs electrode when the potential of the semiconductor electrode was scanned from positive to negative with a scan rate of 20 mV/s. In the feed-back loop the tunneling current was set to 6 nA. There were two potential regions in which the feed-back loop maintained the tip current at this value (tunneling mode): the potential of the working electrode was (a) more positive than +0.7 V, and (b) more negative than -0.25 V. Moving into an intermediate potential region, the tunneling current decreased, and the tip moved towards the electrode surface and crashed onto the semiconductor electrode. In this case, the tip was now in contact mode.

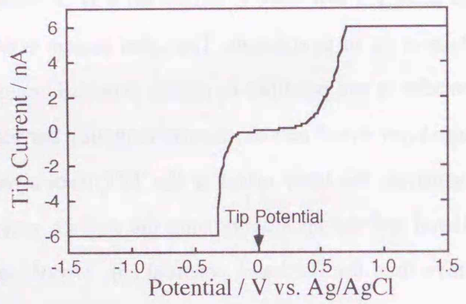

Fig. 3.1 Tip current as a function of the potential of the etched *n*-GaAs electrode in 2 mM $HClO_4$. Tip potential: 0 mV vs. Ag/AgCl. Preset tunneling current, 6 nA.

By considering the fact that the flat-band potential (U_{fb}) of the *n*-GaAs at this pH is *ca.* -0.95 V [10], and tip potential is 0 V, we can draw energy diagrams for the *n*-GaAs/electrolyte/tip system at various potentials, as shown in Fig. 3.2. When the potential is more negative than U_{fb} (Fig. 3.2(a)), the semiconductor is under accumulation conditions and there are enough carriers at the semiconductor surface to maintain the preset tunneling current. Under this condition there are essentially no differences between the STM measurement of a metal electrode and that of the semiconductor electrode. Typical STM images under this condition are shown in Fig. 3.3. Expect for small changes due to thermal drift, all images are essentially the same, suggesting that no surface change took place in this potential region.

When the potential becomes more positive than U_{fb}, a depletion layer, which should be considered as an extra barrier for the tunneling, is formed within the semiconductor. This means that the tunneling current becomes smaller at a given distance. Therefore, one expects that the tip is lowered to maintain the tunneling current and finally touches the semiconductor surface. This type of behavior was observed at TiO_2 electrodes by Itaya and Tomita [5] and at *p*-GaP electrodes by Uosaki *et al.* [6,7]. However, the result shown in Fig. 3.1 clearly indicates that the preset tunneling current flows even when the potential is more positive than U_{fb}, as much as +0.7 V *vs.* U_{fb}. The proposed energy diagram for this situation is presented in Fig. 3.2(b). Although the depletion layer

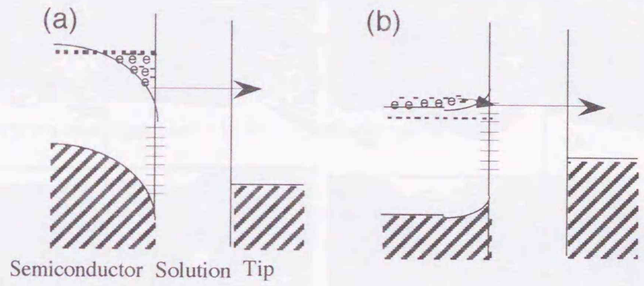

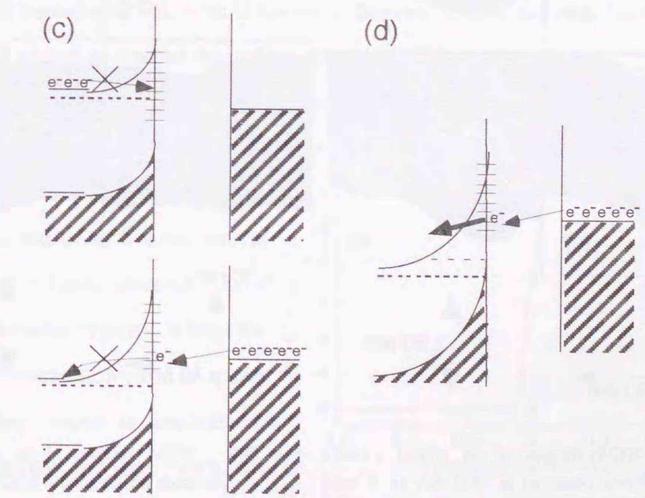

Fig. 3.2 Energetics of *n*-GaAs/electrolyte/tip interface at various potentials. (a) Accumulation region, (b) weak depletion region, (c) depletion region and (d) strong depletion/inversion region.

is formed, electrons can tunnel through the barrier because the thickness of the barrier inside the semiconductor is small owing to the relatively high doping density of GaAs employed in the present work, and the high density surface states increases the tunneling probability.

When the potential becomes much more positive (> -0.25 V), the tunneling current cannot be maintained and energy diagram shown in Fig. 3.2 (c) describes the situation. Under this condition, the depletion layer, the tunneling barrier, becomes too thick to maintain the tunneling current. The tip is now on the surface of the semiconductor

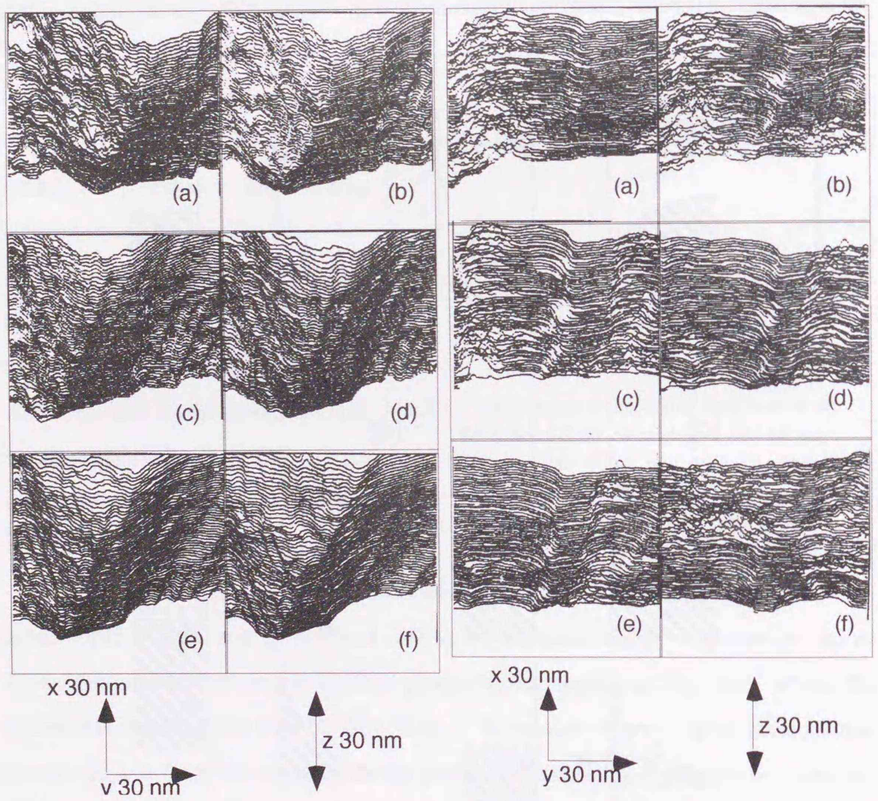

Fig. 3.3 STM images of an etched *n*-GaAs electrode observed at -900 mV in 2 mM $HClO_4$ solution. Tip potential: 0 mV vs. Ag/AgCl. Time after the application of the potential: (a) 2, (b) 4, (c) 6, (d) 8, (e) 10, (f) 12 min.

Fig. 3.4 STM images of an etched *n*-GaAs electrode observed at +1000 mV in 2 mM $HClO_4$ solution. Tip potential: 0 mV vs. Ag/AgCl. Time after the application of the potential: (a) 0.5, (b) 1, (c) 1.5, (d) 2, (e) 2.5, (f) 3 min.

and a Schottky junction is formed between the tip and the semiconductor.

The reason why the tunneling current flows at potentials more positive than +0.7 V is explained by the energy diagram shown in Fig. 3.2 (d). In this potential region the tip potential is more negative than the potential of the semiconductor and, therefore, electrons tunnel from the tip to the unoccupied state of the conduction band of the semiconductor. Although the depletion layer becomes thicker as the potential becomes more positive, the effective thickness of the tunneling barrier decreases under this condition. In this case, the surface states should play a dominant role in maintaining the tunneling current. There is also a possibility that an inversion layer is formed and electron tunneling from the tip to the hole in the valence band takes place. STM images shown in Fig. 3.4 clearly demonstrate that STM measurements are really possible in this potential region. The surface seems to change with time as the anodic faradaic current due to semiconductor dissolution flows in this potential region.

3.2.2 "Ru-treated" and "S-treated" *n*-GaAs Electrodes: Effect of Surface States on TCV

To clarify the role of the surface states on the tip current-potential behavior, the surface was treated with Ru, with is known to increase the surface state density, and with S, which is known to remove the surface states [11,12].

Figure 3.5 shows the tip current as a function of the potential for "Ru-treated" *n*-GaAs. The potential of the semiconductor was scanned from positive to negative at a rate of 20 mV/s. The preset tunneling current was 6 nA. As was the case at the "etched" *n*-GaAs electrode, there are two potential regions where the preset tip current flowed, *i.e.* where the tunneling mode is maintained. The tip current did not reach the preset value in the middle region, but this was only between -0.1 V and +0.1 V and was very narrow

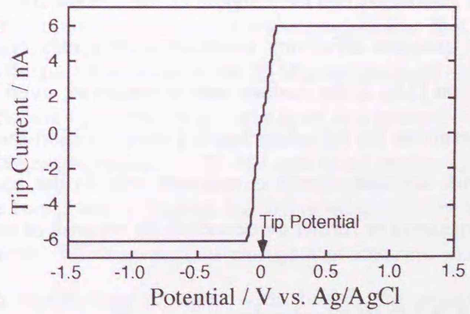

Fig. 3.5 Tip current as a function of the potential of the Ru-treated *n*-GaAs electrode in 2 mM $HClO_4$. Tip potential: 0 mV vs. Ag/AgCl. Preset tunneling current, 6 nA.

compared with that observed for the "etched" *n*-GaAs electrode. According to the model shown in Fig. 3.2, if the density of the surface states increases, the tunneling possibility should increase as well and, therefore, the potential region in which the situation shown in Fig. 3.3 (b) occurs extends to more positive potentials and the situation shown in Fig. 3.2 (d) starts to occur at less positive potential compared with the case at the etched electrode. Thus, the potential region at which tunneling is inhibited becomes very narrow.

The results shown in Fig. 3.6 are for an "S-treated" *n*-GaAs electrode. In contrast to the case of the "Ru-treated" electrode, the transition from tunneling mode to contact mode occurred at more negative potentials than for the etched electrode. The situation shown in Fig. 3.2 (d) was never achieved within the potential region employed in this work. Thus, we can conclude that the "S-treated" *n*-GaAs electrode behaves as an ideal semiconductor electrode. As mentioned before, the sulfur treatment is known to remove the surface states on GaAs, as evidenced by the increase of the photoluminescence intensity in air [13,14]. We confirmed that the removal of the surface states of GaAs in solution by showing that the quantum efficiency increases significantly, particularly in the small over potential region [15]. If the surface state is removed, even a very thin space-charge layer (which constitutes the tunneling barrier) would inhibit the flow of the preset tunneling current. Thus, tunneling mode is achieved only in the accumulation region. This result can be considered as further evidence for the removal of surface states by the sulfur treatment.

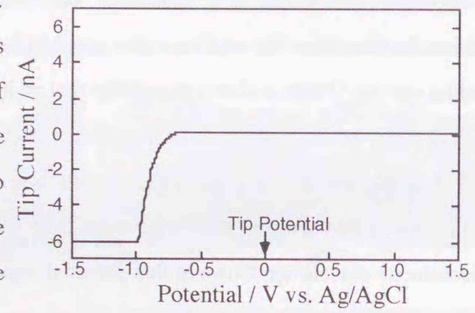

Fig. 3.6 Tip current as a function of the potential of the etched *n*-GaAs electrode in 2 mM $HClO_4$. Tip potential: 0 mV vs. Ag/AgCl. Preset tunneling current, 6 nA.

3.2.3 CdS Electrode

Figure 3.7 shows TCV of the CdS electrode. In this case the transition from the tunneling mode to the contact mode occurred at a potential very close to U_{fb}, which is *ca.* -0.85 V *vs.* Ag/AgCl [16,17]. The transition at more positive potentials was never observed and tip current was almost zero in potential region more positive than U_{fb}. This result is similar to that observed for "S-treated" *n*-GaAs. There are at least two ways to interpret this result. The first possibility is that the surface-state density is very low at the CdS electrode surface, as is the case at the "S-treated" *n*-GaAs. The second possibility is the low carrier density of CdS electrode. If the carrier density is low, the thickness of the space-charge layer at a given potential with respect to the flat-band potential is large and, therefore, the tunneling probability is low. It is impossible to distinguish between two effects from the available data. For that purpose, one needs to carry out more quantitative measurements, such as TCV measurements at a constant tip-semiconductor distance (constant-height mode).

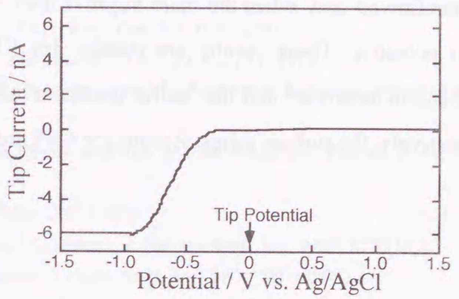

Fig. 3.7 Tip current as a function of the potential of the etched CdS electrode in 2 mM $HClO_4$. Tip potential: 0 mV vs. Ag/AgCl. Preset tunneling current, 6 nA.

3.4 Conclusion

To study the application of *in situ* electrochemical scanning tunneling microscopy (STM) measurements at semiconductor electrode surface, the tip current has been measured as a function of the semiconductor potential. It was demonstrated that the surface treatment affects very strongly the potential window for STM measurements on *n*-GaAs. At an "etched" *n*-GaAs electrode, the tip current was maintained at a present value when the potential of *n*-GaAs was more negative than -0.25 mV and more positive than +0.7 V. STM images of *n*-GaAs in the two potential regions are presented to confirm that imaging is really possible in these regions. While no surface change was observed in the negative potential region, the surface morphology changed with time in the positive-potential region. If the surface was treated with $RuCl_3$ solution, the preset tip current flowed when the potential was more positive than -0.1 V and more positive than +0.1 V. On the other hand, if the surface was treated with $(NH_4)_2S$-S solution, the preset tip

current flowed only when the more negative than -1.0 V, which is very close to the flat-band potential. These results are density for STM characterization is stressed. The "ruthenium treatment" and the "sulfur treatment" are considered to introduce and remove, respectively, the surface states. Results for CdS are also presented.

References

1) X. Gao, A. Hamelin, and M. J. Weaver, *Phys. Rev. Lett.* **67**, 618 (1991).
2) T. Hachiya, H. Honbo, and K. Itaya, *J. Electroanal. Chem.* **315**, 275 (1991).
3) S. R. Morrison, in *Electrochemistry at Semiconductor and Oxidized Metal Electrodes*, Plenum Press, New York, 1980, ch.2.
4) V. A. Myamlin and Yu. V. Pleskov, in *Electrochemistry of Semiconductors*, Plenum Press, New York, 1967.
5) K. Itaya and E. Tomita, *Chem. Lett.* **1989**, 285 (1989).
6) P. Carlsson, B. Holmström, H. Kita, and K. Uosaki, *J. Electrochem. Soc.* **283**, 425 (1990).
7) P. Carlsson, B. Holmström, H. Kita, and K. Uosaki, *Surf. Sci.* **237**, 280 (1990).
8) K. Uosaki and H. Kita, in *Modern Aspects of Electrochemistry*, ed. R. E. White, J. O'M. Bockris and B. E. Conway, Plenum, New York, 1986.
9) J. J. Kelly and R. Memming, *J. Electrochem. Soc.* **129**, 730 (1982).
10) S. R. Morrison, in *Electrochemistry at Semiconductor and Oxidized Metal Electrodes*, Plenum Press, New York, 1980, ch.7, p.289.
11) J. F. Fan, H. Oigawa, and Y. Nannichi, *Jpn. J. Appl. Phys.* **27**, L1331 (1988).
12) B. J. Skromme, C. J. Sandroff, E. Yablonoitch, and T. Gmitter, *Appl. Phys. Lett.* **51**, 2022 (1988).
13) K. Uosaki and H. Kita, *Chem. Lett.* **1987**, 953 (1987).
14) K. Uosaki and H. Kita, *J. Am. Chem. Soc.* **108**, 4294 (1986).
15) K. Uosaki and J. Ushizaki, unpublished results.
16) P. A. Kohl and A. J. Bard, *J. Am. Chem. Soc.* **99**, 7531 (1977).
17) J. H. Reeves and M. Cocivera, *J. Electrochem. Soc.* **131**, 2024 (1984).

CHAPTER 4

AFM STUDY OF SURFACE STRUCTURE AND ELECTROCHEMICAL REACTION OF InSe SINGLE CRYSTALS

CHAPTER 4

AFM STUDY OF SURFACE STRUCTURE AND ELECTROCHEMICAL REACTION OF InSe SINGLE CRYSTALS

4.1 Introduction

InSe is one of the III-VI compound semiconductors with a layered structure [1]. It has interesting properties such as strong conducting anisotropy and insensitivity of cleaved surfaces to the adsorption of foreign atoms and molecules [2,3]. These characteristics are common to all layered compounds. Furthermore, InSe has a high photosensitivity with an optimum energy gap for solar energy conversion (1.3 eV) [4]. Thus, not only optical [5,6] and electronic [6,7] properties but also photovoltaic [2,8] and photoelectrochemical characteristics of InSe have not been investigated as extensively as transition metal dichalcogenides, which also have a layered structure.

It is obvious that the chemical reactivity of InSe should be strongly affected depending upon whether the cleaved van der Waals face of the one perpendicular to the cleaved face is expected. Naturally, perfection of the surface structure is also important to determine the chemical reactivity of InSe surface. Since the step is expected to act as an efficient recombination center for electron-hole pairs generated by illumination, the surface perfection is one of the most important parameters to determine the photovoltaic and photoelectrochemical characteristics of InSe. Uosaki and co-workers have shown the importance of surface conditions with respect to photoelectrochemical properties by using laser spot scanning microscope with μm resolution [9,10]. To understand electrochemical process on InSe surface in more detail, it is necessary to obtain information about surface structure of InSe in air and in electrolyte solution with atomic resolution.

Scanning tunneling microscope (STM) is now a popular tool for imaging electrode surface with atomic resolution, and has been proved to be very useful aid to understanding the fundamentals of surface structure and electron distribution [11-18]. However, this technique is limited. Because STM uses tunneling current as a probe, only the surface of conducting materials can be imaged [19]. Moreover, STM observation of semiconductor electrodes is not possible in certain potential regions owing to the existence of a space-charge layer which acts as

an extra tunneling barrier [20]. However, atomic force microscope (AFM) can image not only conducting surface but also non-conducting surfaces [21]. Furthermore, electrochemical process on the tip which may cause serious problems in the STM measurements in electrolyte solutions can be avoided in the AFM measurements. Recently Gewirth and co-works [22-26] demonstrated that electrochemical AFM provides atomic resolution and is a useful technique for the observation of electrode surfaces *in situ*.

In this chapter, the structure of van der Waals face of InSe is determined by AFM in air with atomic resolution and the effect of imaging on the observed surface structure is discussed. Furthermore, *in situ* electrochemical AFM imaging of the van der Waals face of InSe during electrochemical reaction in solution in real time under potential control is carried out. As mentioned before, InSe has a strong conducting anisotropy with high conductivity parallel to the planes and low conductivity perpendicular to the planes; therefore STM imaging of the van der Waals face was not possible.

4.2 Results and Discussion

4.2.1 Measurement in Air

Figure 4.1 (a) shows a typical AFM image (3.01 nm x 3.01 nm) of *p*-InSe surface obtained with 16 lines/s x 200 lines/image. The hexagonal arrangement of top most atoms can be clearly seen with a distance between the closest neighbor atoms of 0.41 ± 0.01 nm. Further more, atoms which situate 0.2 nm below the first layer were also imaged as shown in sectional view (Fig. 4.1 (b)). No effect of Zn doping was observed. In some cases a much greater of small atomic smaller atomic distance was observed, but we found these results were obtained when the surface of sample was not flat.

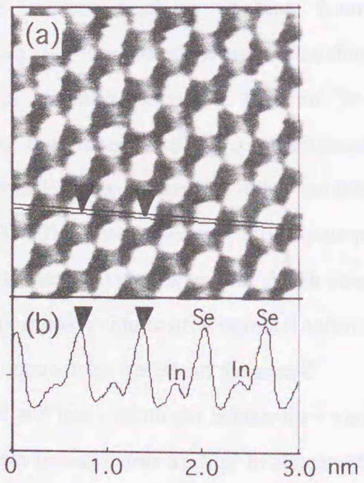

Fig. 4.1 (a) AFM top view image (3 nm x 3 nm) of van der Waals face of *p*-InSe. (b) Sectional view of the surface across the black line shown in the AFM image.

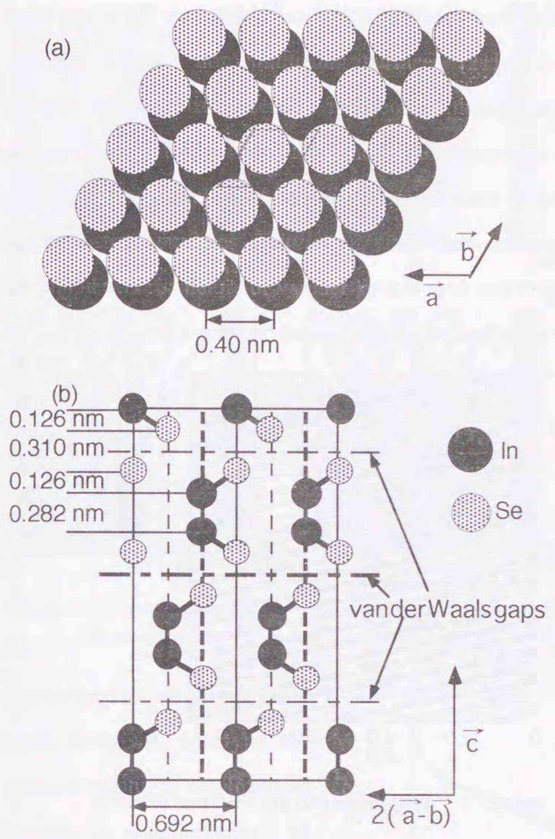

Fig. 4.2 (a) The atomic arrangement of the topmost and second of van der Waals face of InSe. (b) The stacking sequence of InSe in rhombohedral structure.

At least two structure have been proposed for InSe based on XRD analyses, *i.e.*, a hexagonal structure with unit cell of a = 0.400 and c = 1.664 nm (refs. 28, 29) and a rhombohedral structure with a = 0.400 and c = 2.485 nm [27]. In both cases each layer consists of four-layered slabs of Se-In-In-Se. The difference between the two suggested structures is the result of the different stacking sequence of the slabs. The latter structure, which is known to be the dominant structure of InSe crystal grown by the Bridgman method, is presented in Fig. 4.2. In this case, the unit cell extends over three layers. On the other hand, a two slab repletion results in hexagonal structure. As far as the AFM image of van der Waals face is concerned, no difference was expected between the two structures. The topmost and second atom layers should be Se an In, respectively. The atomic distance of the neighboring atoms of the topmost layer determined by AFM measurement was in good agreement with the value (0.4 nm) estimated from the crystal structures. The hexagonal arrangement of the topmost atoms was also observed as expected from the crystal structures. Indium atoms in second atom layer were also in hexagonal arrangement with ~0.4 nm atomic distance as expected. However, the relative position of In to Se was different from the one expected from XRD analyses. The expected vertical distance between a Se atom and the nearest In atom was 0.126 nm, but the observed distance was ~0.19 nm as shown in Fig. 4.1

(b). Horizontal distances between In atom and the nearest and second nearest Se atoms were expected to be 0.23 and 0.46 nm, respectively, but the observed values were 0.32 and 0.36 nm, respectively (see Fig. 4.2 (b)). These discrepancies should have been partly due to the irregular shape of tip that is suggested by the unsymmetrical shape of atoms which is observed in sectional view (Fig. 4.1 (b)). Furthermore, since the measurements were conducted in air, the surface was covered with some contamination and, therefore, the absolute value in the vertical direction was hard to determine. One must also note that no calibration for the z direction of the scanner was carried out. Essentially the same images were obtained for an *n*-type sample.

An almost defect-free atomic arrangement was obtained even at a wide scan (9.0 nm x 9.0 nm) as shown in Fig. 4.3. There are, however, some portions (left-hand side) where the atomic image is less clear. There are several reasons for this. One is an intrinsic defect and the other is surface contamination, The third possibility is a defect created by AFM imaging itself. Actually the atomic images became less clear by repeating the imaging for 2 min and the atoms were not resolved after 3 min of imaging. However, the atomic image was obtained if the imaging spot was changed, suggesting the failure of atomic imaging is not due to the surface contamination but due to the effect of AFM imaging itself.

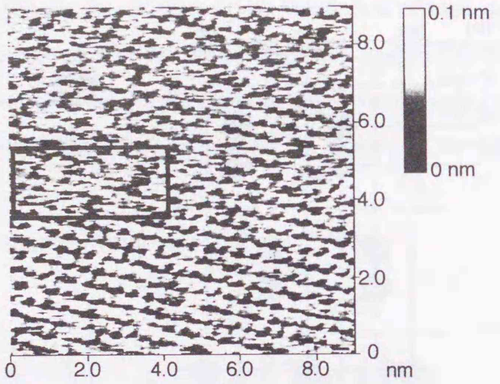

Fig. 4.3 AFM image (9.0 nm x 9.0 nm) of *n*-InSe.

Figure 4.4 shows a wide scan AFM image (500 nm x 500 nm) of *n*-InSe sequentially obtained every 40 s. It took 10 s to obtained one image (19.5 lines/s x 200 lines/image). Figure 4.4 (a) is the first image, showing that the surface is atomically flat for a very wide area. The histogram of the flatness of this image (Fig. 4.5 (a)) shows that the mean flatness is 0.05 nm and confirms the very flat surface. As the scan was repeated, the valley and hill appeared in the image and the flatness decreased as Figs. 4.4 (b) - 4.4 (f) show. There are hardly any flat parts left in Fig. 4.4 (f). The histogram of this image (Fig. 4.5 (b)) shows that the mean flatness of

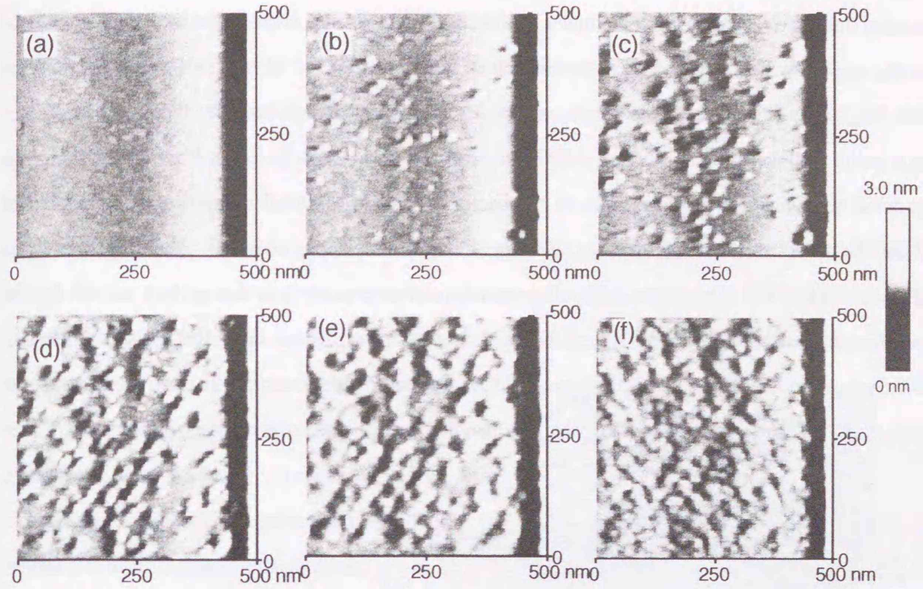

Fig. 4.4 Sequentially obtained wide scan (500 nm x 500 nm) AFM top view images of *n*-InSe. Time after of the measurement: (a) 0 s, (b) 40 s, (c) 80 s, (d) 120 s, (e) 160 s, (f) 200 s.

the surface is ~0.4 nm. One must, however, note that the absolute value of the flatness may not be reliable because of the aforementioned reasons. Thus, one can conclude that the AFM imaging itself damages the surface. In all the valley/hill structures, the left-hand side is lower than the right-hand side, *i.e.*, the left-hand side is the valley and the right-hand side the hill. It seems that theses observed structures reflect the direction of tip movement. The tip was scanned from right to left.

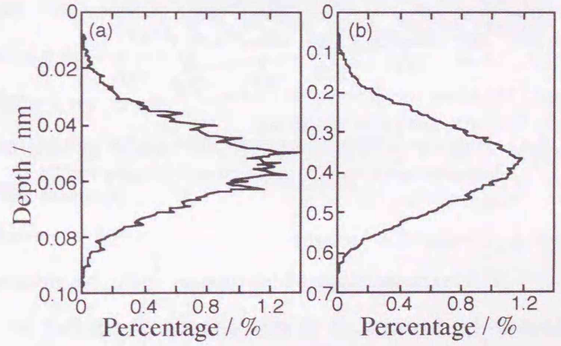

Fig. 4.5 The histogram of the flatness of 500 nm x 500 nm region of *n*-InSe (a) for Fig. 4.4 (a) and (b) for Fig. 4.4 (f).

The effect of imaging is more clearly seen in Fig. 4.6 which is a 500 nm x 500 nm line scan image of InSe after the small size (50 nm x 50 nm) imaging. In this case scanning was

carried out relatively slowly (4.3 lines/s x 200 lines/image). It is clear that a mound was created at the spot where the AFM measurement had been conducted. This result suggests that the bonding between the van der Waals layers was loosen and distance between the layers increased as a result of the scan of tip during AFM imaging. The mound observed in Fig. 4.6 was imaged as a hill and valley structure similar to the one observed in Fig. 4.5 if the image was obtained with a faster scan rate (19.5 lines/s x 200 lines/image) which was used for obtaining the images shown in Fig. 4.5. Thus, this hill/valley structure seems to contain the artifact caused by the insufficient feedback control. When the tip started to feel the mound, the piezo scanner on which the sample was placed started to shrink as a result of feedback control and the trace of the image started to go up. When the tip reaches the top of the mound, the shrink level of the scanner should stay constant. However, if the feedback cannot follow, the scanner shrinks further, *i.e.*, the mound looks higher than it actually is, and then the scanner expands because of the feedback control, *i.e.*, the image gives a valley. Since the tip was scanned from right to left, the mound was imaged as a hill on the right-hand side and a valley on the left.

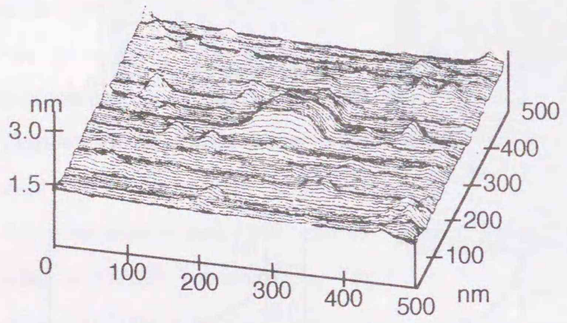

Fig. 4.6 Wide scan AFM line scan imae (500 nm x 500 nm) of *n*-InSe after small scan (50 nm x 50 nm) imaging for 2.5 min.

It is expected that stable images may be obtained by imaging with less force. Unfortunately, however, it is very difficult to conduct out imaging with lower force in air possibly due to the existence of the meniscus force. AFM imaging with less force is thought to be possible in liquid [28]. Actually, we were able to obtain atomically resolved AFM images of InSe in water and in electrolyte solution with less force (~1 nN) and images were more stable in these media [29].

The tip-induced damage reported here should not only be considered as a negative effect, because it opens up the possibility of nanofabrication of the surface with the AFM tip.

4.2.2 Electrochemical AFM observation

Figure 4.7 shows an AFM image of *p*-InSe obtained in pure water. The image obtained in water is essentially the same as that obtained in air as shown in Fig. 4.1 [30]. The topmost atoms show a hexagonal structure with a nearest-neighbor distance of 0.40 nm ± 0.03 nm. The dominant structure of InSe crystals grown by the Bridgman method is rhombohedral (Fig. 4.2) [31,32]. From this structure we can conclude that the topmost atoms should be Se which forms hexagonal arrangement with the nearest-neighbor distance of 0.400 nm. The results of AFM measurement (Fig. 4.7) are in good agreement with the surface structure expected from Fig. 4.2. In the case of small size scan, In was also observed in the second layer. Imaging in water and in solution has two advantages. First the repulsive force of tip in water (ca. 10^{-9} N) is an order of magnitude lower than in air (ca. 10^{-8} N) because of the absence of meniscus force and the reduced van der Waals interaction [27,32-34]. Second, the surface contamination is greatly reduced since the surface is covered with pure water. Thus, we could observe atomic image for longer time in water (more than 10 min) than in air (a few minutes).

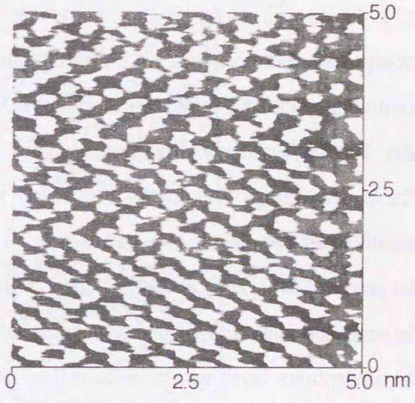

Fig. 4.7 An atomically resolved AFM image of the van der Waals face of *p*-InSe in pure water showing the hexagonal arrangement.

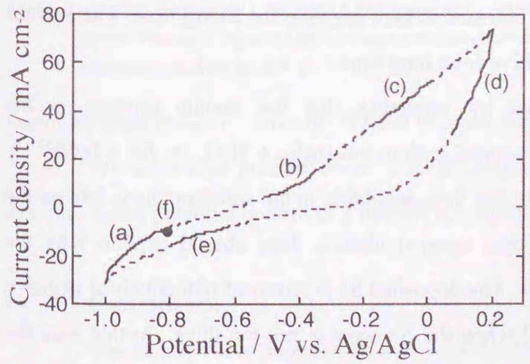

Fig. 4.8 Current-potential relation of *p*-InSe in 10 mM Na_2SO_4 in dark. Sweep rate: 15 mV/s.

Figure 4.8 shows a typical cyclic voltammogram of a *p*-InSe electrode in 10 mM Na_2SO_4 solution in dark (sweep rate, 15 mV/s). The open-circuit potential was ca. -0.5 V vs. Ag/AgCl. The anodic current was larger than the cathodic current. Under illumination, significant cathodic photocurrent due to hydrogen generation flowed at potentials more negative than

ca. -1.0 V. No illumination effect was observed for the anodic current. These results confirm that the material is a *p*-type semiconductor.

Figure 4.9 shows the AFM images obtained sequentially when the potential was scanned from -1.0 V to +0.2 V and back again at a rate of 15 mV/s. All images shown in Fig. 4.9 were obtained while tip was scanned from the top to the bottom. It took 11 s to capture one image and therefore the potential differed by 0.165 V between the top and the bottom of the image. At relatively negative potential region (< -0.5 V), the atomic image was clearly resolved (Fig. 4.9 (a)). The image is essentially the same as those obtained in air and in water (cf. Fig. 4.7). This result suggests that the surface is stable under these conditions. When potential became more positive than -0.5 V, the atomic image became less clear (Fig. 4.9 (b)). The more positive the potential was, the larger was the non-atomically resolved area (Figs. 4.9 (c) and (d)). The atomic image was completely lost at potentials more positive than 0 V (Fig. 4.9 (d)). The atomic image was partly recovered when the potential was scanned from positive to negative and became more negative than -0.7 V (Fig. 4.9 (e)) and was completely recovered if the potential was kept at -0.8 V for 1 min (Fig. 4.9 (f)). These results suggest that InSe is decomposed and amorphous layer is formed on the surface when anodically oxidized. However, the amorphous layer can be removed at negative potentials and an ordered surface one layer below appears.

If the potential was kept at +0.5 V for 2 min then pulsed to -1.0 V, atomic image was never recovered, suggesting that once the amorphous layer on the surface becomes too thick, it cannot be completely removed even if the potential is kept negative for a long time. The surface looked brown after potential was kept positive for a long time.

These results can be explained by assuming that the anodic process is the decomposition of InSe to selenium and hydrated indium ion ($InSe + H_2O \rightarrow Se + InOH^{2+} + H^+ + 3e^-$) [35,36]. Since $InOH^{2+}$ is soluble but Se is insoluble in the solution, Se is left on the InSe surface and forms an amorphous layer upon oxidation. This should explain why the atomic image was lost at positive potentials. The deposited Se is removed reductively at negative potentials ($Se + H+ + 2e^- \rightarrow HSe^-$) [36] when the Se layer is not too thick. In this case the atomically ordered van der Waals face appears and an atomically resolved AFM image can be obtained at negative potentials. If the Se layer is too thick, total removal of Se by

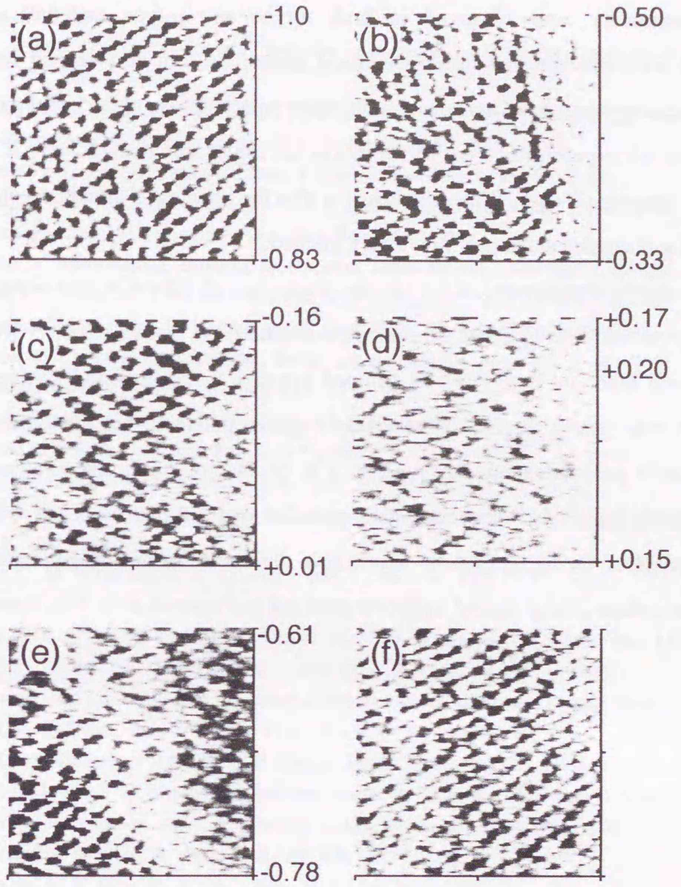

Fig. 4.9 (a)-(e): Sequentially obtained AFM images of *p*-InSe in 10 mM Na_2SO_4 while potential was scanned (a)-(e). Potential regions where images were taken are shown in Fig. 4.8. (f): Image was taken 1 min after potential was kept at -0.8 V.

electrochemical reduction must be difficult because the layer is porous and has low conductivity.

We were also able to observe AFM images of atomic resolution with a hexagonal structure under potential control in 2 mM $HClO_4$ solution.

4.3 Conclusion

The atomic force microscope was employed to observe the surface atomic structure of InSe, one of III-VI compound semiconductors with layered structures, in air and in solution.

Atomic arrangements were observed in both *n*-type and *p*-type materials. The atomic arrangements were obtained not only in topmost atoms, Se, but also second In layers. The observed structures are in good agreement with those expected from bulk crystal structures.

When the experiments were performed in air, the atomic images became less clear by repeating the imaging process. Wide area imaging after the imaging of small area clearly showed that a mound was created at the spot previously imaged.

The atomic arrangement of the van der Waals face of InSe was also observed in water and in electrolyte solutions by AFM. In electrolyte solution, the surface structure was monitored by AFM in real time and potential was scanned negative to positive and scanned back. The atomic image was clearly resolved at relatively negative potential, but the atomic image was completely lost at potentials more positive than 0 V, because of the formation an amorphous Se layer. The atomic image was recovered when potential was returned to negative (-0.7 V) as a result of removal of the Se amorphous layer. It is demonstrated that AFM is very useful for following the surface change caused by electrochemical reaction.

References

1) R. M. A. Leieth, Ed., in *Physics and Chemistry of Materials with Layered Structures*, Reidel, Dordarent-Holland, 1977, Vol. 1, p. 225.
2) V. N. Katerinchuk, Z. D. Kovalyuk, and I. V. Mintyanskii, *Sov. Phys.Solid state* **25**, 94 (1983).
3) S. M. Atakishiev and G. A. Aknumdov, *Phys. Status Solidi* **32**, K33 (1969).
4) H. J. Lewerenz, H. Gerisher, and M. Lubke, *J. Electrochem. Soc.* **131**, 100 (1984).
5) A. Segura, A. Chevy, J. P. Guesdon, and J. M. Besson, *Solar Energy Mater.* **2**, 159 (1979/1980).
6) R. W. Damon and R. W. Redington, *Phys. Rev.* **96**, 1498 (1954).
7) J. C. Merle, R. Baritiromo, E. Borsella, M. Piacetini, and A. Savoia, *Solid State Commun.* **28**, 251 (1978).
8) A. Segura, J. P. Guesdon, J. M. Besson, and A. Chevy, *J. Appl. Phys.* **54**, 876 (1983).
9) P. Carlsson, B. Holmström, K. Uosaki, and H. Kita, *Appl. Phys. Lett.* **53**, 965 (1988).
10) S. Eriksson, P. Carlsson, B. Holmström, and K. Uosaki, *J. Appl. Phys.* **69**, 2324 (1991).
11) R. Sonnenfeld and P. K. Hansma, *Science* **232**, 211 (1986).
12) A. A. Gewirth and A. J. Bard, *J. Phys. Chem.* **92**, 5563 (1988).
13) K. Itaya and E. Tomita, *Surf. Sci.* **201**, L507 (1988).
14) K. Uosaki and H. Kita, *J. Electroanal. Chem.* **259**, 301 (1989).
15) M. P. Green, K. J. Hanson, D. A. Scherson, X. Xing, M. Richter, P. N. Ross, R. Carr, and I. Lindau, *J. Phys. Chem.* **93**, 2181 (1989).
16) S.-L. Yau, C. M. Vitus, and B. C. Schardt, *J. Am. Chem. Soc.* **112**, 3677 (1990).
17) M. Szklarczyk and J. O'M. Bockris, *Surf. Sci.* **241**, 54 (1991).
18) S.-L. Yau, X. Gao, S.-C. Chang, B. C. Schardt, and M. J. Weaver, *J. Am. Chem. Soc.* **113**, 6049 (1991).
19) G. Binnig, H. Rohrer, Ch. Gerber, and E. Weibel, *Phys. Rev. Lett.* **49**, 57 (1982).
20) V. A. Myamlin and Yu. V. Pleskov, in *Electrochemistry of Semiconductors*, Plenum Press, New York, 1967.
21) G. Binnig, C. F. Quate, and Ch. Gerber, *Phys. Rev. Lett.* **56**, 930 (1986).
22) S. Manne, P.K. Hansma, J. Massie, V. B. Elings, and A. A. Gewirth, *Science* **251**, 183 (1991).
23) S. Manne, J. Massie, V. B. Elings, P.K. Hansma,, and A. A. Gewirth, *J. Vac. Sci. Technol. B* **9**, 950 (1991).
24) C-h. Chen, S. M. Vesecky, and A. A. Gewirth, *J. Am. Chem. Soc.* **114**, 451 (1992).
25) C-h. Chen and A. A. Gewirth, *Phys. Rev. Lett.* **68**, 1571 (1992).
26) C-h. Chen and A. A. Gewirth, *J. Am. Chem. Soc.* **114**, 5439 (1992).
27) A. Likforman, D. Carre, J. Etienne, and B. Bachet, *Acta Cryst. B* **31**, 1252 (1975).
28) A. L. Weisenhorn, P. Maivald, H.-J. Butt, and P. K. Hansma, *Phys. Rev. B* **45**, 11226 (1992).
29) K. Uosaki and M. Koinuma, *J. Electroanal Chem.* **357**, 301 (1993).
30) K. Uosaki and M. Koinuma, *Appl. Phys. Lett.* **74**, 1675 (1993).
31) B. Celustka and S. Popovic, *J. Phys. Chem. Solids* **35**, 287 (1974).
32) A. Likforman and M. Guittard, *Compt. Rend. (Paris)* **C279**, 33 (1974).
33) A. L. Weisenhorn, P. Maivald, H.-J. Butt, P. K. Hansma, *Phys. Rev. B* **45**, 11226 (1992).
34) D. A. Grigg, P. E. Russell, and J. E. Griffith, *J. Vac. Sci. Tech. A* **10**, 680 (1992).
35) V. V. Losev and A. I. Molodov, in *Encyclopedia of Electrochemistry of the Elements*, (Ed. A. J. Bard), Vol. VI, Marcel Dekker, New York, 1975, p. 2.
36) S. I. Zhdrarov, in *Encyclopedia of Electrochemistry of the Elements*, (Ed. A. J. Bard), Vol. IV, Marcel Dekker, New York, 1975, p. 352.

CHAPTER 5

AFM STUDY OF SURFACE STRUCTURE AND ELECTROCHEMICAL REACTION OF GaAs(100) SINGLE CRYSTALS

CHAPTER 5
AFM STUDY OF SURFACE STRUCTURE AND ELECTROCHEMICAL REACTION OF GaAs(100) SINGLE CRYSTALS

5.1 Introduction

Control and observation of electrochemical and photoelectrochemical dissolution reactions of semiconductor electrodes are very important in establishing the electrochemical/photoelectrochemical etching processes and stable photoelectrochemical cells [1,2]. GaAs is one of the most attractive semiconductor materials to be used in various electronic devices and in dry/wet solar cells. Thus, many papers on the electrochemical behaviors of GaAs in the dark and under illumination have been published [3-8].

The scanning tunneling microscope (STM) is now recognized as one of the most useful techniques for the *in situ* surface characterization of electrodes with very high resolution [9-12]. We have applied STM to monitor the surface structure change of *n*-GaAs during anodic photocorrosion [13,14]. Unfortunately, however, STM can only be applied to observe the surface of conductive samples. The existence of anodic oxide films as well as the space charge layer in the depletion condition makes the STM measurement of semiconductor electrodes relatively difficult [15] and an atomic image of the semiconductor surface in contact with the electrolyte has only been reported for H-terminated silicon and germanium in H_2SO_4 [16], HF [17], and NaOH solutions [18]. However, an atomic force microscope (AFM) can image even non-conducing surfaces. Furthermore, an electrochemical process on the tip which may cause serious problems in the STM measurements in electrolyte solutions can be avoided in the AFM measurements. Recently Gewirth and co-workers demonstrated that electrochemical AFM (ECAFM) provides atomic resolution and is a useful technique for the observation of electrode surfaces *in situ* [19-21]. In the previous chapter, AFM was successfully applied to monitor the surface structure change of the semiconductor electrode surface for the first time during electrochemical potential cycling with atomic resolution by using an InSe electrode [22].

Nano/micro-fabrication of the surface structure by scanning probe

microscopy (SPM) attracts many research groups. One of the advantages of using SPM for surface modification is that the modification process can be followed in real time. The SPM nanofabrication technique has potential applications to various technologies such as high-density information storage, high-resolution lithography, and production of nanoscale integrated chemical systems and electronic devices. Most of the surface modifications by SPM reported so far have been performed on various substrates including molecular layers such as Lamgmuir-Blodgett films [23,24] and self-assembled monolayers (SAMs) [25,26], semiconductors [27-30], metals [31-33], and layer compounds [34-36] in air or under ultra-high vacuum conditions and the modified structures were created by using the interaction between SPM tips and substrate surfaces. Recently, Schultz *et al.* [37] reported that terminal azide group of SAM on a glass slide surface was converted to amino group in hydrogen saturated isopropyl alcohol only in the regions scanned with Pt coated AFM tip. This report demonstrated that the fabrication of nanometer-sized pattern can be accomplished not only by utilizing physical interaction between the tip and the surface but also by chemical reaction catalyzed by the tip. Solid/electrolyte interface is an appropriate system for the surface modification based on tip induced chemical reaction with nanometer scale resolution, because the reaction rate can be controlled easily by changing the electrode potential [38,39] and since electrode reactions at the solid/electrolyte interface are very sensitive to the condition of the substrate surface, the reactions take place selectively at nano-structure fabricated by the tip.

Gewirth *et al.* demonstrated that the electrodeposition of Cu on Cu electrode took place selectively at the place where the AFM tip was scanned by heterogeneous nucleation and growth mechanism [40,41].

In this chapter, ECAFM was employed to observe and modify GaAs(100) surface in various electrolyte solutions under potential control. Atomic arrangement of (100)-(1x1) structure was observed at both *p*-type and *n*-type GaAs electrodes. Surface faceting at *p*-GaAs(100) in HCl solution was followed in real time. Sub-μm pattern was created by AFM tip as a result of tip-induced anodic dissolution reaction.

5.2 Results and Discussion

5.2.1 *p*-GaAs(100) in HCl solution

The as-received *p*-GaAs(100) was very flat as shown in Fig. 2.1. The sample was used as an electrode after etching treatment in H_2SO_4-H_2O_2 solution at 0℃ for 30 sec just to remove the native oxide layer on the surface. The oxide layer on the surface was not completely removed by this etching treatment and a small amount of the oxide layer seemed to be left on the surface. Thus, we applied cathodic potential (-0.6 V vs. Ag/AgCl) to the electrode to reduce the oxide layer. AFM studies showed when the cathodic potential was applied, the residual oxide layer was completely removed and the GaAs surface was exposed as the surface structure change was stopped and the atomic arrangement was observed.

Figure 5.1 shows cyclic voltammograms of *p*-GaAs electrode in 10 mM HCl in the dark. As expected for a *p*-type semiconductor electrode, a large anodic current was observed but only a small cathodic current flowed in the dark. Anodic current corresponding to the GaAs dissolution was observed at potentials more positive than +0.15 V vs. Ag/AgCl. Significant cathodic current due to hydrogen evolution flowed at potentials more negative than about -0.9 V.

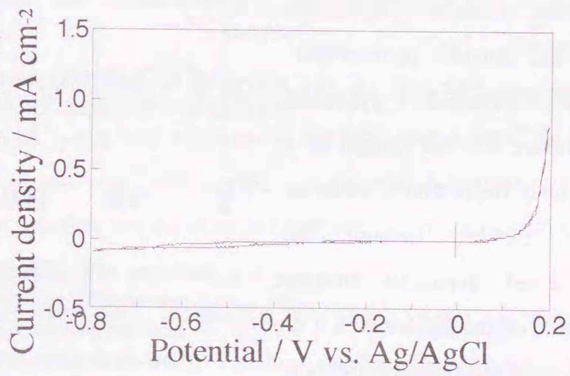

Fig. 5.1 Current-potential relation of the *p*-GaAs(100) electrode in 10 mM HCl in the dark.

When the electrode was kept at open circuit potential (~0.01 V) or at potential where small anodic current flowed in 10 mM HCl solution, truncated pyramids of relatively uniform size (50-100 nm square) were formed on the surface as shown in Figs. 5.2 (a) (top view) and (b) (cross sectional view). This structure was stable in HCl solution at 0 V where almost no current flowed for a long period of time (more than 30

min). A truncated pyramidal structure was formed only at open circuit potential or when the anodic current flowed, possibly due to anodic dissolution of the GaAs electrode in HCl, which proceeds most selectively at (111) face. The formation of the pyramids at open circuit suggests the flow of anodic current which is compensated by the cathodic photocurrent. The truncated pyramidal structure was not formed as a result of deposition of oxide on the surface, because the truncated pyramidal structure stayed on the surface even if the potential was pulsed to cathodic.

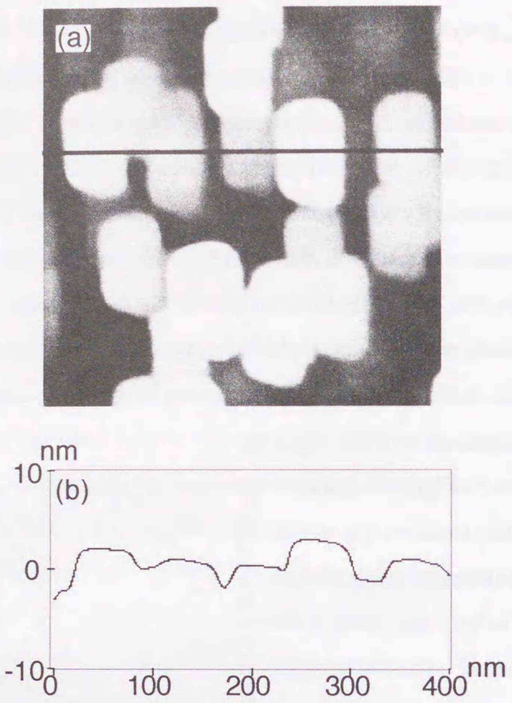

Fig. 5.2 An AFM image of the *p*-GaAs(100) surface obtained at 0 V vs. Ag/AgCl in 10 mM HCl after the anodic potential was applied (400 x 400 nm). (a) Top view and (b) Cross sectional view.

The electrochemically formed planes had an angle of about 40°~50° with respect to the (100) surface and seemed to correspond to the Ga{111} crystallographic planes which form an angle of 54.7° with respect to the (100) surface. The etching proceeds up to the Ga{111} planes because the As{111} planes are very active compared with the Ga{111} planes [42,43].

An atomic arrangement was observed on the terrace of the pyramid when the potential was kept at 0 V where almost no current flowed, as shown in Fig. 5.3. This image is shown without any filtering. The top view shows that the atomic structure exists with nearly four-fold symmetry. The topmost atoms show a nearest-neighbor distance of about 0.42 nm ± 0.04 nm, which is in good agreement with the value of the GaAs(100)-(1x1) surface [44]. Although it is not possible to tell whether the topmost atoms are As or

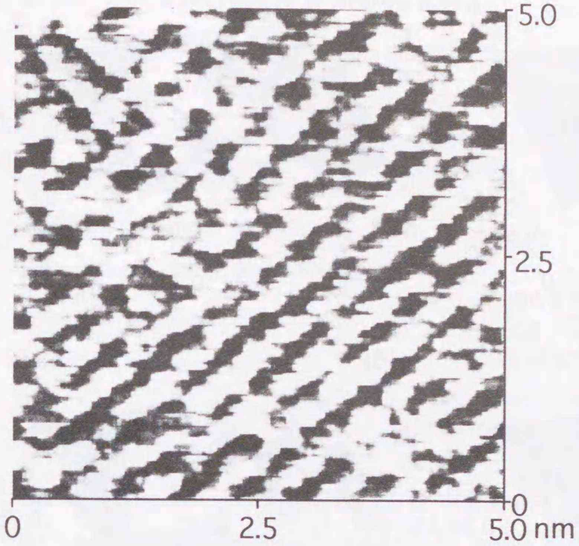

Fig. 5.3 An atomically resolved AFM image of the p-GaAs electrode surface in 10 mM HCl obtained at 0 V vs. Ag/AgCl. The structure shows (100)-(1x1) arrangement. The image was not filtered.

Ga, it seems to be Ga because XPS study shows the Ga/As ratio is higher at samples which were removed from the cell after a positive potential was applied than at samples without anodic treatment. GaAs(100) surface forms (2x4) or c(4x4) structure in UHV condition because of the existence of the dangling bond in (1x1) structure [45,46]. The XPS spectrum also shows that the Cl peak is stronger in samples with anodic treatment and, thus, we speculate that the topmost atoms are Ga terminated with Cl. This Cl termination seems to stabilize (1x1) structure.

Figure 5.4 shows an AFM image obtained at 0 V (Fig. 5.1(a)) and those obtained sequentially after the application of +0.18 V, where small anodic current due to GaAs electrode dissolution flowed (Figs. 5.1 (b)-(e)). Immediately after the application of +0.18 V, almost no surface structure change was observed. Five minutes after +0.18 V was applied, AFM images became unstable and the truncated pyramidal structures lost their shape, particularly at the borders. These results suggest that it took a few minutes to form active sites for anodic dissolution. As time passed, the height of the truncated pyramidal structures became gradually larger. One must note, however, that the pyramidal structures did not grow, but portions in the outskirts of the pyramids were removed by the anodic etching process.

We must mention that the shapes and sizes of truncated pyramids were strongly dependent on the experimental conditions, such as HCl concentration and temperature. The details will be reported elsewhere. We have also observed the atomic arrangement of

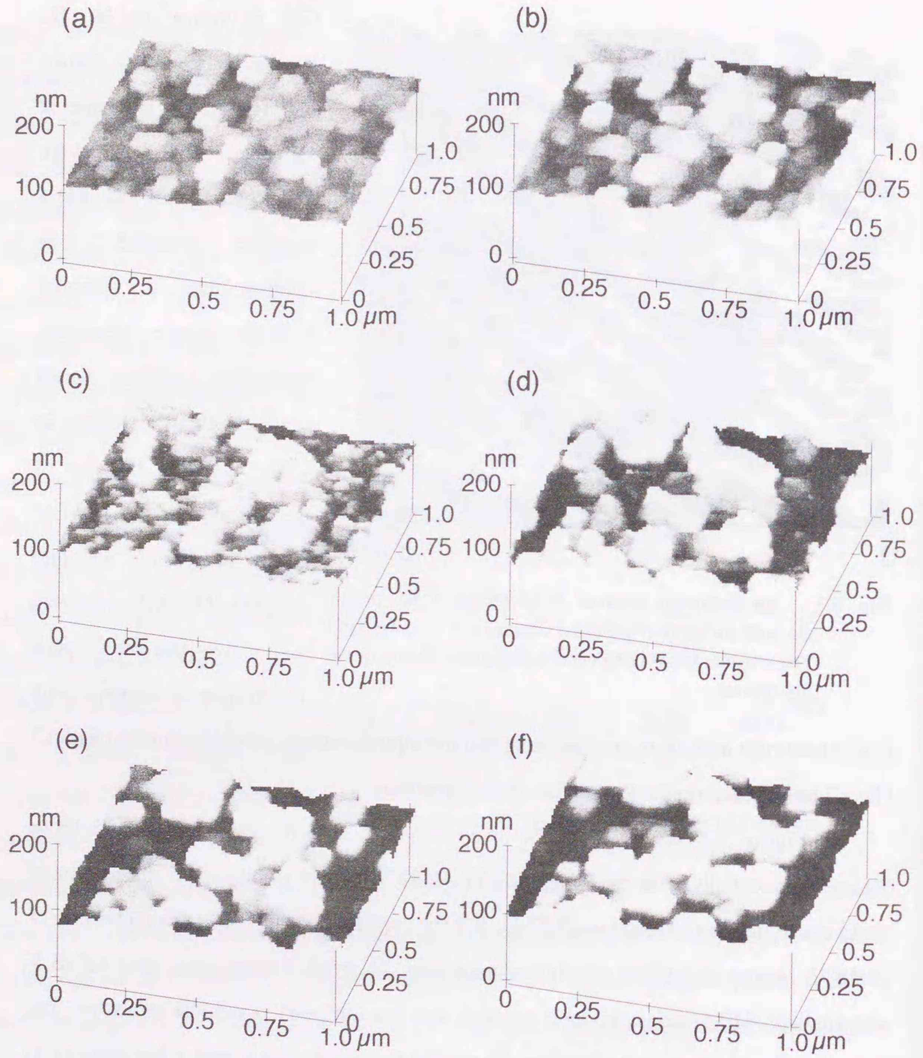

Fig. 5.4 AFM images of p-GaAs in 10 mM HCl obtained (a) at 0 V vs. Ag/AgCl and (b)-(f) after the potential was pulsed from 0 V to +0.18 V where the anodic current of ca. 100 mA·cm^{-2} flowed. Time after the application of +0.18 V was (b) 1 min, (c) 5.5 min, (d) 11 min, (e) 15.5 min, and (f) 22 min.

(100)-(1x1) structure for an *n*-GaAs(100) electrode in HCl solution, although the structure formed on the surface when anodic potential is applied is different from that at *p*-GaAs.

5.2.2 *p*-GaAs(100) in H_2SO_4 solution

Figure 5.5 shows current-potential relation of a *p*-GaAs(100) electrode in 10 mM H_2SO_4 solution during AFM measurement with the potential scan rate of 20 mV/s and showed a usual diode characteristics as expected for semiconductor electrodes. The flat-band potential of *p*-GaAs at this pH is about +0.32 V (vs. Ag/AgCl) [47]. Anodic current started to flow at the potential little negative than the flat-band potential, increased as potential became more positive and became very large at much more positive potential. The cathodic current in the dark was very low within the potential region examined in this study. There were enough holes, the majority carriers, at the semiconductor surface to dissolve the GaAs surface when the potential was more positive than the flat-band potential. On the other hand, the space charge layer, which should be considered as a barrier for the electron transfer, is formed within the semiconductor when the potential becomes more negative than the flat-band potential. Although light, which was used for sensing the deflection of the cantilever, hit the electrode surface and electron-hole pairs were generated, the current-potential curve obtained during AFM measurement was almost identical to that measured in the dark, showing photogenerated electrons recombine with holes before they were transferred to solution species, maybe because the space charge layer was very thin at the semiconductor electrode of high doping density.

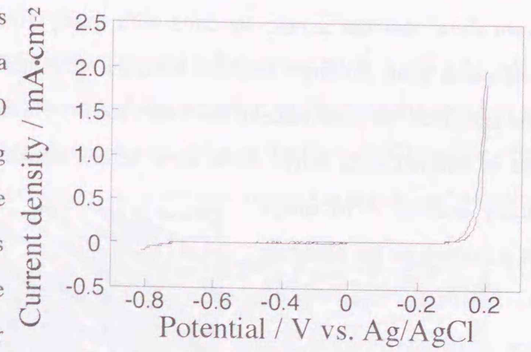

Fig. 5.5 Current-Potential relations of a *p*-GaAs(100) electrode in 10 mM H_2SO_4. Sweep rate; 20 mV / s.

To obtain AFM images under controlled conditions, 10 mM H_2SO_4 solution was introduced to the electrochemical AFM cell while keeping the potential of the GaAs(100) electrode at -0.8 V. Although AFM images obtained just after the solution was introduced showed no ordered structure, atomically ordered images were obtained after keeping the potential at this potential while repeating the AFM scan as shown in Figure 5.6 (a). This AFM image is shown without any filtering. Figure 5.6 (b) shows a two-dimensional (2D)

Fourier spectrum of the raw data shown in Fig. 5.6 (a). The top view and the 2D spectrum show that the atomic structure with nearly four-fold symmetry exists. The topmost atoms show a nearest-neighbor distance of about 0.41 nm ± 0.03 nm, which is in good agreement with the value of the GaAs(100)-(1x1) surface [44]. As-received GaAs surface is covered with native oxide layer with a thickness of a few nanometers and atomically ordered AFM image is not expected to be observed unless the oxide layer on the surface is removed. Thus, the results of Fig. 5.6 show that the surface oxide layer was removed electrochemically. It must be mentioned here, however, that the scanning of the tip seemed to play a certain role for the removal of oxide layer. If we changed the imaging portion after the atomically ordered image was obtained at a certain portion of the surface, the image showed no atomic structure, suggesting the other portion was still covered with oxide. By repeating the scanning at that spot, the atomically ordered image of GaAs(100)-(1x1) was obtained. It does not mean, however, the cathodic potential had no effect as we never observed periodic structure in Milli-Q water even if the tip scan was repeated for long time. Thus, the oxide seemed to be removed by the tip-induced electrochemical reduction. Since scraped structure was not created at the portion where the tip was scanned repeatedly in the cathodic potential region,

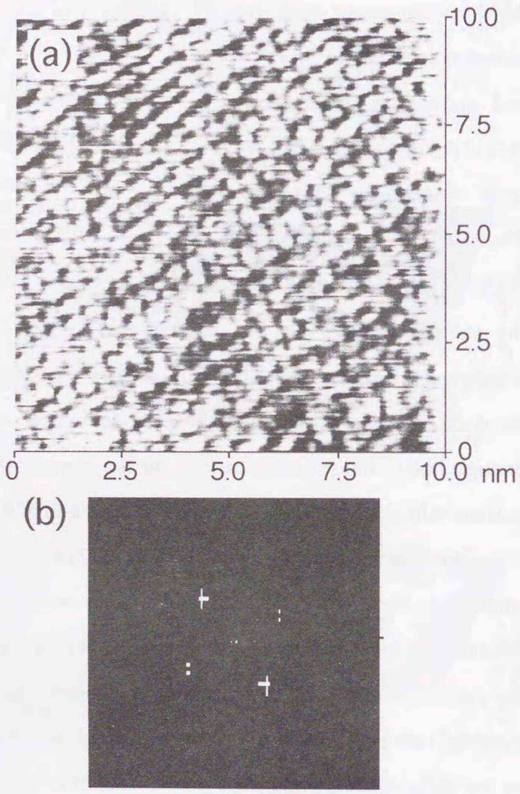

Fig. 5.6 (a) An AFM image (10 nm x 10 nm) of *p*-GaAs(100) structure in 10 mM H_2SO_4 at -0.8 V vs. Ag/AgCl, showing (1x1) structure. (b) Two-dimensional Fourier spectrum of the result of (a).

the scanning of the AFM tip seemed to remove only oxide layer on the surface in the cathodic potential region.

The GaAs(100) surface forms reconstructed structure such as c(2 x 8), (2 x 4), and c(4 x 4) in UHV condition because of the existence of the dangling bond in (1x1) structure [45,46]. However, the present results showed the GaAs(100) surface showed no reconstruction and the stable (1x1) structures were obtained in the electrolyte solution.

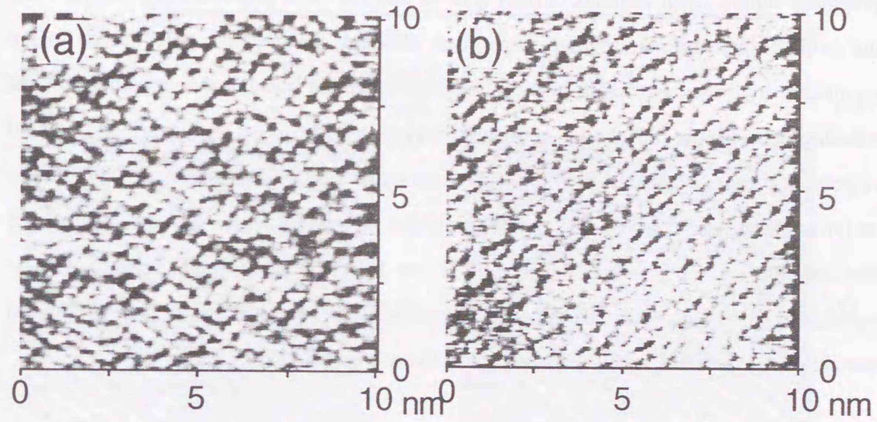

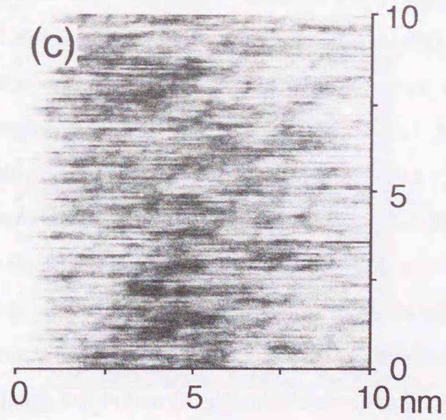

Fig. 5.7 AFM images of potential regions where images were taken are (a) -0.75 V, (b) -0.4 V, and (c) +0.1 V in 10 mM H_2SO_4.

The presence of the stable (1x1) structure is unique in the electrochemical system and suggests that the dangling bonds of the surface atoms are terminated with ions in the electrolyte solution. As we have reported before, *p*-GaAs(100)-(1x1) structure was also found in HCl solution but near the open circuit potential [48]. We proposed that the surface atoms are terminated with Cl in HCl solution. On the other hand, in H_2SO_4 solution reported in this section, the GaAs(100)-(1x1) structure was most stable at the potentials where small cathodic current flowed and the more negative the potential was, the more distinct the atomic image was seen, although too negative potential led to the significant hydrogen evolution and the evolved hydrogen gas interfered with the AFM measurement. Figure 5.7 shows atomically resolved AFM images at the various potential regions of *p*-GaAs in H_2SO_4 solution. It is contrary to the result observed in HCl solution as far as the potential region for atomic resolution imaging is concerned. It is speculated that dangling bonds are terminated with H^+ or H in H_2SO_4 solution in the cathodic potential region, since the anion in the solution is SO_4^{2-}, which is larger than Cl^-, and is not able to form bonds with surface atoms in the anodic potential region.

5.2.3 p-GaAs(100) in Na_2S solution

To clarify the role of the adsorbed atoms on GaAs surface, the surface was treated with S, which is known to stabilize the surface condition. [49,50]. Atomic images of p-GaAs(100) surface were observed in Na_2S solution in the potential region where almost no current flowed, *i.e.*, between the onset potential of hydrogen evolution (-0.7 V) and anodic dissolution (+0.05 V). Figure 5.8 shows (a) a cyclic voltammogram and (b) atomically resolved AFM images at the various potentials of *p*-GaAs(100) electrode in 2 mM Na_2S solution. All the AFM images obtained in Na_2S solution showed identical structure regardless of the electrode potential. The structure showed four-fold symmetry with nearest neighbor distance of about 0.40 nm. The atomic distance and the directions of the atom rows were same as those obtained in 10 mM H_2SO_4 solution at -0.8 V before the solution was replaced by 2 mM Na_2S solution. Thus, it is clear that *p*-GaAs(100) surface has the (1x1) structure in Na_2S solution. Although sulfur atoms which adsorb on GaAs(100) surface when the H_2S gas is introduced in UHV chamber form (2x1) adlayer in UHV condition [51], only the (1x1) structure was observed in Na_2S solution. This

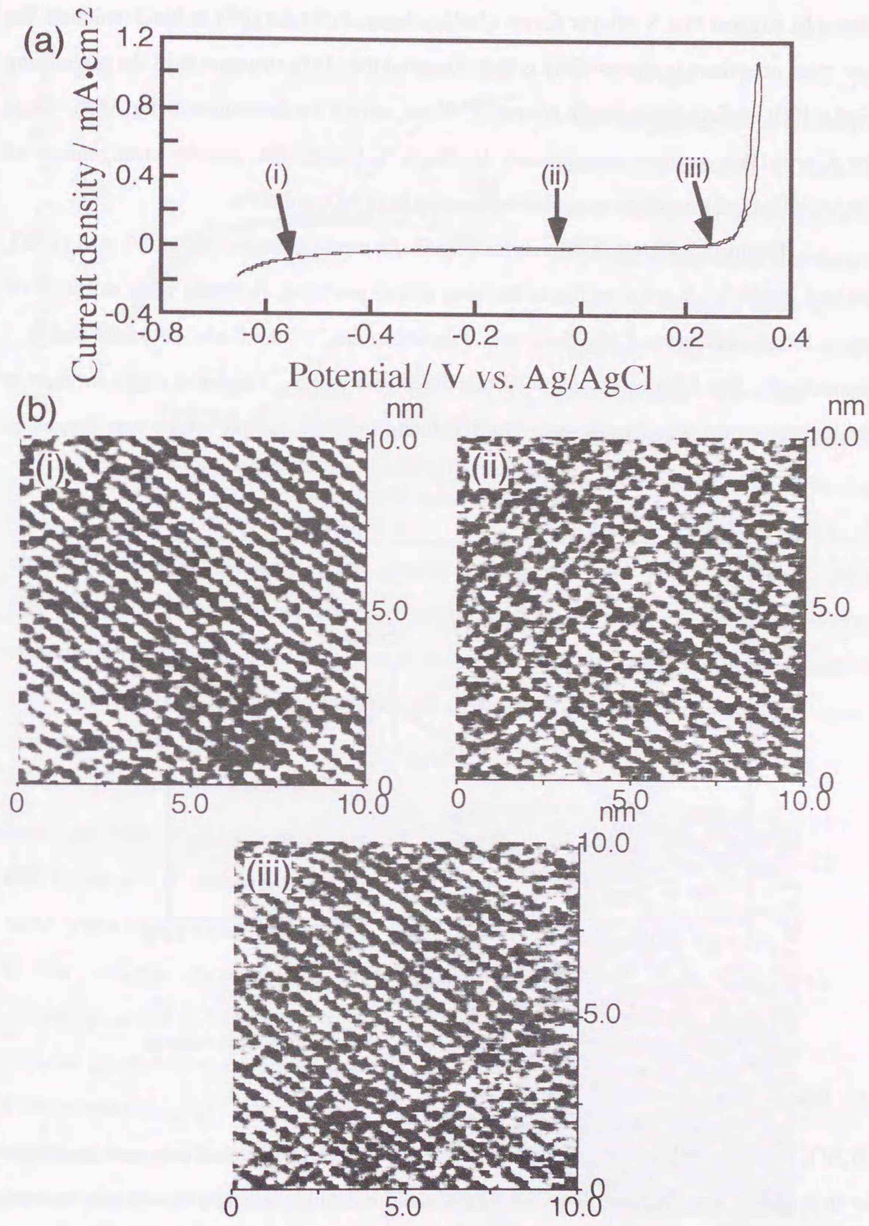

Fig. 5.8 (a) Cyclic voltammogram of *p*-GaAs(100) in 2 mM Na_2S. (b) AFM images of potential regions where images were taken are shown in (a).

seems to suggest that S adlayer forms (1x1) adlayer on GaAs(100) in Na_2S solution but one must note there is a possibility is that observed the (1x1) structure is of the underlying GaAs(100) surface because the observed atoms cannot be determinated by AFM. Once the GaAs(100) surface was treated in Na_2S solution, the atomic arrangement of GaAs(100)-(1x1) structure was observed easily in H_2SO_4 solution.

Figure 5.9 shows XPS spectra of *p*-GaAs electrode immersed in 10 mM H_2SO_4 (a) and 2 mM Na_2S solution (b) at the open circuit potential. A strong peak at 160.5 eV and a broad peak around 164.5 eV are assigned to Ga_{3s} of the GaAs substrate and S_{2p}, respectively. The XPS results showed that the intensity of S_{2p} band was much stronger at the sample which was treated with Na_2S solution than the sample which was dipped in

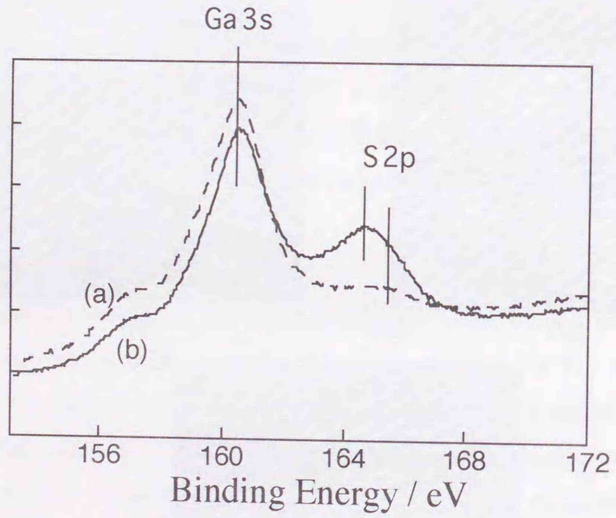

Fig. 5.9 XPS spectra of *p*-GaAs(100) electrode. Samples were immersed in 10 mM H_2SO_4 (a) and 2 mM Na_2S solution.

H_2SO_4 solution. Although this result suggests that GaAs(100) surface was terminated with S atoms, it is necessary to investigate in more detail by using other techniques such as SXRD and EXAFS.

A similar effect of "sulfur treatment" was observed at *n*-GaAs(100) electrodes.

5.2.4 *n*-GaAs(100) in HCl solution

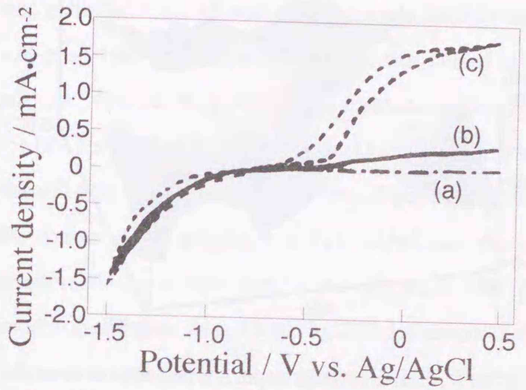

Fig. 5.10 Current-potential relation of *n*-GaAs in 10 mM HCl. (a) in dark, (b) during AFM measurement, and (c) under white light illumination.

Figure 5.10 shows cyclic voltammograms of *n*-GaAs(100) electrode in 10 mM in dark (a), under during AFM measurement (b), and white light illumination by 30 W halogen lamp (c). As expected for the *n*-type semiconductor electrode, large cathodic current was observed but no anodic current flowed in dark and anodic current was strongly enhanced by illumination [1]. The anodic current was also observed during AFM measurement, although small compared with that under white light illumination. This current should be also photocurrent as some portions of laser light which was used for sensing the deflection of the cantilever hit the electrode surface. Cathodic and anodic current should be due to hydrogen evolution and GaAs dissolution, respectively.

Figure 5.11 shows the high resolution AFM image obtained when HCl solution was introduced into the AFM cell while keeping the potential of the *n*-GaAs electrode in the cathodic potential region where small cathodic current flowed. The atomic arrangement with four-fold symmetry and the nearest atomic distance of 0.4 nm was observed. The surface was very flat over a wide region (1 x 1 μm^2) and was stable for a long time if the electrode potential was kept in

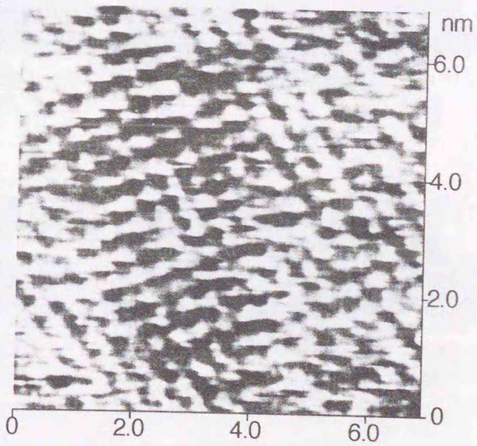

Fig. 5.11 An atomically resolved AFM image of the *p*-GaAs electrode surface in 10 mM HCl obtained at -0.4 V vs. Ag/AgCl.

cathodic potential region.

The surface structure change of *n*-GaAs(100) during electrochemical etching process was followed by ECAFM. In order to examine the electrochemical etching process in detail, AFM measurement was carried out the sample which had a relatively rough structure as shown in Fig. 5.12.

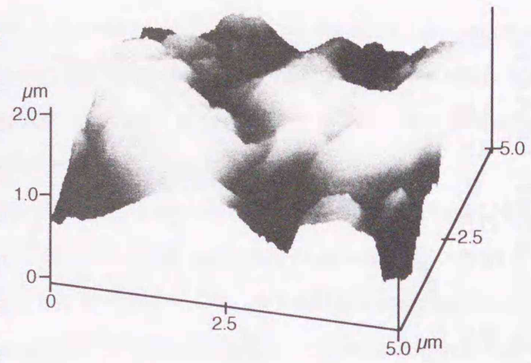

Fig. 5.12 An AFM image (5 μm x 5 μm) of an as-received *p*-GaAs(100) surface without polishing.

Figure 5.13 shows AFM images obtained sequentially after -0.6 V was applied. At this potential almost no current flowed (c.f. open circuit potential = -0.58 V) and no structure change was observed even after 20 min. Similar results were reported by STM in NaOH solution [52].

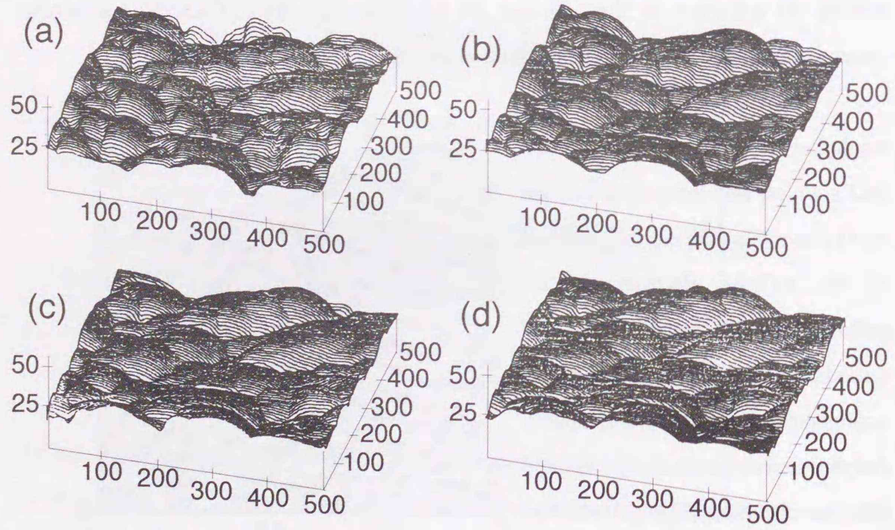

Fig. 5.13 Sequentially obtained AFM images of *n*-GaAs in 10 mM HCl while potential was held at -0.6 V where no anodic current flowed. Time after application of the potential at -0.6 V was (a) 0.5 min, (b) 7 min, (c) 13.5 min, and (d) 20 min.

Figure 5.14 (a) is an AFM image obtained at -0.6 V after the image of Fig. 5.13 was collected, *i.e.*, 35 min after the application of the potential. Still no surface change was observed. As soon as the potential was pulsed to 0 V where anodic current of ca. 150 $mA \cdot cm^{-2}$ flowed, however, surface structure started to change as shown in Figs. 5.14 (b)-(f). The change was significant. Dome structures were removed, the structure became flat and only large structure remained. Since similar structure was observed at places were the contact AFM imaging was not carried out, the effect of the tip on the dissolution reaction of the surface can not be important. Our previous studies on photochemical anodic dissolution of *n*-GaAs by STM showed that electrolyte solutions have strong influence on the surface morphology [13,52]. Photoelectrochemical etching leads to a flat

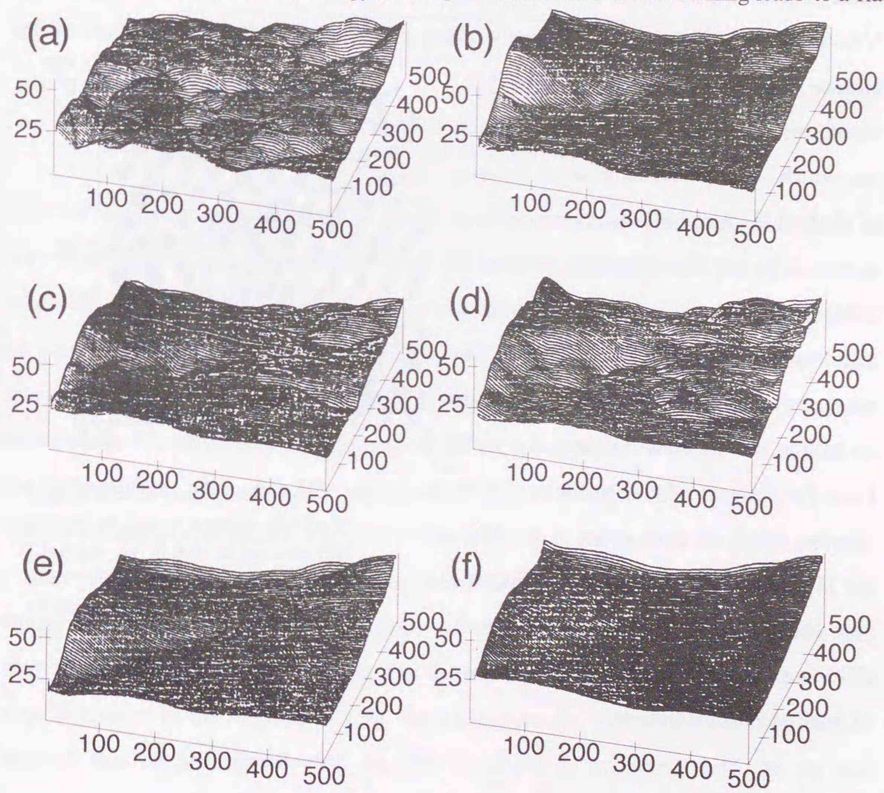

Fig. 5.14 AFM images of *n*-GaAs in 10 mM HCl obtained (a) after the potential was held at -0.6 V for 35 min and (b)-(f) after the potential was pulsed from -0.6 V to 0 V where anodic photocurrent of ca. 150 $\mu A \cdot cm^{-2}$ flowed. Time after the application of 0 V was (b) 3.5 min, (c) 6.5 min, (d) 10 min, (e) 17.5 min, and (f) 25 min.

surface in $HClO_4$ solutions [52], but generated rougher surface in NaOH solution [13]. Preliminary investigation using electrochemical AFM in various electrolyte solutions also suggests the important role of electrolyte solution in determining the morphology of electrochemically etched surface. Detailed investigation is now under way.

Although some portions of the surface became atomically flat after prolonged oxidation (Fig. 5.14 (f)), an atomically resolved structure was not observed at 0 V. An atomically resolved AFM image was, however, obtained if potential was pulsed to -0.6 V where no current flowed. Structure became clear with time and several minutes after -0.6 V was applied an atomically resolved AFM image as shown in Fig. 5.15, was obtained at some portion of the surface. The reason why atomic image was obtained at -0.6 V not at 0 V is that dissolution process is actively taking place at 0 V and/or the oxide covers the surface [53]. This image suggests the (111) arrangement with atom-atom distance of 0.4 nm which agrees with atom-atom distance of GaAs(111) face [44]. It is reasonable as it was reported that chemical etching of (001) face of GaAs in HCl solution selectively gives (111) face [42,43]. One must, however, note that 0.4 nm atomic separation can be observed also at a (100) face. The difference between the two is the crossing angle of atom rows, i. e., 60° for (111) and 90° for (100). Thus, the possibility that the imaged surface is (100)face cannot be totally rejected because of relatively unclear image.

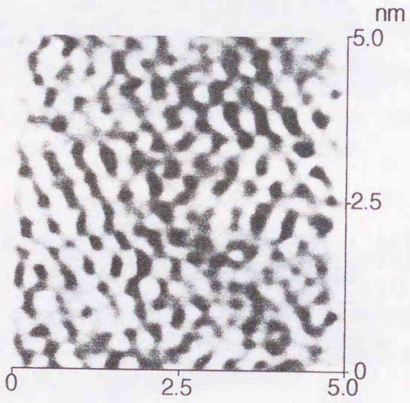

Fig. 5.15 An atomically resolved AFM imaged of *n*-GaAs electrode surface in 10 mM HCl obtained at -0.6 V vs. Ag/AgCl after potential was held at 0 V for 25 min (Fig. 5.14 (f)). The structure shows (111) arrangement. The image was FFT filtered.

5.2.5 Surface Modification

Figure 5.16 shows an AFM image of *p*-GaAs(100) surface (1000 x 1000 nm^2) observed with an applied force of less than 1 nN in 10 mM H_2SO_4 solution at an open circuit potential (-0.05 V) where no current flowed apparently, captured after the 100 x

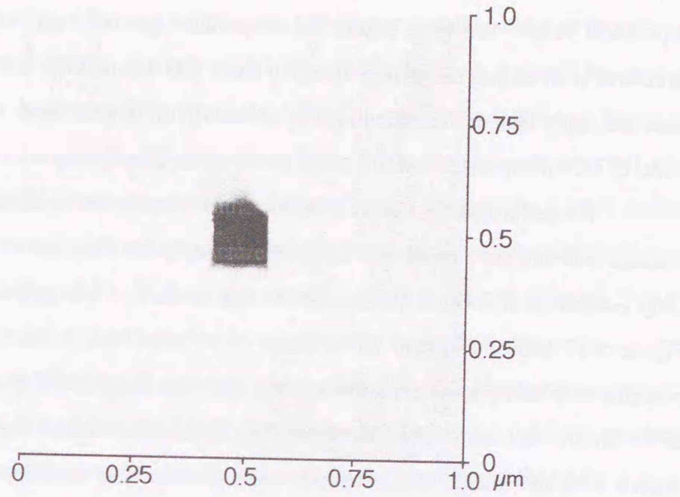

Fig. 5.16 AFM top image (1000 x 1000 nm2) of *p*-GaAs surface in 10 mM H_2SO_4 solution at the open circuit potential (-0.05 V vs. Ag/AgCl) after small scan (100 x 100 nm2) imaging for 1 hour at the same potential but with the stronger force. See text for detail.

100 nm^2 area in the center of the GaAs surface was scanned with an applied force of about 10 nN for 1 hour. It is clear that there is a square hollow at central part of the image where the tip was initially scanned with strong force. During the initial scan, the number of scans of the tip was 450 as it took 8 s to obtained one image (25 lines/s x 200 lines/image). When the GaAs electrode was kept in H_2SO_4 solution near the open circuit potential for 1 hour without the scanning of the tip, no apparent structure was created on the GaAs surface, although a little uneven structure was formed. Thus, one can conclude that the surface modification is the result of the scanning of the tip over the GaAs surface.

Although the scanning size was only 100 x 100 nm^2, the observed size of the square hollow was 140 x 140 nm^2. At least two reasons should be considered for the size of modified square hollow to be larger than the scan size. One is that AFM tips have finite size. If a shape of the AFM tip is very sharp like a needle, the modified area should be same as that of the scanned area. Another possibility is a thermal drift. As the real structure for the point of the tip used in the present study has cone angle of 70° and the depth of the square hollow was 28 nm, the expected modification size should be large than the scanned size by 32 nm (= 2 x 28 x sin 35°) which is in good agreement with the

experiment result. We were successful to produce geometrically well-defined square structures with critical dimensions ranging from 100 nm to 3000 nm and the observed sizes are larger than the modified area by about 40 nm in most case, suggesting that the effect of the tip dimension was the major cause of the discrepancy.

We performed the surface modification at various electrode potentials in order to examine whether the surface was modified by the tip mechanically or electrochemically. Only x-direction of 500 nm was scanned so that the surface was modified in a short time. Figure 5.17 shows a typical AFM image of *p*-GaAs(100) surface at an open circuit potential after the tip was scanned at an open circuit potential for 30 min with the scan rate of 25 lines/s. Sectional views corresponding to the solid line in Fig. 5.17 (a) are also shown with the image. The sectional views indicate that modified line has a wedge

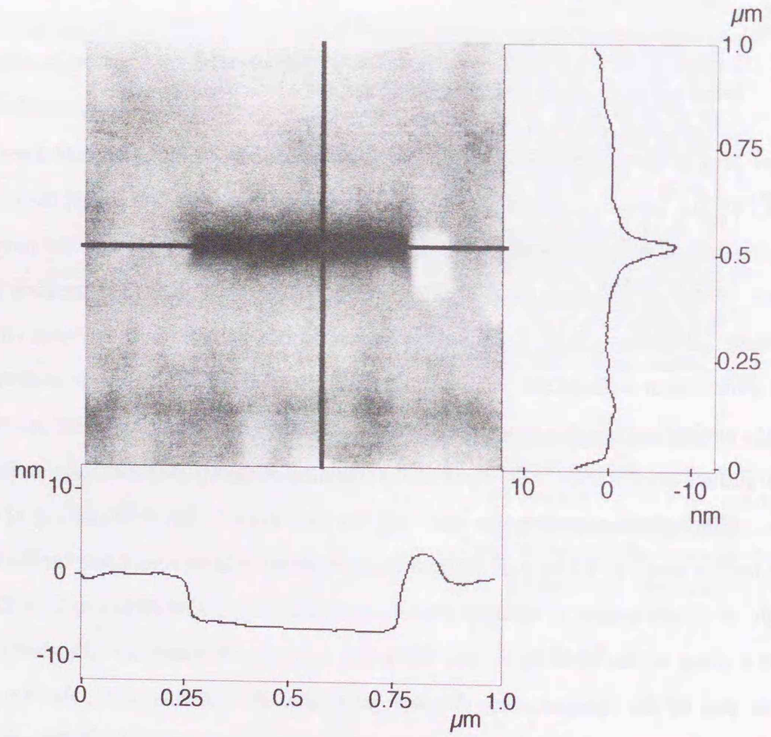

Fig. 5.17 AFM image (1000 x 1000 nm2) of *p*-GaAs surface in 10 mM H_2SO_4 at the open circuit potential after only x-direction was scanned for 30 min with stronger force. Sectional views corresponding to thick solid lines in the image are also shown.

structure with a length of 530 nm which is again little larger than the scan size because of the reason mentioned before, a width of 80 nm, and a depth of 8 nm. This wedge structure resembles the shape of the top of the AFM tip, confirming that the surface was modified by the scanning of the tip over the surface. When the electrode potential was kept at +0.05 V which is more positive than the open circuit potential by 0.10 V during the modification process and imaging process, the depth of the wedge structure was deeper than that of Fig. 5.17. In this case, anodic current of ca. 15 $\mu A \cdot cm^{-2}$ flowed continuously. While the surface was very flat except for the portion where the tip was scanned repeatedly and the wedge structure was created in Fig. 5.16, uneven structures were seen at the portion where the AFM tip was not scanned when the potential was kept at +0.05 V. Surface structure was not affected at all by the scanning of the tip for 1 hour when the electrode was kept at negative potential (-0.5 V). It may be worth pointing out here that we obtained GaAs(100)-(1x1) structure when the potential was kept cathodic for long time, showing only the surface oxide layer was completely removed by cathodic reduction.

The potential dependence of the depth of fabricated wedge and steady current at *p*-GaAs electrode is shown in Fig. 5.18. The more positive the potential, the larger the anodic current and the deeper the depth of the wedge structure. However, when the electrode potential became more positive than +0.075 V, the wedge structure was not clearly observed because the dissolution process on *p*-GaAs surface proceeded violently and large hill-and-valley structures were formed everywhere on the surface. These results suggest that the formation of square hollow or wedge structure on the surface was performed neither by the scanning of the tip alone nor by the anodic

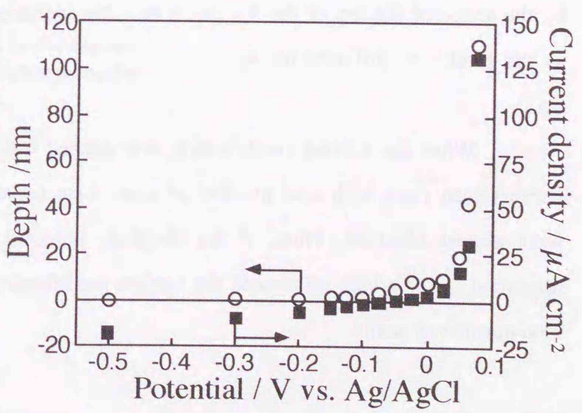

Fig. 5.18 The mean depth and the steady current as a function of the electrode potential for *p*-GaAs electrode in 10 mM H_2SO_4 solution.

potential alone. The modification is the result of the tip-induced electrochemical etching. The results of Fig. 5.15 and Fig. 5.16(a) show that even at the open circuit potential, GaAs dissolution process occurred. This is because small anodic current corresponding to GaAs dissolution flowed to compensate the cathodic photocurrent which was generated by laser light used for sensing the deflection of the cantilever. Most of the anodic current seemed to be consumed at the portion over which the tip was scanned.

Figure 5.19 shows the relationship between the number of scans and the depth of modified wedge with an applied force of 10 nN, a scan width of 500 nm, and scan rate of 25 line/s. All the measurements were carried out in 10 mM H_2SO_4 solution at an open circuit potential. The mean depth increased gradually with increasing the number of scans up to 90000 times and seemed to saturate with the number of scans. The AFM tip was an obstacle to modify the surface by itself when the modification structure became too deep and, consequently, surface modification stopped. The limit of the depth for modified structure seemed to be influenced by the shape of the top of the tip as the limit was different tip by tip.

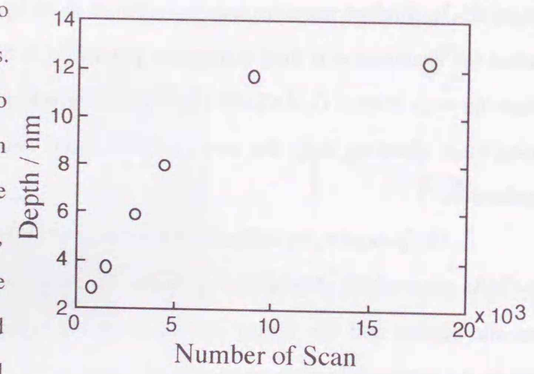

Fig. 5.19 The mean depth of the modified wedge created at the open circuit potential on the *p*-GaAs surface as a function of the number of scans in 10 mM H_2SO_4.

When the surface modification was carried out at the open circuit potential at various scan rates with total number of scans kept constant, the depths of the wedges were almost identical. Thus, if the electrode potential was kept constant, the most important factor which influenced the surface modification was not the scan rate but the total number of scans.

5.3 Conclusion

The surface of GaAs(100) electrode was examined by *in situ* AFM measurements under potential control. Atomic arrangement of (100)-(1x1) structure was

observed at both *n*-type and *p*-type GaAs(100) electrode in various electrolyte solutions. The atomic AFM images were observed clearly in HCl solution when the electrode was kept around the open circuit potential. On the other hand, in the case of H_2SO_4 solution, GaAs(100)-(1x1) structure was most stable at the potentials little positive than that of H_2 evolution. These results suggest that dangling bonds are terminated with Cl^- in HCl solution at the anodic potential region and with H^+ in H_2SO_4 solution at the cathodic potential region. In Na_2S solution, atomic image of GaAs(100) surface was obtained over a wide potential region. Anodic dissolution process of GaAs(100) surface was different between *n*-type and *p*-type electrode.

The AFM tip induced surface modification of the GaAs electrode surface was also studied by *in situ* AFM measurements under potential control. The electrochemical dissolution was found to be promoted by the scanning of an AFM tip.

References

1) S. R. Morrison, Electrochemistry at Semiconductor and Oxidized Electrode, Plenum Press, New York (1980).
2) H. Gerischer, *J. Electroanal. Chem.* **58**, 263 (1975).
3) K.W. Frese, Jr., M. J. Madou and S. R. Morrison, *J. Electrochem. Soc.* **128**, 1527 (1981).
4) P. Allongue and H. Cachet, *Electrochim. Acta.* **33**, 9 (1988).
5) W. J. Plieth, G. Pfuhl, A. Felske, and W. Badawy, *Electrochim. Acta.* **34**, 1133 (1989).
6) H. F. Hsieh and H. C. Shih, *J. Electrochem. Soc.* **138**, 1965 (1991).
7) K. Uosaki, Y. Shigematsu, S. Kaneko, and H. Kita, *J. Phys. Chem.* **93**, 6521 (1989).
8) K. Uosaki, Y. Shigematsu, H. Kita, and K. Kunimatsu, *J. Phys. Chem.* **94**, 4623 (1990).
9) K. Itaya and E. Tomita, *Surf. Sci.* **201**, L507 (1988).
10) S.-L. Yau, X. Gao, S.-C. Chang, B.C. Schardt, and M.J. Weaver, *J. Am. Chem. Soc.* **113**, 6049 (1991).
11) O. M. Magnussen, J. Hageböck, J. Holtos, and R.J. Behm, *Faraday discuss.* **94**, 329 (1992).
12) S. R. Snyder and H. S. White, *Anal. Chem.* **64**, 166R (1992).
13) K. Uosaki, M. Fukuda, and H. Kita, *Denki Kagaku* **57** (1989) 1213.
14) S. Erikson, P. Carlsson, B. Holmström, and K. Uosaki, *J. Electroanal. Chem.* **313**, 121 (1991).
15) P. Carlsson, B. Holmström, H. Kita, and K. Uosaki, *Surf. Sci.* **237**, 280 (1980).
16) K. Itaya, R. Sugawara, Y. Morita, and H. Tokumoto, *Appl. Phys. Lett.* **60**, 2534 (1992).
17) S.-L. Yau, F.F. Fun, and A.J. Bard, *J.Electrochem. Soc.* **139**, 2825 (1992).
18) P. Allongue, H. Brune, and H. Gerischer, *Surf. Sci.* **257**, 414. (1992)
19) S. Manne, P. K. Hansma, J. Massie, V. B. Elings, and A. A. Gewirth, *Science* **251** (1991) 183.
20) C.-h. Chen, S. M. Vescky, and A. A. Gewirth, *J. Am. Chem. Soc.* **114**, 451 (1992).
21) C.-h. Chen and A. A. Gewirth, *Phys. Rev. Lett.* **68**, 1571 (1992).
22) K. Uosaki and M. Koinuma, *J. Electroanal. Chem.* **357**, 301 (1993).
23) L. F. Chi, L. M. Eng, K. Graf, and H. Fuchs, *Langmuir* **8**, 2255 (1992).
24) U. Demir, K. K. Balasubramanian, V. Cammarata, and C. Shannon, *J. Vac. Sci. Technol. B* **13**, 1294 (1995).
25) C. B. Ross, L. Sun, and R. M. Crooks, *Langmuir* **9**, 632 (1993).
26) T. Nakagawa, K. Ogawa, and T. Kurumizawa, *Lungmuir* **10**, 525 (1994).
27) J. A. Dagata, J. Schneir, H. H. Harary, C. J. Evans, M. T. Postek, and J. Bennett, *Appl. Phys. Lett.* **56**, 2001 (1990).
28) E. S. Snow, P. M. Campbell, and P. J. McMarr, *Appl. Phys. Lett.* **63**, 749 (1993).
29) T. K. Whidden, J. Allgair, A. Jenkins-Gray, and M. N. Kozicki, *J. Vac. Sci. Technol. B* **13**, 1337 (1995).
30) G. L. Christenson, S. A. Miller, Z. H. Zhu, N. C. MacDonald, and Y. H. Lo, *Appl. Phys. Lett.* **66**, 2780 (1995).
31) T. Sugimoto, T. Endo, K. Kuwahara, R. Kaneko, and T. Miyamoto, *J. Vac. Sci. Tecnol. B* **12**, 1876 (1994).
32) H. Sugimura, T. Uchida, N. Kitamura, H. Masuhara, *J. Phys. Chem.* **98**, 4352 (1994).
33) H. Göbel and P. von Blanckenhagen, *J. Vac. Sci. Technol. B* **13**, 1247 (1995).
34) Y. Kim, J. Huang, and C. M. Lieber, *Appl. Phys. Lett.* **59**, 3404 (1991).
35) E. Delawski and B. A. Parkinson, *J. Am. Chem. Soc.* **114**, 1661 (1992).
36) K. Uosaki and M. Koinuma, *J. Appl. Phys.* **74**, 1675 (1993).
37) W. T. Müller, D. L. Klein, T. Lee, J. Clarke, P. L. McEuen, P. G. Schultz, *Science* **268**, 272 (1995).

38) A. K. Vijh, in *Electrochemistry of Metal and Semiconductors*, Marcel Dekker, New York (1973).
39) R. E. White, J. O'M. Bockris, and B. E. Conway, in *Modern Aspects of Electrochemistry*, Plenum, New York (1986).
40) J. R. Lagraff and A. A. Gewirth, *Surf. Sci.* **326**, L461 (1995).
41) J. R. Lagraff and A. A. Gewirth, *J. Phys. Chem.* **99**, 10009 (1995).
42) P.K. Kohl, C. Wolowodiuk and F.W. Ostermayer, Jr., *J. Electrochem. Soc.* **130** (1983) 2288.
43) S. Adachi and K. Oe, *J. Electrochem. Soc.* **130**, 2427 (1983).
44) J. S. Blakemore, *J. Appl. Phys.* **53**, R123 (1982).
45) D. K. Biegelesen, R. D. Bringans, J. E. Northrup, and L. E. Swartz, *Phys. Rev. B* **41**, 5701 (1990).
46) J. E. Northrup and S. Froyen, *Phys. Rev. Lett.* **71**, 2276 (1993).
47) J. J. Kelly and R. Memming, *J. Electrochem. Soc.* **129**, 729 (1982).
48) M. Koinuma and K. Uosaki, *Surf. Sci.* **311**, L737 (1994).
49) J. F. Fan, H. Oigawa, and Y. Nannichi, *Jpn. J. Appl. Phys.* **27**, L1331 (1988).
50) B. J. Skromme, C. J. Sandroff, E. Yablonoitch, and T. Gmitter, *Appl. Phys. Lett.* **51**, 2022 (1988).
51) W. Mönch and H. Gant, *J. Vac. Sci. Technol.* **17**, 1094 (1980).
52) S. Erikson, P. Carlsson, B. Holmström, and K. Uosaki, J. Electroanal. Chem. **313**, 121 (1991).
53) H. F. Hsieh and H. C. Shih, J. Electrochem. Soc. **138**, 1965 (1991).

CHAPTER 6

COPPER ELECTROCHEMICAL DEPOSITION ON GaAs(100) SURFACE - AN ECAFM STUDY

CHAPTER 6
COPPER ELECTROCHEMICAL DEPOSITION ON GaAs(100) SURFACE - AN ECAFM STUDY

6.1 Introduction

The electrodeposition of metal is a process of great technological importance. A large number of studies have been carried out to understand the mechanism of electrodeposition of metal on conducting surfaces by employing a variety of electrochemical and spectroscopic techniques [1-3]. Traditionally, conventional electrochemical methods, such as cyclic voltammetry and impedance spectroscopy, have been used to assess the mechanism and kinetics of the metal electrocrystallization. Such techniques, however, only provide information concerning the whole surface. To fully understand the process, it is essential to obtain structural information on the substrate and the deposit in μm to the atomic level. Although techniques such as electron microscopy and optical microscopy have been applied to examine the morphology of the substrate and the metal deposit, electron microscopy can be used only for the *ex situ* examination and optical microscopy has poor resolution [4,5]. The scanning tunneling microscope (STM) and its various related techniques, *e.g.*, the atomic force microscope (AFM), are now recognized as very valuable tools for the *in situ* examination of the surface topography of an electrode with extremely high spatial resolution up to the atomic level [6-16]. Many studies have been directed towards *in situ* STM and AFM imaging of metal underdeposition [8-14] and bulk deposition [15-20] on metal electrode.

As pointed out by Allongue *et al.* [21], very little fundamental experimental and theoretical work has been done on the electrodeposition of metal on semiconductor surfaces despite its technical significance [22-24]. Moreover, while metal/electrolyte interfaces have been studied by STM and AFM, only few reports are available for the application of these techniques to semiconductor/electrolyte interfaces [25-38]. We have applied STM to monitor the surface structure change of *n*-GaAs during anodic photocorrosion [27,28] and metal electrodeposition [29]. Unfortunately, however, since STM can only be applied to observe conductive surfaces, the existence of anodic oxide

films as well as the space charge layer in the depletion condition makes the STM measurement of semiconductor electrodes relatively difficult [30]. Atomic images of the semiconductor surface in contact with the electrolyte have been reported only for H-terminated Si in H_2SO_4 [31], HF [32], and NaOH solutions [33,34]. As AFM can image even non-conducing surfaces and electrochemical processes on the tip, which may cause serious problems in the STM measurements in electrolyte solutions, can be avoided in the AFM measurements, AFM may be more useful than STM in studying the electrode surface *in situ*. Gewirth *et al.* demonstrated that electrochemical AFM provides atomic resolution and is a useful technique for the observation of electrode surfaces *in situ* [12,13]. We have successfully applied AFM to monitor the surface structure changes of semiconducting InSe electrode during electrochemical potential cycling [35] and of GaAs during electrochemical etching [36,37] with atomic resolution as described in previous chapter. Recently Gewirth *et al.* also reported *in situ*, atomic resolution images of Ge electrode surfaces under potential control using AFM [38].

In this chapter, ECAFM was employed to investigate the electrodeposition of Cu on *p*-GaAs(100) face in electrolyte solutions. We noticed that how the Cu deposition proceeded strongly depended on the surface structure before the deposition and on the applied overpotential. How the surface modification influenced on Cu electrodeposition process on GaAs surface was also investigated.

6.2 Results and Discussion

6.2.1 *p*-GaAs(100) in HCl-$CuCl_2$ solution

Figure 6.1 shows cyclic voltammograms (CVs) of a *p*-GaAs(100) electrode in 9 mM HCl solution (a) and in 9 mM HCl + 1 mM $CuCl_2$ solution (b) during AFM measurement. The flat-band potential of *p*-GaAs at this pH is about +0.22 V (vs. Ag/AgCl) [39]. In the HCl solution, while an anodic current was observed at potentials more positive than +0.15 V, a cathodic current was hardly seen in the potential region shown in Fig. 6.1 (a) (solid line) as expected for a *p*-type semiconductor. The anodic current corresponds to the electrochemical dissolution of GaAs surface [40,41]. When $CuCl_2$ was added to the solution, the cathodic current was observed at potentials more

negative than -0.1 V and two anodic current peaks were observed at +0.01 V and +0.09 V (Fig. 6.1 (b), dotted line). The cathodic current is associated with Cu electrodeposition onto the GaAs surface and the anodic peaks correspond to the oxidative dissolution of the Cu deposit.

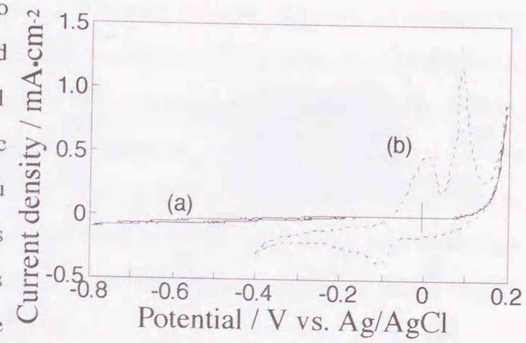

Fig. 6.1 Cyclic Voltammograms of *p*-GaAs(100) in (a) 9 mM HCl solution (solid line) and (b) 9 mM HCl + 1 mM $CuCl_2$ (dotted line) under AFM measurement.

We noticed that the Cu deposition proceeded strongly depended on the surface structure before the deposition. Typical examples are shown in Fig. 6.2 and Fig. 6.3. It took 8 s to capture each image in these cases. The directions of y-scan are indicated by arrows beside the AFM images. Figure 6.2 shows a series of AFM images taken before (a) and during (b)-(f) bulk deposition of Cu on a relatively flat surface of *p*-GaAs(100) in 9 mM HCl + 1 mM $CuCl_2$ solution. Figure 6.2 (a) was recorded at +0.1 V where no Cu deposition took place and showed that the substrate surface was relatively smooth in this region before Cu deposition. Potential was stepped from +0.1 V to -0.15 V during imaging Fig. 6.2 (b) at the time indicated by a thick arrow. Figure 6.2 (b) clearly shows that immediately after potential was stepped into the bulk deposition region at -0.15 V, a large number of small grains were generated with spacings of several tens of nm. These initial deposits of Cu on the surface played a role as effective nucleation centers and the initial growth of these grains seemed to be three-dimensional. AFM images were continuously captured at -0.15 V and are shown in Figs. 6.2 (c), (d), and (e). As time progressed the grains of Cu overlapped with each other (Figs. 6.2 (c) and (d)) and finally truncated pyramidal structures of relatively uniform size were formed (Fig. 6.2 (e)). We must mention here that we had observed atomic arrangement on the terrace portion of the truncated pyramids [42]. While capturing the AFM image shown in Fig. 6.2 (f), potential was pulsed back to +0.1 V as indicated by a thick arrow in the figure. Upon stepping the potential back to +0.1 V, Cu deposits were removed

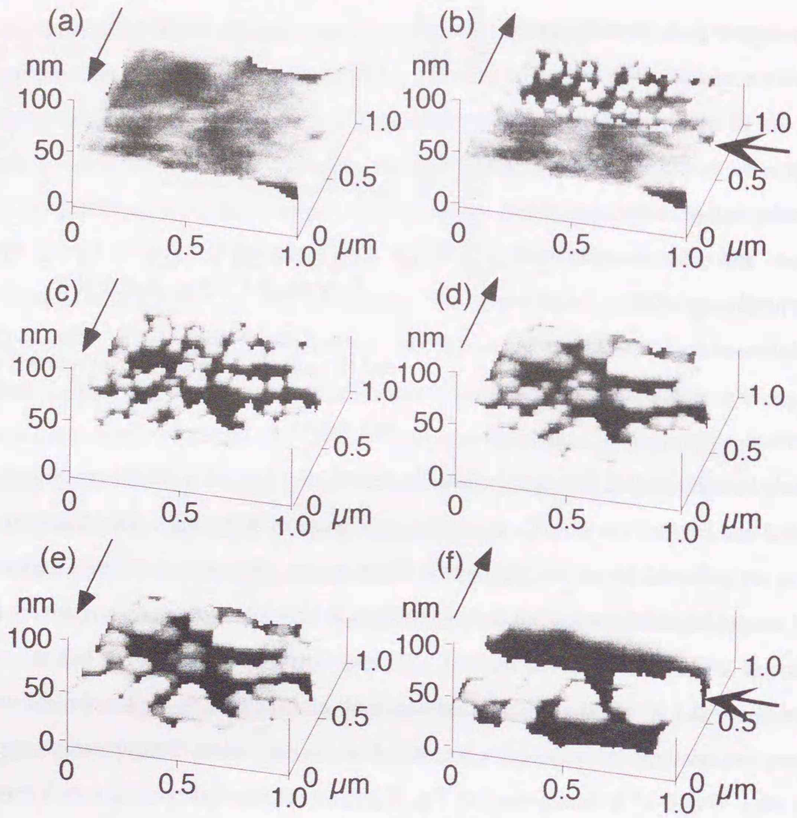

Fig. 6.2 Sequentially obtained AFM images of *p*-GaAs in the relatively flat region in 9 mM HCl + 1 mM $CuCl_2$ solution (a) at +0.1 V vs. Ag/AgCl, (b) while the potential was pulsed to -0.15 V, (c)-(e) at -0.15 V, and (f) while the potential was back to the initial potential (+0.1 V). Time after the application of -0.15 V at the beginning of imaging was (c) 4 s, (d) 12 s, (e) 20 s, and (f) 74 s. Thick arrows indicate the onset of deposition and stripping. Arrows beside the figure indicate the scan direction of the tip.

immediately within the time domain of AFM measurement and the surface was returned to a state similar to that before Cu deposition (Fig. 6.2 (f)).

As mentioned in previous chapter [37], when potentials more positive than 0 V were applied to the GaAs electrode in HCl solution, truncated pyramidal structures were formed on the substrate surface as a result of the anodic electrochemical dissolution of GaAs. Actually, it was hard to obtain an atomically flat surface over a wide range if the electrode was kept in the anodic potential region where no Cu deposition took place. The

surface shown in Fig. 6.2 (a) was one of the flattest surfaces observed. To examine the effect of the surface structure on Cu deposition, we also monitored the deposition process of Cu on the surface with the pre-formed truncated pyramids of relatively uniform size, *i.e.*, 100-200 nm wide and less than 10 nm high as shown in Fig. 6.3 (a). Totally different time sequences were observed for the electrodeposition of Cu on this surface as shown in Figs. 6.3 (b) - (e). As soon as stepping the potential to the bulk deposition region (-0.15 V) as indicated by a thick arrow, the truncated pyramids on the surface

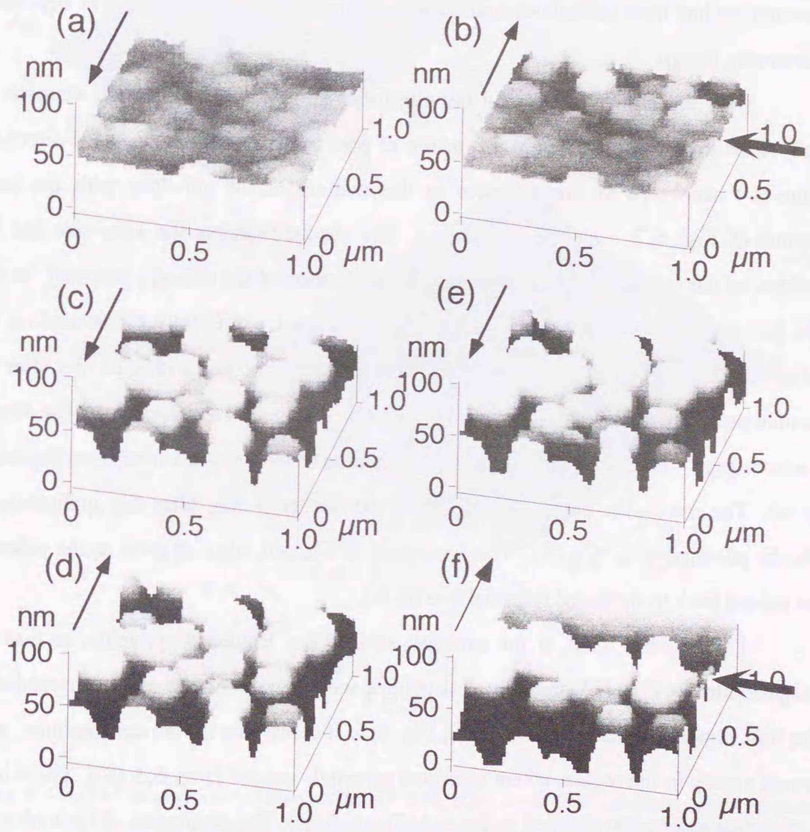

Fig. 6.3 Sequentially obtained AFM images of *p*-GaAs surface with pre-formed truncated pyramidal structures in 9 mM HCl + 1 mM $CuCl_2$ solution (a) at +0.1 V vs. Ag/AgCl, (b) while the potential was pulsed to -0.15 V, (c)-(e) at -0.15 V, and (f) while the potential was back to the initial potential (+0.1 V). Time after the application of -0.15 V at the beginning of imaging was (c) 36 s, (d) 116 s, (e) 196 s, and (f) 204 s. Thick arrows indicate the onset of deposition and stripping. Arrows beside the figure indicate the scan direction of the tip.

grew only in the z-direction (Fig. 6.3 (b)). Grains observed in Fig. 6.2 were not seen in this image. Even the images taken at later times showed that only the height of the truncated pyramids increased with the progress of deposition and the horizontal size was kept almost constant as that of the substrate structure. The truncated pyramids were observed everywhere on the surface regardless of the pre-history of the surface, *i.e.*, whether the surface was continuously scanned or not during Cu deposition. It seems that the heights of the truncated pyramids were slightly lower in the region where AFM measurement had been carried out continuously, indicating that the growth was depressed by scanning the tip.

With the aim of examining the electrodeposition of individual Cu deposits in detail, AFM images were taken as a function of time by scanning only in the x-direction. Figure 6.4 shows AFM images taken in this manner of the substrate with the same structure of Fig. 6.2, *i.e.*, the flat surface. The abscissa depicts the scan size and the numbers on the ordinate indicate time after the application of the cathodic potential. In this case, just after potential was pulsed to -0.15 V, ca. ten Cu clusters were created on the surface 1000 nm in width (Fig. 6.4 (b)). These clusters vanished within ca. 3 s after the potential pulse and terrace structures with a width of 100~200 nm appeared. The terrace structures grew vertically with time, although the rate of the growth varied from deposit to deposit. The maximum height became about 50 nm for 1 min after the application of cathodic potential (Fig. 6.4 (a)). The desorption of Cu took place as soon as the potential was pulsed back to the initial potential (+0.05 V).

On the other hand, if the substrate surface had truncated pyramids, as was the case presented in Fig. 6.3, the terrace structures were formed on the surface immediately after bulk deposition started as shown in Fig. 6.5. It seems that the terrace structures were formed mainly in the region where truncated pyramids existed (Fig. 6.5 (b)). The widths of the structures hardly changed to the end (Fig. 6.5 (a)). The desorption of Cu took place as soon as potential was pulsed back to the initial potential (+0.05 V). The structure of the substrate was, however, not completely recovered and a small amount of Cu deposits seemed to remain on the surface. When the potential was stepped to -0.15 V again, deposition took place at the location where the deposition took place at the first potential pulse.

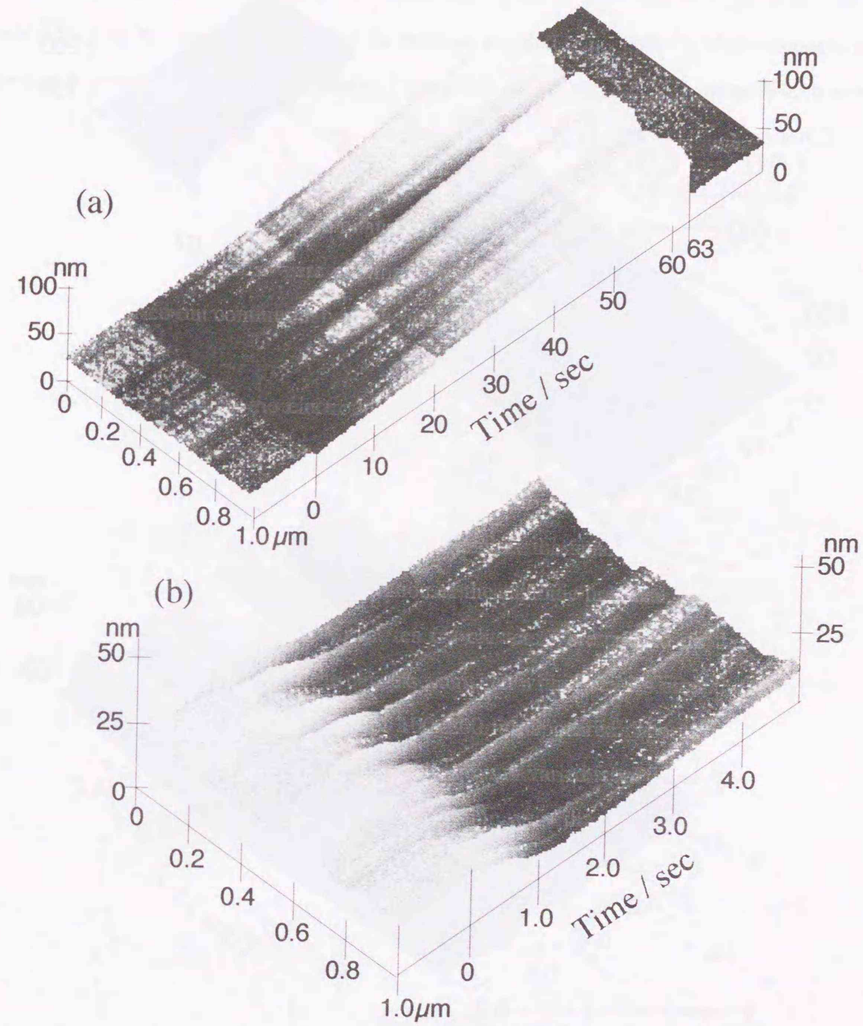

Fig. 6.4 AFM image of a flat *p*-GaAs surface in 9 mM HCl + 1 mM $CuCl_2$ solution showing the time sequence of Cu deposition for deposition time of 67 s (a). Only x-scan was activated. (b) Time expanded view just before and after the deposition. Potential was pulsed from +0.05 V to -0.15 V at 0 s and back at 67 s.

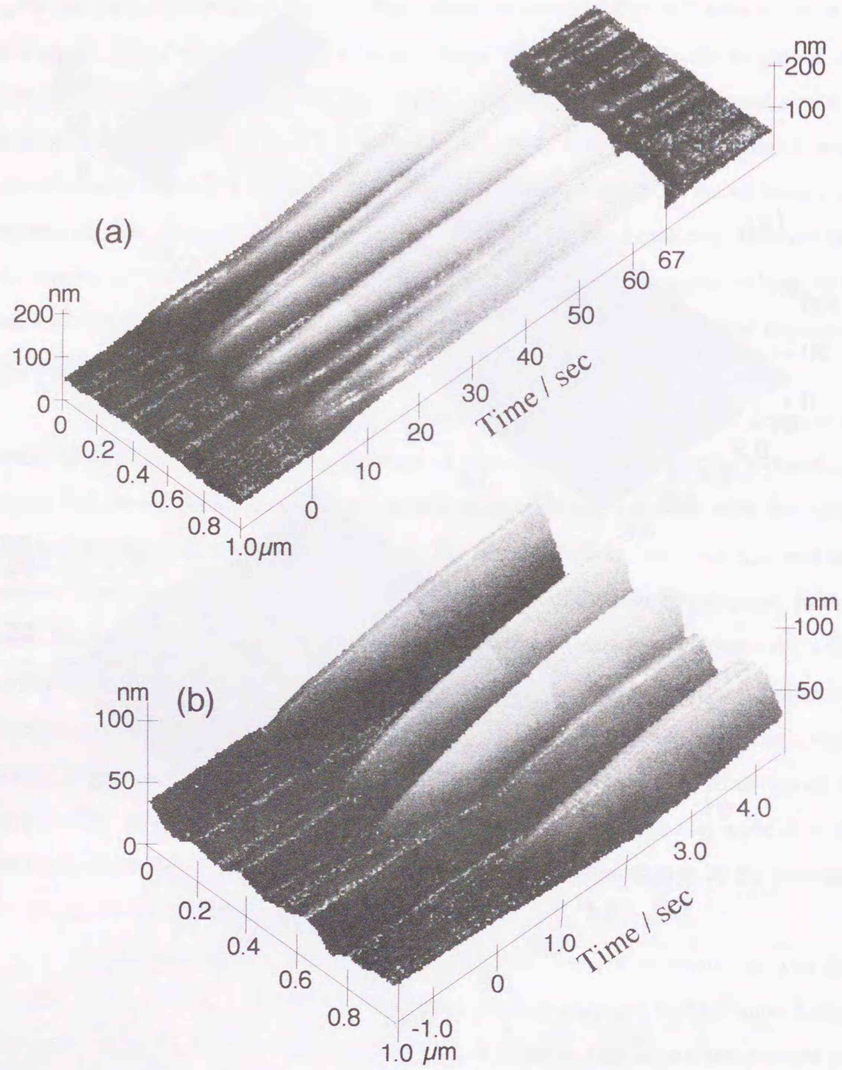

Fig. 6.5 AFM image of *p*-GaAs surface with the pre-formed truncated pyramids in 9 mM HCl + 1 mM $CuCl_2$ solution showing the time sequence of Cu deposition for deposition time of 67 s (a). Only x-scan was activated. (b) Time expanded view just before and after the deposition. Potential was pulsed from +0.05 V to -0.15 V at 0 s and back at 67 s.

We also monitored Cu electrodeposition by AFM, scanning only the x-direction while cycling the electrode potential in order to investigate where Cu electrodeposition proceeds predominantly at the surface. Figure 6.6 (a) shows an AFM image which was

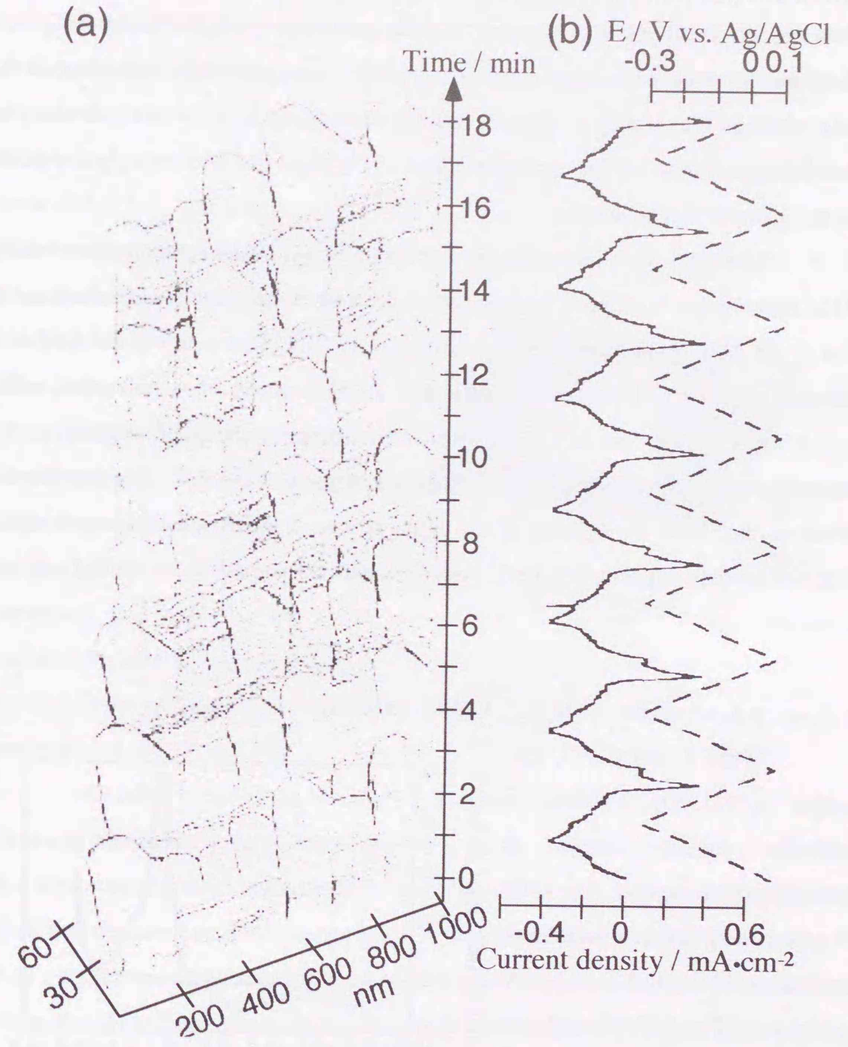

Fig. 6.6 (a) AFM image taken in 9 mM HCl + 1 mM $CuCl_2$ solution during potential cycle between +0.1 V and -0.3 V for 7 times. Only x-scan was activated. (b) Current and potential curves corresponding to the AFM image.

recorded as a function of time when the potential was cycled repeatedly between +0.1 V and -0.3 V at a rate of 10 mV/s. Time sequences of current and potential are also shown in the figure. When the potential was scanned to negative, Cu deposition began to take place as soon as cathodic current started to flow. On the other hand, Cu desorption gave a sharp anodic current peak. Interestingly, Cu deposition took place at the same place all the time, although the quantity of deposits differed cycle by cycle. This result also implies that the manner in which the electrodeposition of Cu proceeded was strongly dependent on the structure of the substrate.

There may be a possibility that the truncated pyramidal structure observed by AFM measurement is different from the actual structure of the substrate/deposition and is that of the AFM tip as pointed out by Grütter *et al.* [43]. This is true if the deposit is sharper than the tip. However, we think that the AFM images shown in this article reflect real structure as we were able to image smaller structure at the initial stage of the Cu electrodeposition process on the flat surface (c.f. Figs. 6.2 and 6.4). The fact that we observed the atomic arrangement of Cu on the terrace of the truncated pyramids of Cu deposits strongly suggests that the Cu deposit was not in a needle form but had a terrace structure.

6.2.2 *p*-GaAs(100) in H_2SO_4-$CuSO_4$ solution

When 1 mM $CuSO_4$ was added to H_2SO_4 solution, a cathodic current flowed at potentials more negative than -0.05 V and a sharp anodic current peak was observed at +0.03 V as the CV is shown in Fig. 6.7. The cathodic current is associated with the bulk Cu electrodeposition onto the GaAs surface and the anodic peak corresponds to the oxidative

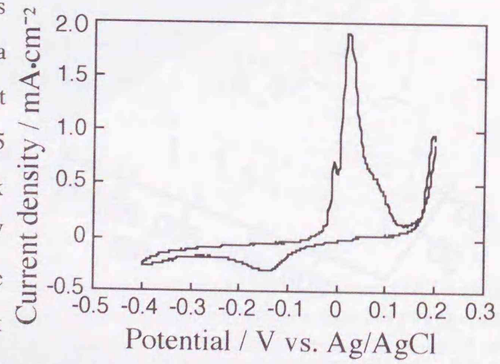

Fig. 6.7 Current-Potential relations of a *p*-GaAs(100) electrode in 1 mM $CuSO_4$ + 10 mM H_2SO_4 solution. Sweep rate: 20 mV / s.

dissolution of the Cu deposit.

Figure 6.8 shows an AFM image of the Cu deposits on a *p*-GaAs(100) electrode captured 30 s after the electrode potential was pulsed from +0.05 V to -0.2 V in 1 mM $CuSO_4$ + 10 mM H_2SO_4 solution. Islands of the Cu deposits appeared over the whole surface and terrace size of those was in an average of 100 nm in the present conditions. As mentioned above for Cu deposition on *p*-GaAs(100) in $CuCl_2$ - HCl solution [24], morphology of the deposits depended strongly on the substrate structure and the result presented in Fig. 6.8 was obtained at a relatively flat surface. The typical shape of Cu islands deposited on the flat surface was triangular pyramid with flat terrace. At the present condition, cathodic current of ca. 50 $\mu A \cdot cm^{-2}$ flowed continuously. The triangular pyramidal structure grew with time but the total number of Cu islands was constant from the initial stage of the deposition. Size and number of the islands were strongly dependent not only on the GaAs surface structure as mentioned before but also on the applied potential and the concentration of Cu^{2+} ion [26].

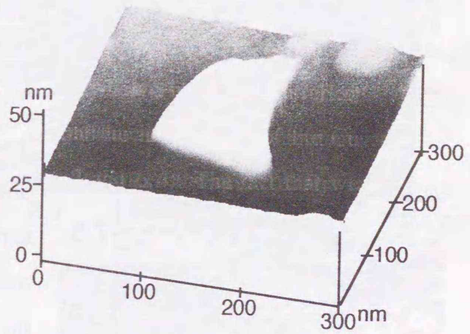

Fig. 6.8 An AFM image (300 nm x 300 nm) of the surface of the Cu islands formed on the *p*-GaAs(100) surface in 1 mM $CuSO_4$ + 10 mM H_2SO_4 solution at -0.2 V vs. Ag/AgCl.

An AFM image observed on the flat terraces of Cu islands in narrow regions shows an atomically resolved structure shown in Fig. 6.9 (a). Figure 6.9 (b) shows a two-dimensional Fourier spectrum of the raw data shown in Fig. 6.9 (a). These results show that topmost atoms have a hexagonal structure with a nearest-neighbor distance of 0.26 ± 0.04 nm, which is almost equal to the known lattice constant (0.256 nm) of bulk Cu in the (111) basal plane. Thus, the Cu deposits seemed to have a closed packed structure. The atomic arrangement of square lattice with atomic distance of about 0.4 nm corresponding to underlying structure of GaAs (100)-(1x1) structure was observed when the tip was scanned over the region between Cu deposited pyramidal structures as shown in Fig. 6.10. These results suggest that the bulk Cu deposition on the GaAs surface

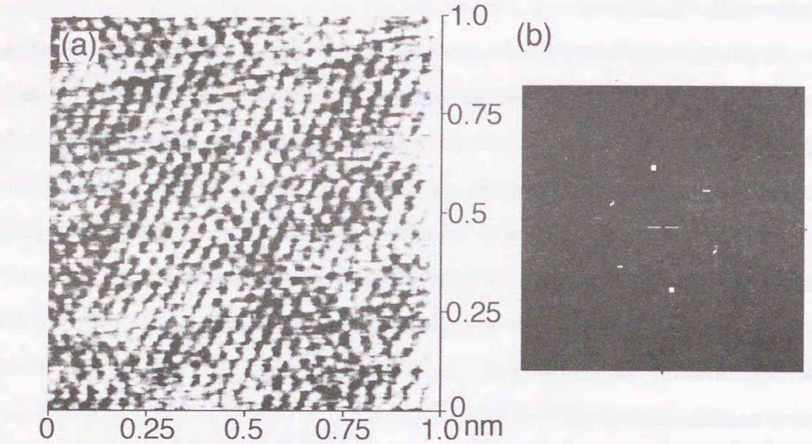

Fig. 6.9 (a) An AFM image (10 nm x 10 nm) of the surface of the Cu deposit on the *p*-GaAs(100) surface obtained at -0.2 V vs. Ag/AgCl, showing Cu(111)-(1x1) structure. (b) Two-dimensional Fourier spectrum of the result of (a).

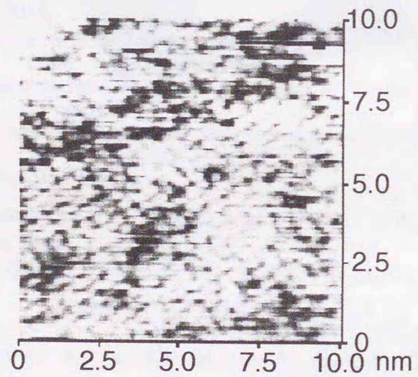

Fig. 6.10 An AFM image (10 nm x 10 nm) of *p*-GaAs(100) electrode between the Cu deposits in 1 mM $CuSO_4$ + 10 mM H_2SO_4 at -0.2 V vs. Ag/AgCl, showing *p*-GaAs(100)-(1x1) structure.

proceeded without strong influence of the orientation of underlying GaAs(100) surface. Manne *et al.* [13] have reported that the Cu(111) structure was formed on the Au(111) substrate in the course of bulk deposition and the closed packed Cu(111) overlayer was incommensurate with the Au(111) surface, as the lattice constant of the face-centered cubic structure of Cu (0.362 nm) is shorter than that of Au (0.408 nm). They suggested that although the initial stage of Cu deposition was strongly affected by the substrate structure, the bulk Cu deposition of Cu on Au(111) proceeded without strong influence of underlying Au(111) structure.

We were able to observe the atomic image on top of almost all the deposits but only fractions of the whole surface of the terrace gave atomically ordered images. There are patched domains of atomically ordered regions and of disordered regions. In most

cases these domains were separated by steps of several nm. The average terrace size was ca. 100 nm as mentioned before but the maximum size of the single domain where atomic arrangement was observed was 20 nm.

Figure 6.11 (a) shows an AFM image with atomic scale obtained at the boundary region between two Cu deposits. Both sides of the boundary region show closed packed hexagonal structures corresponding to the Cu(111) lattice but with different atomic orientation and atoms were less ordered at the boundary region. Atomic arrangements of Fig. 6.11 (a) are schematically shown in Fig. 6.11 (b) as a guide. The angles between two atom rows of the Cu(111) lattice at the boundary regions had no regularity. In addition, the atomic images for individual Cu islands showed various directions of atom rows. These results suggest that each Cu deposit had closed packed structure of different atomic orientation. The direction of atom rows seemed to be determined at the initial stage of bulk Cu deposition.

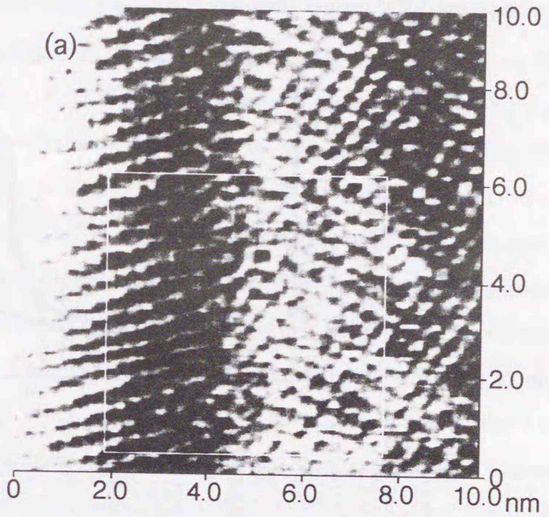

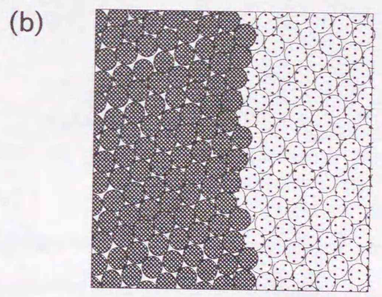

Fig. 6.11 (a) An atomically resolved image of the boundary region of two domains of the bulk deposited Cu on *p*-GaAs(100) surface obtained at -0.3 V vs. Ag/AgCl. (b) Schematically shown atomic arrangement of the boundary region indicated by a white square in Fig. 6.11 (a).

To investigate how the Cu electrodeposition/dissolution proceeded on the *p*-GaAs surface, the atomic images were monitored during potential cycling between the deposition and stripping potentials. Figure 6.12 (a) and 6.12 (b) show current-potential relation and AFM images obtained sequentially while the potential was scanned between -

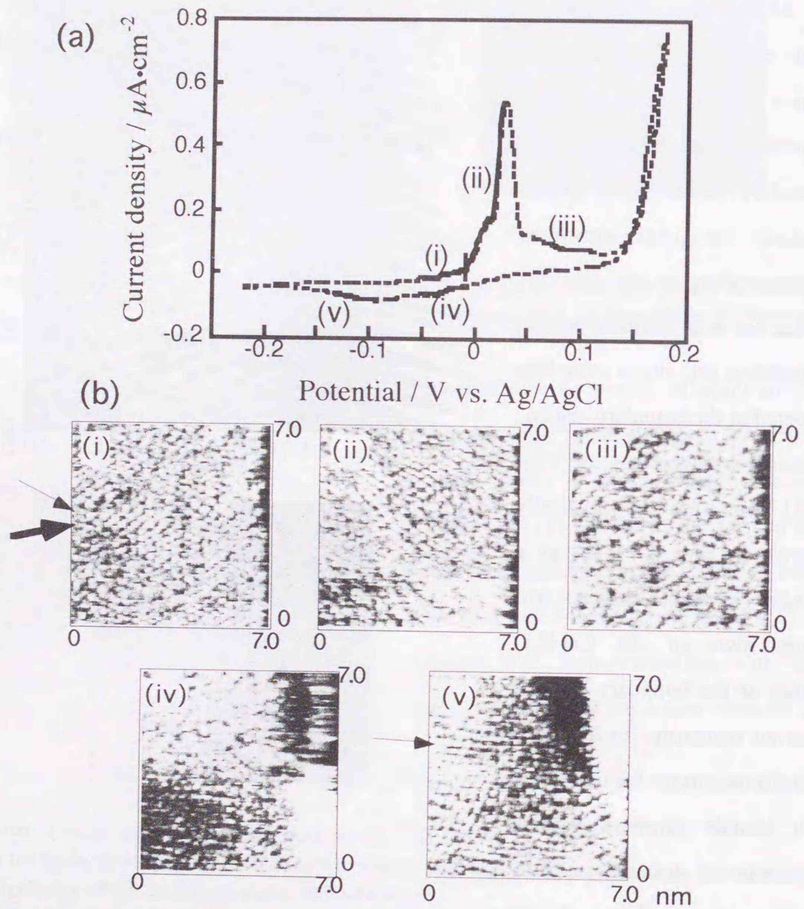

Fig. 6.12 (a) Current-Potential relation of *p*-GaAs(100) in 1 mM $CuSO_4$ + 10 mM H_2SO_4 solution. Sweep rate: 5 mV / s. (b) Sequentially obtained AFM images (7 nm x 7 nm) of *p*-GaAs(100) electrode in 1 mM $CuSO_4$ + 10 mM H_2SO_4 solution while potential was scanned between -0.22 V and +0.18 V. Potential regions where images were taken are shown in Fig. 6.12(a). Thick arrow shows the direction of atom row of the underlying GaAs(100). Narrow arrows show the directions of atom rows of the bulk deposited Cu. Potential regions are (i) -0.05 V ~ -0.01 V, (ii) -0.01 V ~ +0.03 V, (iii) +0.07 V ~ +0.11 V, (iv) -0.01 V ~ -0.05 V, and (v) -0.09 V ~ -0.13 V.

0.22 V and +0.18 V with the potential scan rate of 5 mV/s, respectively. Potential regions where images of Fig. 6.12 (b) were taken are indicated in Fig. 6.12 (a). All images were captured while tip was scanned from the top to the bottom of the image. It took about 8 s to capture one image and, therefore, the potential differed by about 40 mV between the top and the bottom of the image. Figure 6.12 (b)-(i) shows the atomic image of Cu on the GaAs surface at the potential from -0.05 V to -0.01 V. The hexagonal arrangement was confirmed, although the atomic order was not as high as that in Fig. 6.7. When the potential became more positive than 0 V, anodic current for Cu desorption started to flow and atomic image became less clear (Fig. 6.12 (b)-(ii)). The atomic image was completely lost at potentials more positive than +0.05 V (Fig. 6.12 (b)-(iii)). The atomic arrangement was not seen in the potential region between +0.07 V and +0.15 V where no current flowed. The atomic image was recovered when the potential was scanned back to the value more negative than -0.05 V(Fig. 6.12 (b)-(iv)). The atomic image of the Cu overlayer can be seen in the whole image of Fig. 6.12 (b)-(v) but the orientation of atom rows of Fig. 6.12 (b)-(v) is different from that of Fig. 6.12 (b)-(i)). This result confirms that the lattice orientation of the Cu deposits is not dependent on that of the underlying GaAs(100) structure.

6.2.3 Selective Cu Deposition at μm Defects Created by AFM Tip Modified Surface

As mention above Cu deposition on *p*-GaAs(100) depended strongly on the substrate structure [47]. Thus, it is interesting to observe Cu deposition process on GaAs surface where a square hollow was intentionally created by AFM tip.

Figure 6.13 shows an AFM image of *p*-GaAs (100) surface captured at -0.4 V after 1 μm sized square hollow structure was created at +0.05 V where no current flowed by scanning the AFM tip for 1 hour, followed by Cu deposition at -0.4 V in 1 mM $CuSO_4$ + 10 mM H_2SO_4 solution for 40 sec. It is clear that Cu deposition occurred selectively at the scratched portion. If the modified area was larger than 1000 x 1000 nm^2, Cu deposition occurred selectivity at the modified portion regardless of applied cathodic potentials. When the modified area was smaller than 500 x 500 nm^2, Cu deposition was

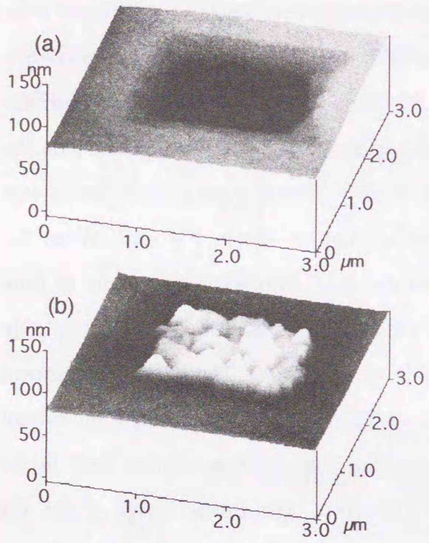

Fig. 6.13 (a) The square pattern(1000 x 1000 nm^2) in the center of image was fabricated by scanning the AFM tip for 1 hour at +0.05 V where almost no current was flowed in 1 mM $CuSO_4$ + 10 mM H_2SO_4 solution. (b) An AFM image (1000 x 1000 nm^2) of *p*-GaAs surface after Cu electrodeposition at -0.4 V on the electrode shown in Fig. (a) in 1 mM $CuSO_4$ + 10 mM H_2SO_4 solution for 40 sec.

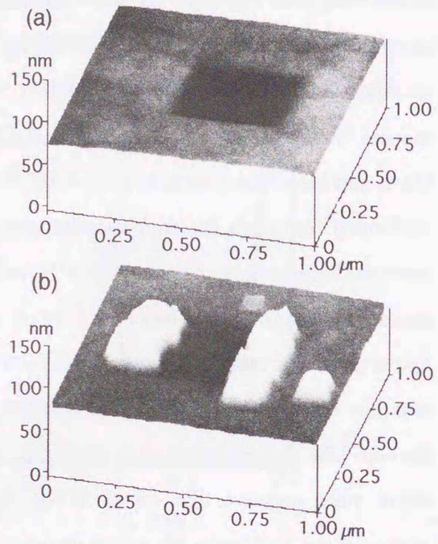

Fig. 6.14 (a) The square pattern(500 x 500 nm^2) in the center of image was fabricated by scanning the AFM tip for 1 hour at +0.05 V where almost no current was flowed in 1 mM $CuSO_4$ + 10 mM H_2SO_4 solution. (b) An AFM image (500 x 500 nm^2) of *p*-GaAs surface after Cu electrodeposition at -0.4 V on the electrode shown in Fig. (a) in 1 mM $CuSO_4$ + 10 mM H_2SO_4 solution for 40 sec.

inclined to take place not at the modified portion but around the modified area (Fig. 6.14). In this case, the Cu deposition process was strongly dependent on the applied cathodic potential. The lower the overpotential applied, the more selective than Cu deposition tended to occur around the modified portion. The detailed mechanism for the selective Cu deposition is not clear at present.

6.5 Conclusion

In situ ECAFM was used to monitor the Cu electrodeposition process on p-GaAs(100) surfaces. While the reaction proceeded with the nucleation-and-growth process on the flat surface, deposition occurs on the surface structure without a clear nucleation process when the surface had truncated pyramids. The truncated pyramids must have many defects such as step and kink sites and the defect sites must have high reactivity for Cu deposition. Atomically ordered structure of closed packed hexagonal arrangement corresponding to the bulk Cu(111) face was observed at the surface of the Cu deposits on *p*-GaAs(100) in H_2SO_4 - $CuSO_4$ solution. The direction of the atom rows of Cu deposits varied from grain to grain, suggesting that the Cu deposition on GaAs surface was not influenced by the orientation of underlying GaAs(100) surface.

The ECAFM study also showed that the electrodeposition of Cu took place selectively at the defects of μm size created by the AFM tip, demonstrating the possibility of surface nanofabrication by combination of a variety of electrode reactions and the scanning of the tip.

References

1) K. Franaszcuk and J. Sobokowski, *Surf. Sci.* **204**, 530 (1988).
2) A. J. Arvia, R. C. Salvarezza and W. E. Triaca, *Electrochim. Acta* **34**, 1057 (1989).
3) N. M. Markovic and P. N. Ross, Jr., *J. Vac. Sci. Technol. A* **11**, 2225 (1993).
4) A. Damjanovoic, T. H. V. Setty, and J. O'M. Bockris, *J. Electrochem. Soc.* **113**, 429 (1966).
5) M. H. J. Hottenhuis, A. L. M. van den Berg and J. P. van den Eerden, *Electrochim. Acta* **33**, 1519 (1988).
6) R. Sonnenenfeld and P. K. Hansma, *Science* **232**, 221 (1986).
7) O. M. Magnussen, J. Holts, R. J. Nichols, D. M. Kolb and R. J. Behm, *Phys. Rev. Lett.* **64**, 2929 (1990).
8) T. Hachiya, H. Honbo and K. Itaya, *J. electroanal. Chem.* **315**, 275 (1991).
9) S. -L. Yau, X. Gao, S. -C. Chang, B. C. Schardt and M. J. Weaver, *J. Am. Chem. Soc.* **113**, 6049 (1991).
10) S. Manne, P. K. Hansma, J. Massie, V. B. Elings, and A. A. Gewirth, *Science* **251**, 183 (1991).
11) G. Staikov, K. Jüttner, W. J. Lorenz and E. Bundevski, *Electrochim. Acta* **39**, 1019 (1994).
12) C. -h. Chen, S. M. Vescky and A. A. Gewirth, *J. Am. Chem. Soc.* **114**, 451 (1992).
13) C. -h. Chen and A. A. Gewirth, *Phys. Rev. Lett.* **68**, 1571 (1992).
14) N. Ikemiya, S. Miyaoka and S. Hara, *Surf. Sci.* **311**, L641 (1994).
15) R. J. Nichols, W. Beckmann, H. Mayer, N. Batina and D. M. Kolb, *J. Electroanal. Chem.* **330**, 381 (1992).
16) K. Batina, D. M. Nichols, *Langmuir* **8**, 2572 (1992).
17) R. Snnenfeld and B. C. Schardt, *Appl. Phys. Lett.* **49**, 1172 (1986).
18) K. Tomita and K. Itaya, *Surf. Sci.* **201**, L507 (1988).
19) K. Uosaki and H. Kita, *J. Vac. Sci. Technol. A* **8**, 520 (1990).
20) K. Kowal, L. Xie, R. Huq and G. C. Farrington, *J. Electrochem. Soc.* **141**, 116 (1994).
21) P. Allongue and E. Souteyand, *J. Electroanal. Chem.* **286**, 217 (1990).
22) N. Nakato, S. Tsumura and H. Tsubomura, *Ber. Bunsenges. Phys. Chem.* **80**, 1289 (1976).
23) K. Kautek, J. Gobrecht and H. Gerischer, *Ber. Bunsenges. Phys. Chem.* **84**, 1034 (1980).
24) P. Allongue, *Ber. Bunsenges. Phys. Chem.* **92**, 895 (1988).
25) S. E. Gilbert and J. H. Kennedy, *J. electrochem. Soc.* **135**, 2385 (1988).
26) T. Thundat, L. A. Nagahara and S. M. Lindsay, *J. Vac. Sci. Technol. A* **8**, 539 (1990).
27) S. Erikson, P. Carlsson, B. Holmström and K. Uosaki, *J. Electroanal. Chem.* **313**, 121 (1991).
28) P. Carlsson, B. Holmström, K. Uosaki and H. Kita, *J. Electroanal. Chem.* **283**, 425 (1990).
29) S. Erikson, P. Carlsson, B. Holmström and K. Uosaki, *J. Electroanal. Chem.* **337**, 217 (1992).
30) P. Carlsson, B. Holmström, H. Kita and K. Uosaki, *Surf. Sci.* **237**, 280 (1990).
31) K. Itaya, R. Sugawara, Y. Morita and H. Tokumoto, *Appl. Phys. Lett.* **60**, 2534 (1992).
32) S.-L. Yau, F. F. Fun and A. J. Bard, *J. Electrochem. Soc.* **139**, 2825 (1992).
33) P. Allongue, H. Brune and H. Gerischer, *Surf. Sci.* **257**, 414 (1992).
34) P. Allongue, V. Kieling and H. Gerischer, *J. Electrochem. Soc.* **140**, 1009 (1993).
35) K. Uosaki and M. Koinuma *J. electroanal. Chem.*, **357**, 301 (1993).
36) M. Koinuma and K. Uosaki, *J. Vac. Sci. Technol. B*, 12, 1543 (1994).
37) M. Koinuma and K. Uosaki, *Surf. Sci.*, **311**, L737 (1994).
38) K. D. Kepler and A. A. Gewirth, *Surf. Sci.* **303**, 101 (1994).
39) J. J. Kelly and R. Memming, *J. Electrochem. Soc.* **129**, 729 (1982).

40) S. R. Morrison, in *Electrochemistry at Semiconductor and Oxidized Electrode*, Plenum Press, New York (1980).
41) W. P. Gomes and H. H. Goossens, in *Advances in Electrochemical Science and Engineering* (Edited by H. Gerischer and C. W. Tobias), Vol. 3, VCH Publishers, New York (1994).
42) M. Koinuma and K. Uosaki, J. Electroanal. Chem. in press (1996).
43) P. Grütter, W. Zimmerman-Edling and D. Brodbeck, *Appl. Phys. Lett.* **60**, 2741 (1992).

CHAPTER 7

In situ OBSERVATION OF ANODIC DISSOLUTION PROCESS OF *p*-GaAs(001) IN HCl SOLUTION BY SXRD

CHAPTER 7

In situ OBSERVATION OF ANODIC DISSOLUTION PROCESS OF *p*-GaAs(001) IN HCl SOLUTION BY SXRD

7.1 Introduction

As already described in the proceeding chapters, the STM and AFM techniques provide very useful information for the understanding of electrochemical reaction at the electrode surface [1,2]. Although they are quite useful to probe local atomic structure of the substrate, the accuracy for the determination of the atomic distance is rather limited. As far as the accuracy for the atomic distance is considerable, surface X-ray scattering (SXS) techniques is superior to STM and AFM. SXS gives a Fourier transformed image of the atomic structure with a lateral resolution better than 10^{-3} nm, although the information is of the average over macroscopic region. SXS studies of metal single crystal electrode surfaces include the surface reconstruction of Au [3-6], UPD on Au, Ag, and Pt [7-11], halide adsorption on Au [11,12], roughening of Pt [13].

Control and observation of electrochemical and photoelectrochemical dissolution reactions of semiconductor electrodes are very important in establishing the electrochemical/photoelectrochemical etching processes and stable photoelectrochemical cells [14]. GaAs is one of the most attractive semiconductor materials to be used in various electronic devices and in dry/wet solar cells. Thus, many papers on the electrochemical behaviors of GaAs in dark and under illumination have been published [15-18]. In the proceeding chapters *in situ* structural observation of bare and Cu deposited GaAs surfaces with atomic scale using electrochemical AFM were reported [19-22]. No paper of the application of SXS to semiconductor/electrolyte interface, however, has been published expect the very recent one by Zegenhagen *et al.* who reported the results of surface X-ray reflectivity measurement at *n*-GaAs(001) electrode in H_2SO_4 solution and surface X-ray diffraction (SXRD) measurement at Cu islands deposited on *n*-GaAs(001) surface [23].

In this chapter, SXRD technique was employed to investigate the anodic dissolution process of the *p*-GaAs(001) surface in HCl solution.

7.2 Results and Discussion

The diffraction peak corresponding to (11) direction for GaAs(001) electrode was obtained in air and in 0.1 M HCl solution. Figure 7.1 shows typical results obtained from normalized high resolution transverse (q-2q) scans recorded by rocking the (11) direction for GaAs(001) in air (a) and in 0.1 M HCl at -0.5 V (b). The diffraction intensity contains information from both surface and bulk structure because the incident X-ray penetrates the GaAs sample into several hundred Å even when the incident angle is 0.4°. Although the diffraction intensity in HCl solution is much smaller than that obtained in air because of scattering by the solution and Kapton window, the peak position and full-witdh-at-half-maiximum (FWHM) were almost the same. This result shows that the lattice spacing in HCl solution is identical with that in air. High resolution transverse scans also revealed that full-witdh-at-half-maiximum (FWHM) did not change by the introduction of HCl solution into the electrochemical cell. The values of FWHM are 0.006 $Å^{-1}$ in both cases, which showed that the domain sizes for the samples were about 1000 Å. This is much bigger than the typical domain size of metal single crystals such as Au and Pt which are usually 2~300 Å [8,11]. The diffraction peak appeared every 90 degree against f axis reflecting the 4-fold symmetry of the GaAs(001) [24].

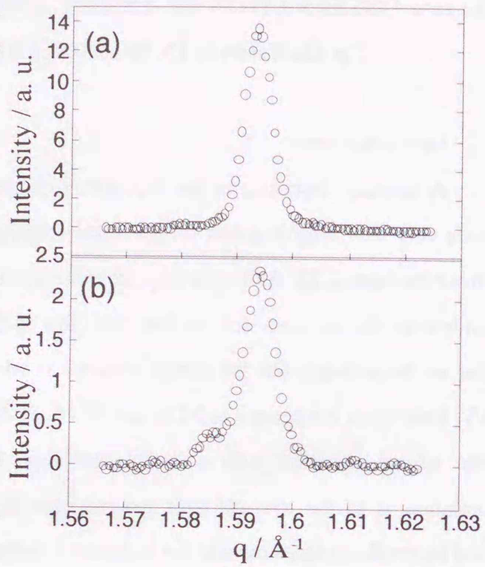

Fig. 7.1 *In situ* SXRD characterization of *p*-GaAs(001) in air (a) and 0.1 M HCl solution (b). High resolution tranverse scans recorded by the rocking the sample along the GaAs(001) direction.

When anodic potential was applied to the GaAs electrode, dissolution current flowed and the intensity of diffracted peaks decreased with time. Figure 7.2 shows the time course of the diffraction peak intensity after the application of +0.5 V where the steady current of 30 $\mu A \cdot cm^{-2}$ flowed. Although a very large current (several $mA \cdot cm^{-2}$) was observed at +0.5 V in a conventional electrochemical cell, only small current flowed in the present SXRD measurement due to the very thin solution layer. The intensity of diffraction peak decreased and then became constant. The diffraction intensity was never vanished while the electrode was kept at anodic potential. Anodic charge flowed at the GaAs electrode per minute is 3.5 $mC \cdot cm^{-2}$. As the electrochemical equivalence of the anodic dissolution reaction of the GaAs electrode was reported to equal to 6 in acidic solution [25,26], the vertical dissolution rate of the GaAs surface was estimated to be about 16 $Å \cdot cm^{-2}$ if the dissolution reaction proceeded homogeneously.

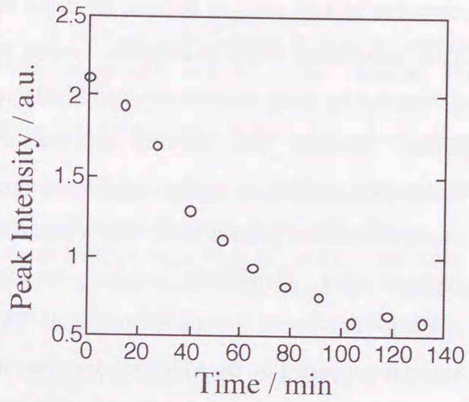

Fig. 7.2 The diffraction intensity for (11) direction of *p*-GaAs(001) recorded as a function of time at -0.5 V in 0.1 M HCl solution.

It is known that electrochemical anodic dissolution of the GaAs electrode in HCl solution proceeds most selectively at (111) face [27], Thus, the selective etching of (001) plane along (111) direction seems to cause the diffraction intensity to decrease.

Figure 7.3 shows a possible model of the structural change of GaAs(001) surface due to the anodic dissolution along (111) direction. The *p*-GaAs(001) surface was flat as shown in Fig. 7.3 (a) before the anodic dissolution occurred. In this case, the diffraction of the incident X-ray should occur in all the portion that X-ray penetrated. When the anodic dissolution started, a number of (111) facets were formed on the (001) surface (Fig. 7.3 (b)). The diffraction intensity decreased with time because the (001) crystal orientation decreased in the portion of X-ray penetration. The defect sites formed in the initial stage dissolved selectively along (111) direction and became gradually larger. Finally, pyramidal structures which contained four (111) faces appeared on the whole surface as shown in Fig. 7.3 (c). If the pyramidal structures were formed on the whole surface, the apparent surface structure stopped to change. Thus, the diffraction intensity

seemed to be kept constant because the depth of X-ray penetration remained constant. Gomes *et al.* reported by using ellopsometry and SEM that porous structure was formed on the *p*-GaAs(100) surface in acidic solution during anodic dissolution process [28]. This result also supports that GaAs(001) surface became gradually uneven in the anodic potential. The model is supported by the AFM data describes in chapter 5. According to AFM results shown in Fig. 5.4, the height of the domain structures became gradually larger but the size of those did not change. Thus, portions in the outskirts of the domains *i.e.* (001) plane, were removed by the anodic etching process.

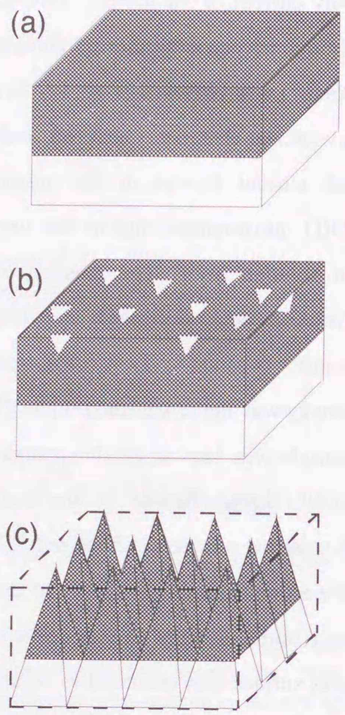

Fig. 7.3 Most possible model of the structural change of *p*-GaAs(001) as a result of the anodic dissolution. The incident X-ray penetrates in dashed region.

7.3 Conclusion

In situ SXRD was carried out to follow the anodic dissolution of *p*-GaAs(001) electrode in HCl solution. The diffraction intensity of (11) direction for *p*-GaAs(001) surface was obtained every 90 degree in 0.1 M HCl solution. As the anodic dissolution process progressed, the intensity of diffraction peaks decreased. The decrease in diffraction intensity indicates that the GaAs(001) surface became rough. This result is in good agreement with the AFM results on the anodic dissolution process described in chapter 5. More careful examination in various solutions should provide useful information on the termination is the dangling bond.

References

1) A. J. Bard, H. D. Abruna, C. E.Chidsey, L. R. Faulkner, S. W. Feldgerg, K. Itaya, M. Majda, O. Melroy, R. W. Murray, M.D. Porter, M. D. Soriage and H. S. White, *J. Phys. Chem.* **97**, 7147 (1993).
2) A. A. Gewirth and V. Siegenthaler, In Nanoscale Probes of the Solid/Liquid Interface, Kluwer Academic Publishers, Dordrecht 1995.
3) B. M. Ocko, J. Wang, A. J. Davenport, and H. S. Isaacs, *Phys. Rev. Lett.* **65**, 1466 (1990).
4) J. Wang, B. M. Ocko, A. J. Davenport, and H. S. Isaacs, *Phys. Rev. B* **46**, 10321 (1992).
5) I. M. Tidswell, N. M. Markovic, C. A. Lucas, and P. N. Ross, *Phys. Rev. B* **47**, 16542 (1993).
6) W. Polewska, C. M. Vitys, B. M. Ocko, and R. R. Adzic, *J. Electroanal. Chem.* **364**, 265 (1994).
7) M. H. Samant, M. F. Toney, G. L. Borges, L. Blum, and O. R. Melroy, *J. Phys. Chem.* **92**, 220 (1988).
8) M. F. Toney, J. G. Gordon, L. Kau, G. L. Borges, O. R. Melroy, M. H. Samant, D. G. Wiesler, D. Yee, and L. B. Sorensen, *Phys. Rev. B* **42**, 5594 (1990).
9) M. F. Toney, J. G. Gordon, M. H. Samant, G. L. Borges, D. G. Wiesler, D. Yee, and L. B. Sorensen, *Langumir* **7**, 796 (1991).
10) J. Wang, R. R. Adzic, O. M. Magnussen, and B. M. Ocko, *Surf. Sci.* **344**, 111 (1995).
11) B. M. Ocko, G. M. Watoson, and J. Wang, *J. Phys. Chem.* **98**, 897 (1994).
12) B. M. Ocko, O. M. Magnussen, R. R. Adzic, J. Wang, Z. Shi, and J. Lipkoski, *J. Electroanal. Chem.* **376**, 35 (1994)
13) H. You and Z. Nagy, *Physica B* **33**, 3830 (1994).
14) For example, S.R. Morrison, *Electrochemistry at Semiconductor and Oxidized Electrode*, Plenum Press, New York, (1980).
15) K.W. Frese, Jr., M.J. Madou and S.R. Morrison, *J. Electrochem. Soc.* **128**, 1527 (1981).
16) P. Allongue and H. Cachet, *Electrochim. Acta.* **33**, 9 (1988).
17) K. Uosaki, Y. Shigematsu, S. Kaneko and H. Kita, *J. Phys. Chem.* **93**, 6521 (1989).
18) J. S. Blakemore, *J. Appl. Phys.* **53**, R123 (1982).
19) M. Koinuma and K. Uosaki, *Surf. Sci.* **311**, L737 (1994).
20) M. Koinuma and K. Uosaki, *J. Vc. Sci. Technol. B* **7**, 1543 (1994).
19) M. Koinuma and K. Uosaki, *Electrochim. Acta* **40**, 1345 (1995).
22) M. Koinuma and K. Uosaki, *J .Electroanal. Chem.* in press (1996).
23) J. Zegenhagen, A. Kazimirov, G. Scherb, D. M. Kolb, D. -M. Smilgies, R. Feidenhans'l, *Surf. Sci.* in press (1996).
24) J.S. Blakemore, *J. Appl. Phys.* **53**, R123 (1982).
25) H. Gerischer, *Ber. Bunsenges. Phys. Chem.* **69**, 578 (1965).
26) E. A. Efimov and I. G. *Erusalimchik, Elektrokhimiya* **1**, 818 (1965).
27) W. P. Gomes and H. H. Goossens, *Electrochemistry of III-V Compound Semiconductor: Dissolution Kinetics and Etching* in Advances in Electrochemical Science and Engineering (Eds. H. Gerischer and C. W. Tobias), Vol. 3, Sec. 1, VCH, NY (1994).
28) S. Lingier and W. P. Gomes, *Ber. Bunsenges. Phys. Chem.* **95**, 170 (1991).

CHAPTER 8

GENERAL CONCLUSION

CHAPTER 8
GENERAL CONCLUSION

In this thesis the morphological and electronic structures of the semiconductor/electrolyte solution interfaces were studied.

The effect of various surface treatments of *n*-GaAs(100) on the tunneling characteristics was investigated by TCV. The effect was attributed to the density of surface states. It was found that the "ruthenium treatment" and the "sulfur treatment" are considered to introduce and remove the surface states, respectively.

Hexagonal atomic arrangement was observed in both *n*-type and *p*-type InSe(0001) materials in air and in electrolyte solution. The atomic arrangement was obtained not only for topmost atoms, Se, but also the second In layer. Electrochemical AFM measurement was carried out to monitor the surface structure change of the *p*-InSe electrode during electrochemical potential cycling with atomic resolution. It was found that atomically ordered structure observed in negative potential region was lost after anodic reaction proceeded as amorphous Se layer deposited on the surface but was recovered if the electrode was cathodically biased that the Se layer was removed by the cathodic reaction. Thus, it was demonstrated that AFM is very useful to follow the surface change caused by electrochemical reaction.

Atomically structural GaAs(100)-(1x1) structure was obtained in HCl, H_2SO_4, and Na_2S solution. The result suggests that the topmost atoms are terminated with chemical species in electrolyte solution after the cathodic removal of oxide layer. In HCl solution, the GaAs(100)-(1x1) structure seems to be stabilized as a result of termination with Cl^- ion. H^+ ion and S atoms seems to terminate with the dangling bond of GaAs(100) surface in H_2SO_4 and Na_2S solution, respectively.

AFM tip induced surface modification of the GaAs electrode surface was also studied. The effect of number of scans, scanning rates, and applied electrode potentials on the efficiency of the surface modification were investigated. The formation of modified structure on the surface requires both the scanning of the tip and the flow of anodic current, showing the modification is the result of the tip-induced electrochemical etching.

It was found that how the electrodeposition of Cu on *p*-GaAs(100) proceeded strongly depended on the structure of the substrate. While the reaction proceeded with the nucleation-and-growth process on the flat surface, deposition occurs on the surface structure without a clear nucleation process when the surface had truncated pyramids. AFM results suggest that the bulk Cu deposition on GaAs surface proceeded without strong influence of the orientation of underlying GaAs(100) surface. Atomically ordered structure of closed packed hexagonal arrangement corresponding to the bulk Cu(111) face was observed at the surface of the Cu deposits on *p*-GaAs(100).

Surface x-ray diffraction technique was employed to follow the anodic dissolution process of the GaAs(001) in 0.1 M HCl solution. The surface diffraction intensity for (11) direction decreased in anodic potential region with time as a result of selective etching of (100) plane along (111) direction.

It was demonstrated here that clean and atomically ordered surface of compound semiconductors can be prepared in electrolyte solutions if the proper treatment is employed. This fact should lead to the new development of science and technology of semiconductor. The finding of the tip induced etching and selective deposition of Cu on the modified portion should open the way to novel nano-fabrication technique.